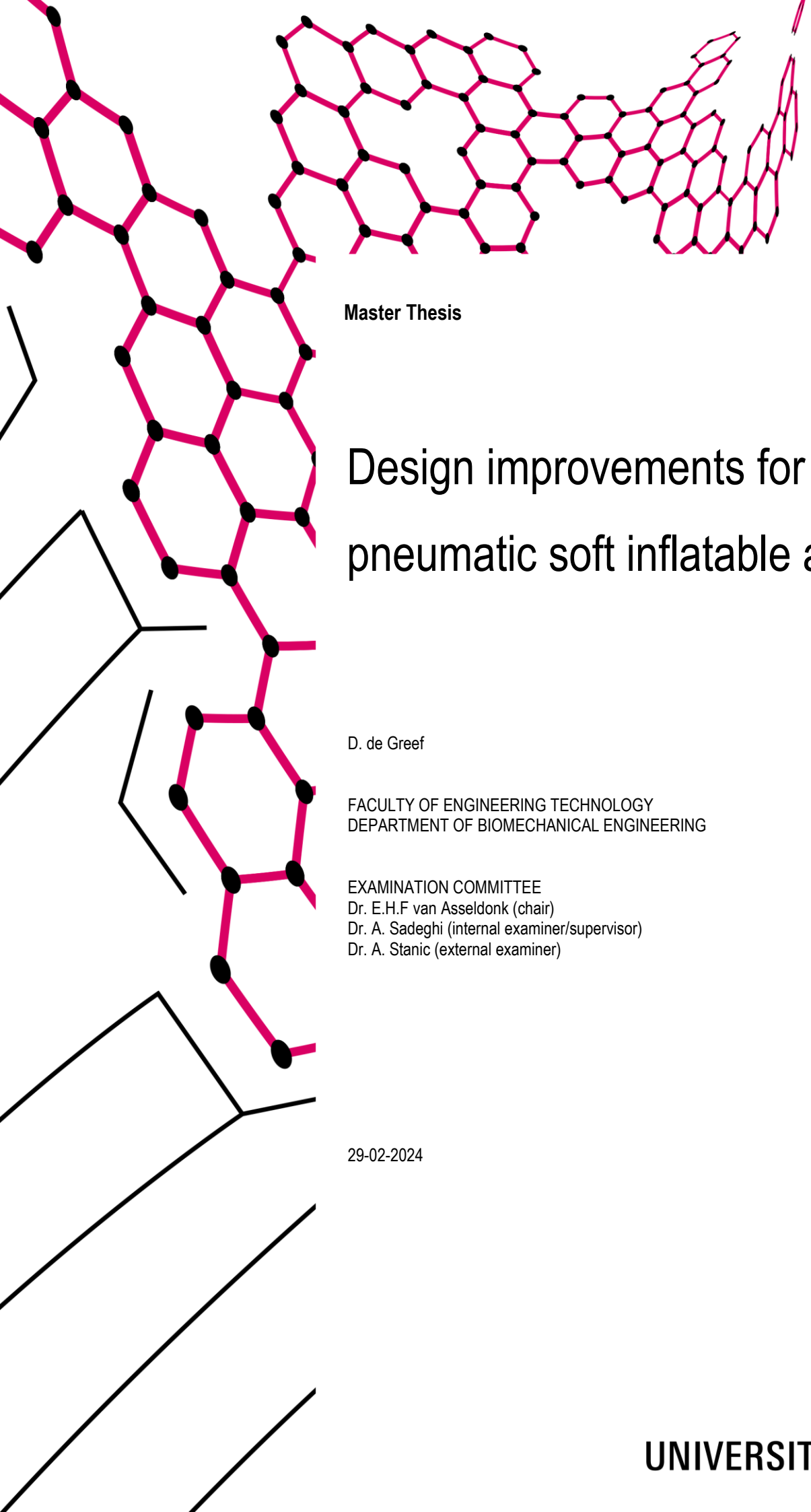

Master Thesis

Design improvements for a pneumatic soft inflatable actuator

D. de Greef

FACULTY OF ENGINEERING TECHNOLOGY
DEPARTMENT OF BIOMECHANICAL ENGINEERING

EXAMINATION COMMITTEE
Dr. E.H.F van Asseldonk (chair)
Dr. A. Sadeghi (internal examiner/supervisor)
Dr. A. Stanic (external examiner)

29-02-2024

UNIVERSITY OF TWENTE.

Acknowledgements

I would like to thank Ali Sadeghi for his daily supervision and support during the Master assignment, without him I would not have been able to achieve this. Furthermore, I would like to thank Saivimal Sridar for his support and help in both the theoretical and practical aspects of this master thesis.

Abstract

In an attempt to reduce the requirements of the pneumatic source and possibly move to an unthetered setup, a design improvement to the soft inflatable actuator is presented in this paper. Current state of the art soft actuators tend to be shaped as a solid pouch of air, while the newly proposed design is shaped as a hollow cylinder. The newly proposed design consumes a lower volume of air for inflation, while achieving similar output forces in bending applications. The increased performance per unit volume air is observed at all pressures tested and is supported by a theoretical model. There is however a significant discrepancy between the results of the theoretical model and the experimental results, which will require further research to prove the validity of the theoretical model. When the actuator is axially loaded the results from the theoretical model match with the experimental results and no improvement per unit volume is observed. It is hypothesised that an improvement will be found for a long and slender design, however, this was not experimentally investigated.

Contents

1 Introduction

Walking is one of the most important functions in daily life and is a complex cooperation of bones, muscles, sensory receptors and the nerve system. When problems occur in one of these systems it can cause gait disorders, which can be caused by a large variety of disorders. For patients suffering and/or recovering from neuromuscular disorders, such as cerebral palsy (CP), stroke, amyotrophic lateral sclerosis (ALS) and multiple sclerosis (MS) walking becomes problematic, if not impossible. This has devastating effects on the quality of life of these individuals.
Robots that have a human operator can be divided into different categories. Serial robotic manipulators, which interact with the operator at the end-effector. Exoskeletons are robots that cover the anatomical joint(s) of the operator and moves synchronously with these joints. To augment human mechanical effort, wearable robotic systems such as exoskeletons are used. These can either augment limps or replace lost limps. These systems have great promise for applications in rehabilitation, medicine and even for physical enhancement of non-impaired users. Many different kinds of exoskeletons and wearable robotics have been researched by research facilities. These can be subdivided in a few different groups based on their function. Empowering robotic exoskeletons are robots that enhance the strength of the human user while keeping the user in control. These robots map onto the existing user anatomy. The second class are orthotic robots, which also maps onto the users anatomy, but this class rather restores lost or weak functions to their original level, caused by a wide variety of diseases or neuromuscular disorders. The last class are prosthetic robots, which replace the limbs rather than mapping onto existing anatomy [Pons, 2008].
These robotic solutions can be subdivided further by their actuation mechanism. A large variety of actuation methods are available to achieve the mechanical effort of the robots. Each of these different actuation methods have their own advantages and disadvantages, which have to be weighed for the specific application in which the solution will be implemented. Possible actuation methods include electric motors, pneumatic, hydraulic, electrohydraulic transducers, electroactive polymers. Within these different categories subdivisions can be made between rigid and soft actuators. Rigid actuators with respect to exoskeletons generally consist of a rigid frame which transfers the forces from the actuation method to the user. Soft actuators are opposite of the rigid actuators, where they do not have this rigid frame and are able to deform along with the body of the user. Both the rigid and soft actuators have their own advantages and disadvantages.
Despite promising results in recent studies in the field of wearable robots [Mooney et al., 2014, Malcolm et al., 2013, Sup et al., 2009, Talaty et al., 2013, Farris et al., 2014], there are still some major limitations that hinder the widespread usage of these systems [Caldwell et al., 1994]. The mass and rigidity of the actuation methods in these wearable robots are among their main limitations. The rigidity results in more complex systems and can also decrease user comfort. The rigid exoskeletons usually have fixed axes of rotation and thus need to be aligned carefully with the anatomical joints to not cause harm to the user.

1.1 Rigid actuators

1.1.1 Electric motors

Electric motors come in a wide variety of sizes, output force and actuation types. Many exoskeletons use this type of actuation, due to it's high control precision, quick response and relatively large output forces. These actuators, however, also tend to be relatively heavy, significantly reducing their power-to-mass ratio, which is one of the most important characteristics for exoskeletons. High weight, especially located distally, significantly increases the metabolic cost of the user [Barnett et al., 1993] [Sovero et al., 2017]. On top of the relatively high mass of these actuators, they are also rigid and require precise alignment with the anatomical joints of the users, in order to not harm the user during actuation. Furthermore, the rigidity tends to result in more complex systems and can also decrease user comfort.
Exoskeletons relying on electric motors for actuation have several different methods of transferring the force from the actuator to the joints of the user. These actuation methods include, direct drive, electro-hydraulic, cables [Pons, 2008]. These actuation methods each have their own advantages and disadvantages. The electro-hydraulic and cable solution can also be categorized as soft or hybrid solutions, depending on the implementation. Usually these systems use rigid interfaces with the user, while the remainder of the setup is soft and flexible.
Direct drive relies on the straightforward transmission of the actuator onto the joint. The actuator can be rotary or linear. An example of a direct drive actuation method would be positioning a rotary actuator in such a way that the point of rotation aligns with the human elbow or knee. Since these joints are relatively simple they can be actuated directly by the electric motor given that the alignment of the joint with the point of rotation is good. This allows for a simple system to be created. The disadvantages of this actuation type become clear when the complexity of the actuation increases [Pons, 2008]. When, for instance, the shoulder joint is actuated using a system like this, a highly complex system will need to be designed to enable actuation of the different degrees of

freedom (DoFs). This most likely results in a bulky and heavy system which is not desired [Gao et al., 2023]. On top of the complex and heavy system, the mass is located on the joint, which results in further challenges when it comes to control, as well as the increased metabolic costs. The system shown in Figure 1 already made a bunch of optimizations to reduce the complexity and adverse effect of the high mass, such as moving the actuator distally, using carbon fiber to reduce mass and using a cable setup instead of direct drive.

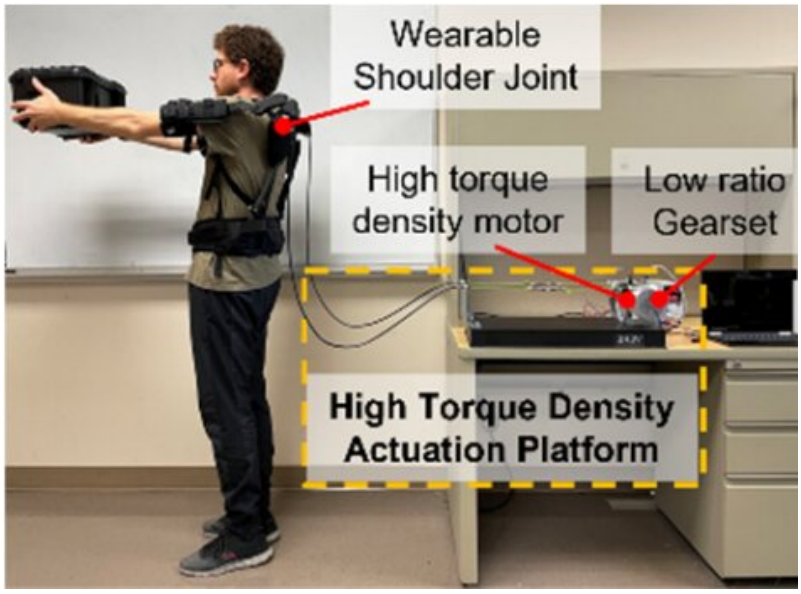

Figure 1: State of the art active shoulder exoskeleton [Gao et al., 2023]

Electro-hydraulic actuation is a combination actuation method, which combines an electrical motor with a hydraulic transmission system. An example of this can be found in [Bechet and Ohnishi, 2014]. This specific system would be best categorized as a hybrid solution, since the hydraulic tube can be considered soft, while the syringes are rigid and thus the actuator cannot be defined as fully soft. This actuation method relies on an electromagnetic motor to provide the force/actuation of the system. The force from the distally located motor is transferred to the target joint by the use of syringes filled with water. One syringe is located near the actuator and the other is located at the target joint. The syringes are connected using a tube filled with water. The main advantages of a system like this are the ability to position the motor distally, which can significantly reduce the metabolic cost for the user. Additionally, the system can provide both pushing and pulling motions, achieve high accuracy, and deliver force quickly.
Cable systems are somewhat similar to the previously mentioned electro-hydraulic actuation system. The actuator can be located distally and the force from the actuator is transferred to the target joint using a cable system. One of the advantages of the cable systems is the ability to have low friction forces and zero backlash, as long as the cables are tensioned [Pehlivan et al., 2013]. Cable system also can be designed to have speed reduction, which in turn can decrease the weight of the entire system. One of the main disadvantages of cable systems is that they are unable to handle compression forces. To overcome this shortcoming, most systems are designed with an antagonistic force to control the joint. The cable transmission can be even further subdivided into categories based on the type of cable used, which can be seen in Figure 2. These each have their own advantages and disadvantages with respect to friction, backlash, efficiency, controllability, etc. [Sanjuan et al., 2020]. The cable system actuator can be classified as rigid, hybrid or fully soft depending on the exact solution used. If Bowden cables are used, the system can classified as fully soft since the system can deform along with the user, albeit with some resistance. If however motorized reel to anchor point transmissions are used the system might get classified as rigid due to rigid frame elements used, to which the cables are attached. The exact classification is not of importance, but it should be remembered that these systems have their own advantages and disadvantages and these tend to show similarities with other actuator solutions within the same classification.

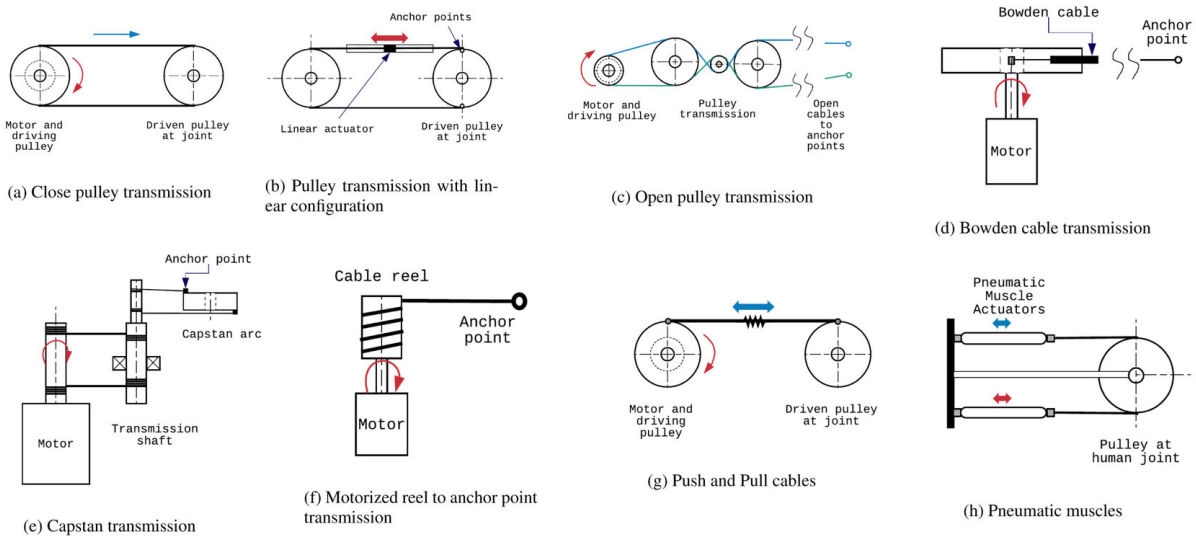

(a) Close pulley transmission

(b) Pulley transmission with linear configuration

(c) Open pulley transmission

(d) Bowden cable transmission

(e) Capstan transmission

(f) Motorized reel to anchor point transmission

(g) Push and Pull cables

(h) Pneumatic muscles

Figure 2: Overview of different actuation and transmission systems [Sanjuan et al., 2020]

1.2 Soft actuators

Soft actuators generally are lightweight, able to deform along with the body and relatively cheap, which tackle some of the main limitation of rigid actuators; however, they also have some disadvantages of their own. A wide variety of physical mechanisms have been used to provide the deformation in the soft materials, including, pneumatic inflation, combustion and electrostatic force. Each of these techniques has their own upsides and downsides with respect to force, displacement, speed, auxiliary equipment requirements and reliability [Rich et al., 2018], [El-Atab et al., 2020]. They also provide a comprehensive overview of untethered soft robots, which shows only a very small number of attempts at untethered soft pneumatic actuators. In Figure 3 a comprehensive overview can be seen of many different classes of soft actuators. In Figure 4, the soft actuators discussed in this paper can be seen.

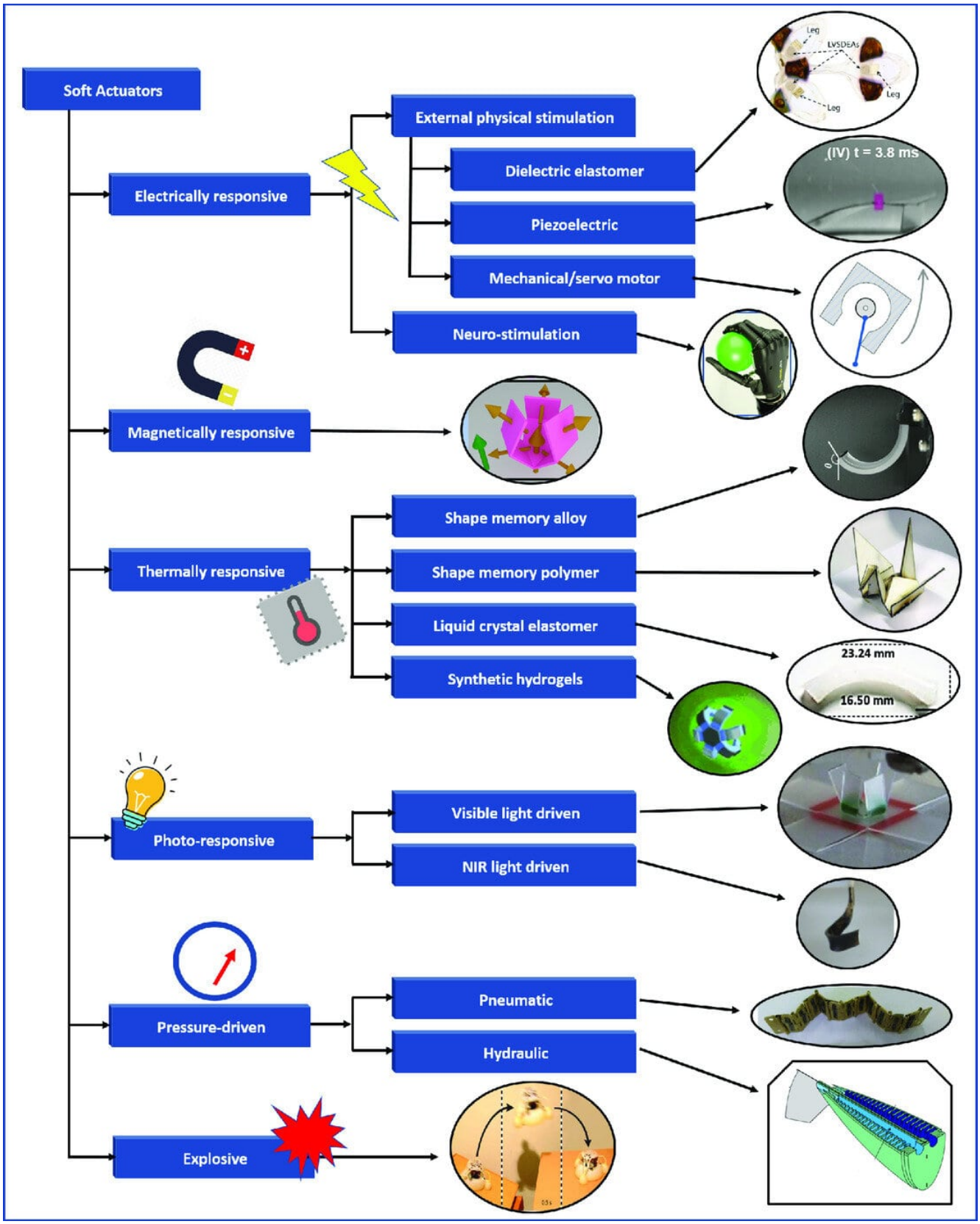

Figure 3: Overview of soft actuator types. [El-Atab et al., 2020]

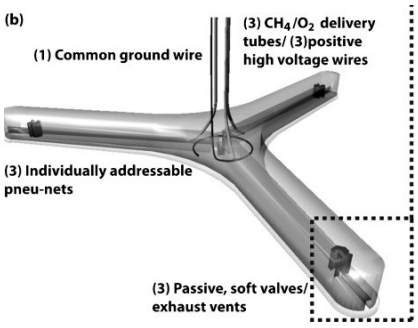

(a) Combustion actuator [Shepherd et al., 2013]

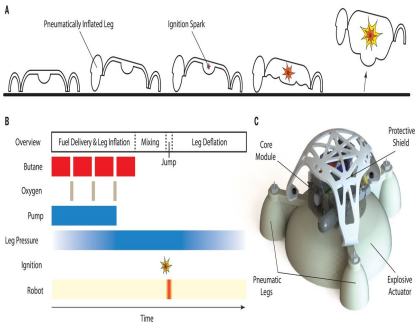

(b) Combustion actuator [Bartlett et al., 2015]

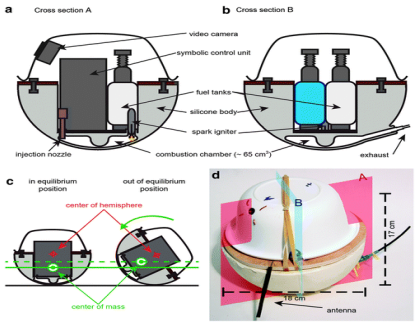

(c) Combustion actuator [Loepfe et al., 2015]

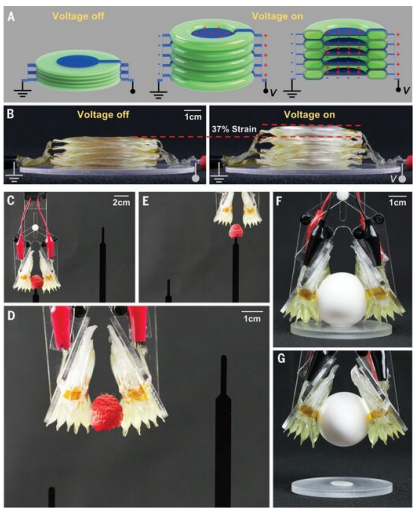

(d) HASEL actuator for gripping objects [Acome et al., 2018]

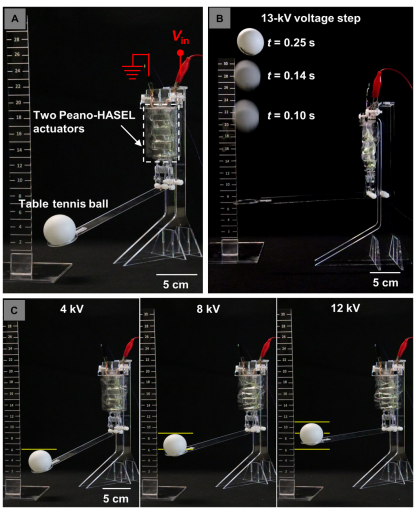

(e) Contracting HASEL actuator [Kellaris et al., 2018]

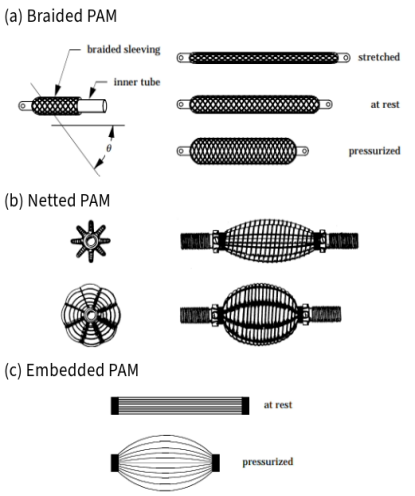

(f) Different categories of Pneumatic Artificial Muscles (PAM) [Daerden, 1999]

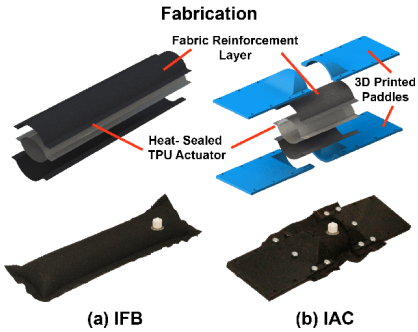

(g) Pneumatic actuator enhanced with rigid paddles to reduce actuator volume [Sridar et al., 2020]

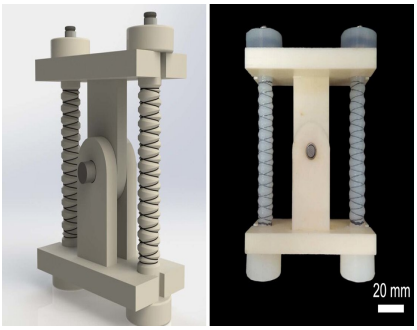

(h) Antagonistic reverse PAM (rPAM) setup [Skorina et al., 2018]

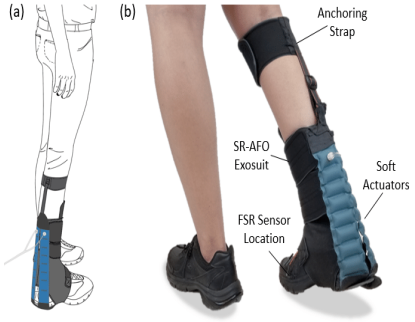

(i) SR-AFO, a state of the art plantar flexion assistance pneumatic actuator [Thalman et al., 2020]

Figure 4: Schematic overview soft actuators

1.2.1 Pneumatic actuators

Pneumatic actuators are an alternative to the pneumatic/hydraulic cylinders and motors for the generation of actuation. Pneumatic actuators, as the name suggests, rely on gasses to generate the forces for actuation. Air is the gas of choice for almost all pneumatic actuators used in exoskeletons, because it is readily available. Pneumatic actuators can also be subdivided in a few different categories based on actuation techniques. The pneumatic actuators used for exoskeletons are soft pneumatic actuators, which mean they consist of soft materials that can deform along with body. The different soft pneumatic actuators discern themselves by the way the pneumatic pressure is used to achieve actuation, both in designed geometry as well as the way to achieve this pneumatic pressure. The inflation of the prototype causes a change in geometry, which in turn can be used as actuation. The change

in geometry depends on the material used and the design of the actuator. Many different geometry changes can be used to achieve actuation and animals have been used as inspiration for a lot of the soft pneumatic actuator designs, some of the inspiration animals are elephant trunks, octopus tentacles and worms/snakes [Xavier et al., 2022]. Some examples of pneumatic actuators can be seen in Figure 5. However, not all pneumatic actuators are fully soft, depending on the actuation technique and the application, rigid connections with human joints might be required. The main advantages of pneumatic actuators are its ability to deform along with body, the low weight and adjustable impedance. This makes them highly suitable for applications with a lot of environmental uncertainty. Pneumatic actuators also tend to be relatively cheap with the highest cost coming from the pneumatic source.
The different actuation methods of the soft pneumatic actuators each have their own upsides and downsides with respect to speed, stroke and force. Generally, there exists a trade-off triangle between these factors, where a large stroke either requires a significantly longer time to be achieved and/or results in a lower output force. Similarly, a fast-moving actuator typically compromises either on the output force it can generate and/or the stroke it can achieve. This is caused by the fact that force for these actuators is proportional to the pressure. When the volume of the actuator increases, which is often necessary for larger strokes, it reduces the pressure that the actuator can attain within a given time frame, assuming the same air supply.
Combustion actuators are a subcategory for pneumatic actuators where the volume change required for the geometrical change is being generated by combustion [Rich et al., 2018], [El-Atab et al., 2020]. The big upside for combustion actuators is that they are able to achieve this volume change very rapidly, however the supply for combustion actuators is very limited. Where the number of inflation cycles is limited by the running out of the combustion mechanism. Combustion actuators are capable of achieving rapid inflation; however, controlling this inflation is often challenging and limited in terms of precision. This makes them unsuitable for usage in exoskeletons, on top of the risks of possibly harming the user. Furthermore, combustion based actuators also require a very strong body in order to not be damaged by the combustion itself, which also limits the ability to be a soft actuator. Examples of combustion based actuators are found in [Shepherd et al., 2013], [Bartlett et al., 2015], [Loepfe et al., 2015].

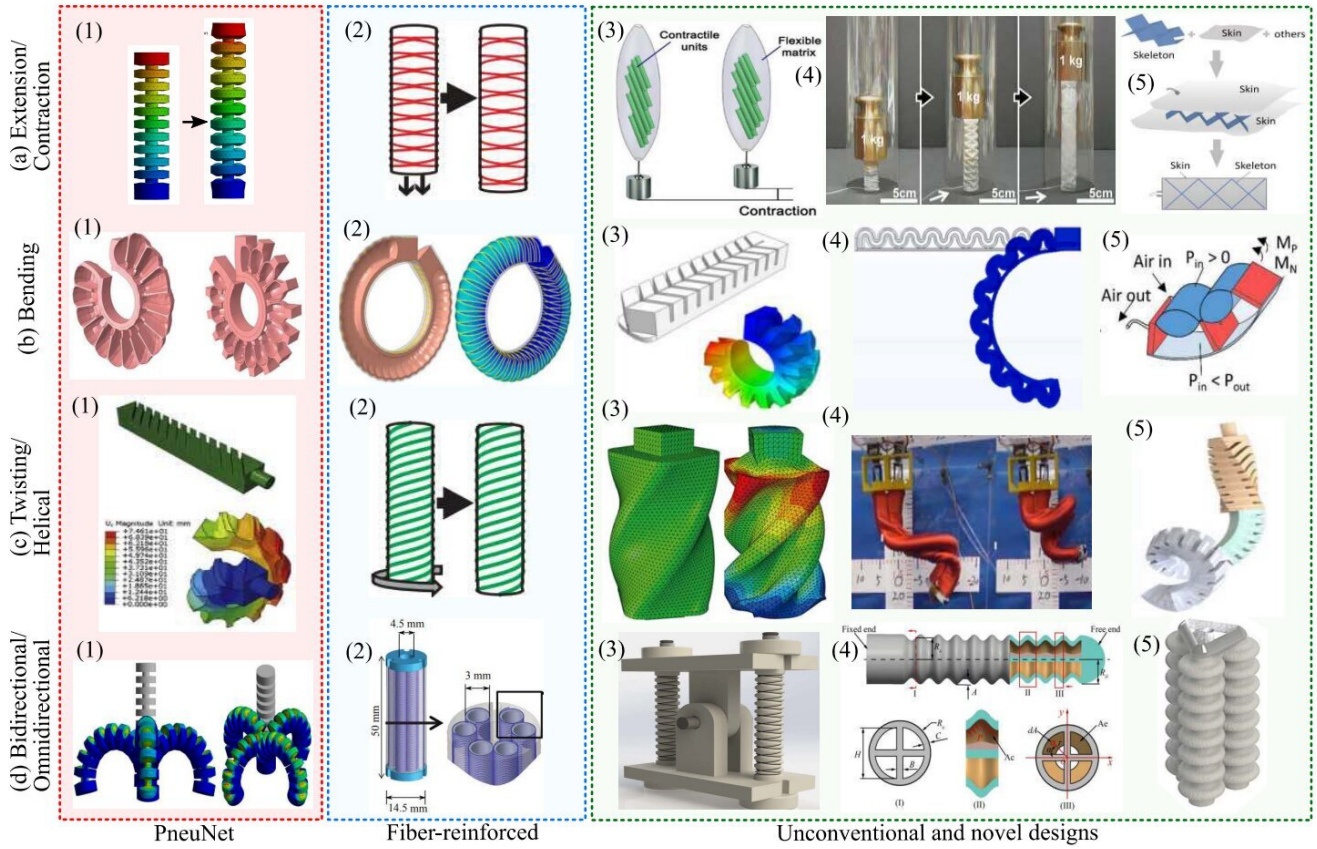

Figure 5: Examples of inflatable soft actuator designs. (a) Extension and contraction soft pneumatic actuators (SPAs). (b) Bending SPAs. (c) Twisting and helical SPAs. (d) Bidirectional and omindirectional SPAs. [Xavier et al., 2022]

1.2.2 Dielectric elastomers

Dielectric elastomer actuators work based on the Coulomb force of two flexible electrodes with a deformable membrane between them. These actuators are able to achieve large strains and high efficiencies. In addition, these actuators have an exteremly fast response time and are cost-effective in production, due to the use of inexpensive materials. These actuators, however, are prone to failure due to the presence of high electric fields that travel across them. This problem is solved with the introduction of a new variation of these actuators. Hydraulically amplified self-healing electrostatic (HASEL) actuators, which combine these dielectric elastomer actuators with a hydraulic solution between them. This allows for a variety of actuation modes. These actuators are able to self-heal after dielectric breakdown, while being able to mimic human muscles. These actuators are able to lift more than 200 times their own weight [Acome et al., 2018], [Kellaris et al., 2018]. Possible applications for these actuators may include exoskeletons designed for muscle activation that require lower forces, such as finger movements, considering that the output force of these actuators is relatively low.

1.2.3 Other soft actuators

Many other possible methods of actuation are available for soft actuators, which include but are not limited to, piezoelectric-based actuators, magnetically responsive actuators, shape memory alloys, shape memory polymers, liquid crystal elastomers, synthetic hydrogels, visible-light-driven actuators, near IR-driven actuators [El-Atab et al., 2020]. However, all of these actuator types have some major limitations, which is why they have not been implemented for exoskeleton designs yet. These include very low output forces, extremely slow actuation times, up to minutes and relatively small strains.

1.3 Soft vs rigid actuators

Soft actuators have a have a variety of advantages with respect to their rigid counterparts. Where rigid robots consist of rigid links connected together by rigid or elastic joints, recent soft actuator solutions consist of soft bodies that are expected to change their effective stiffness in order to provide actuation or compliance. When designing robots/exoskeletons, compromises have to be made between weight, size, cost, speed and complexity among others. This is highly dependent on the application of the robotic solution. When designing an exoskeleton it is very important to minimize the weight while being able to achieve sufficient speeds for usage. The size of the actuator is determined by the specific application requirements, but the objective is to achieve actuation using a low-profile actuation method. To provide control in a system with significant uncertainty resulting from interactions with both the environment and the user, it is crucial to limit complexity. As mentioned at the start, there have been some promising results in field of wearable exoskeletons recently, but these still have some limitations. This is where soft actuation methods have some very notable advantages with respect to their rigid counterparts. Soft actuators and soft exoskeletons are much lower in weight due to the lightweight compliant materials used to produce them. Having a high weight, especially located distally significantly increases the metabolic cost of the user [Barnett et al., 1993] [Sovero et al., 2017]. However, soft actuators do not fully solve this problem either, as they typically still require a heavy power source to provide the actuation to the soft actuator. The upside is that this weight can be located in a strategically chosen location on the users body, usually around the torso, to significantly reduce the impact of this added weight.

Due to the rigidity of rigid exoskeletons they require precise alignment with the joints of the user and they also require highly advanced control solutions to be able to deal with environmental uncertainty. This is one of the major advantages of soft actuators with respect to their rigid counterparts. Soft actuators/exoskeletons try to use the existing human geometry for structure. This approach offers the advantage of not only significantly reducing the weight of the solution but also enabling better handling of uncertainty. Due to the soft nature of these actuators they also should have very limited impact on the users locomotion in the "off"-state, where the soft actuator will just deform along with the body.

Speed and output force is where rigid actuators tend to outperform their soft counterparts. Rigid actuators are able to provide much higher output forces and are able to provide these forces at very high speeds. If however the power to weight ratio is considered this changes significantly, as can be seen in Table 1 [Alici, 2018]. It should be noted that while the maximum operation frequency mentioned here may be achievable for small actuators, when a pneumatic actuator is used in an exoskeleton, this frequency may be further reduced due to the larger volumes of air required. The speed off rigid actuators tends to be higher than that of their soft counterparts, especially when larger strokes/forces are required.

The cost of soft actuator tends to be significantly lower than that of their rigid counterparts, due to a combination of reasons. The main reason for the cost difference between rigid and soft actuators comes from the materials used to produce the actuator. Where the rigid components and actuators tend to generally be relatively expensive,

soft actuators like pneumatic actuators can be produced from cheap materials like fabric in combination with an air-tight material like a polymer. On top of this, rigid actuators require precise alignment and significantly higher levels of accuracy compared to their soft counterparts. This further contributes to the price difference between the various types of actuators. Furthermore, the production of small sample sizes of soft actuators is generally a lot cheaper than their rigid counterparts as well, due to the ease at which the materials can be handled. This is further enhanced by the rapidly developing 3D printing space, which allows for much more intricate soft actuator designs to be produced, at low cost.
Rigid actuators however also have some advantages compared to their soft counterparts. Rigid actuators tend to be able to achieve much higher output forces per volume of space available, which can be limited in applications like exoskeletons, where bulkiness reduces user comfort. As mentioned previously rigid actuators tend to be able to achieve significantly faster actuation times, especially when a high accuracy is required for the task. While soft actuators are good at adapting to unknown environments, they are also prone to non-linearities and other uncertainties, which can make controlling these actuators difficult, especially when high accuracies are necessary.

Table 1: A comparison of typical robotic actuators with the human muscle with approximate values. Specific power ρ is the power per unit of weight, $\sigma_{\max}$ is the maximum force applied by the actuator per unit area (i.e. maximum actuation stress), $\varepsilon_{\max}$ is the maximum actuation strain. Maximum stress and maximum strain are valid for linear actuators. E is the actuator modulus of elasticity. Efficiency is the mechanical efficiency. $f_{\max}$ is the maximum operation frequency. The indexes without a numerical value depend on too many operation and design parameters. Therefore, they are left blank. [Alici, 2018]

Actuator type	$\varepsilon_{\max}$	$\sigma_{\max}(MPa)$	$E(MPa)$	$\rho[W/kg]$	Efficiency	$f_{\max}$
Muscle	0.3-0.4	0.1-0.4	5-20	50-284	0.2-0.4	50-500
DC Motors	0.4	0.1	–	100	0.6-0.9	-
Pneumatic	0.1-1	0.5-0.9	50-90	4000	0.4-0.5	50-300
Hydraulic	0.1-1	20-70	2-3 $\times 10^3$	1600-2000	0.9-0.98	50-300

1.4 Pneumatic actuators

Pneumatic actuators are the most used type of soft actuator in wearable robotics applications, due to the high output force, low cost, low weight, compactness, its inherent compliance and large possible strokes [Rich et al., 2018]. The pneumatic actuation of this actuator type can be achieved by a variety of different source methods. These sources have their own up- and downsides, however the behaviour of the pneumatic actuator is also highly reliant on the design of the actuator itself. Pneumatic actuators work by the change in pressure inside the actuator which results in strain. By limiting the strain in certain directions, specific movements can be created. Pneumatic actuators are able to achieve a large variety of different shapes, which allows for a large variety of actuation modes. Pneumatic actuators are able to extend, rotate, twist, bend or any combination of the above, which allows them to take most configurations in a 3D space.
The output force of pneumatic actuators is proportional to the pressure inside the actuator, thus increasing the pressure inside the actuator allows the actuator to output larger forces. For exoskeleton applications, being able to output a force as large as possible is preferred. The ability to generate large forces from an actuator typically enables the actuator to be scaled down in size while still achieving similar force output levels as a less powerful actuator. This scaling-down is often preferred in order to reduce size and weight, which would result in less interference with the natural gait of the user.
The pressure inside a pneumatic actuator cannot be arbitrarily scaled up, as doing so would introduce the risk of explosions and other failure issues. This problem can be offset by designing the pneumatic actuator with materials such that the pressure can be increased without the material rupturing. Choosing materials that are able to withstand larger forces generally also means that strain gets more limited as well, which might not be preferred.
3D printing of soft actuators is becoming a more and more prevalent solution of creating these actuators, as it allows for cheap and fast production. The big downside of 3D printed actuators is that the material tends to have a very low tensile strength which causes the actuators to break very easily [Decker, 2015]. The desired behaviour would be a high tensile strength while still being flexible as to not disrupt the natural gait in the deflated state.
By limiting the strain in pneumatic actuators, a variety of actuation shapes can be achieved. This strain limiting behaviour is generally introduced by material properties and/or smart geometrical design choices. Soft actuators used for exoskeletons tend to perform relatively basic movement tasks, like linear extension/contraction and bending/extension. Some examples of soft pneumatic actuators used in exoskeleton applications include, pneumatic artificial muscle (PAM), reverse PAM (rPAM) and also other solutions like, soft robotic ankle-foot orthosis (SR-

AFO). All these actuators are linear extension/contraction based. PAM actuators include McKibben actuators, Shadow Air Muscle (SAM), Fluidic Muscle [Sárosi and György, 2015]. These actuators are discerned from each other based on their connection, as described by Daerden in [Daerden, 1999]. The actuators consist of two main parts, a flexible membrane and a load carrying element. The flexible membrane is used to contain the gas, while the load carrying element limits the strain in order to achieve larger forces. When these actuators are inflated they expand in radial direction. This expansion in combination with the load carrying element causes the actuator to contract in the longitudinal direction. The three actuators types as discerned by Daerden in [Daerden, 1999], are braided, netted and embedded. Braided muscles include the McKibben actuator, which is a cylindrical braided muscle, that has both the inner membrane tube as well as its surrounding sleeve connected to it's endpoints. These actuators suffer from hysteresis and have a certain threshold pressure which has to be achieved before radial expansion is started. These characteristics are dependent on the materials used as well as the angle at which the fibers are woven around the cylinder. Furthermore, the actuator also suffers from friction, both between fibers and with the inner sleeve, which leads to a decrease in efficiency. Another drawback of McKibben actuators is it's inability to provide contraction forces. To solve this problem an antagonistic muscles setup can be used.
Netted muscles discern themselves from braided muscles by the density of the mesh network around the membrane. Due to the low mesh density of the netted design, the actuator membrane material has to have limited strain. If the straining of the membrane material is easy, the operating pressure while be significantly reduced, thus lowering output forces. The main advantage of this type of actuator is it's ability to keep a near constant surface area and have almost no friction. This results in a higher output force and very low hysteresis.
The third type of actuator mentioned are the embedded muscles. These type of muscles have its load carrying structure embedded into the membrane. Different designs exist for this type of actuator, which include designs where fibers are embedded into the membrane material. The advantage of this is the very low hysteresis and low initial pressure requirement. The fibers have a high stiffness in one direction while having a low stiffness in the others. The big disadvantage of this design is the low radial stiffness, which allows this actuator to only be operated at relatively low pressures.
A different category of linear pneumatic actuators are reverse PAM's (rPAM's), which as the name suggest operate opposite of the previously mentioned PAM's. These actuators provide extension forces upon inflation. This is achieved by constraining the actuator in radial direction, by means of pre-straining the actuator. An example of a rPAM can be found in [Skorina et al., 2018], which consists of a silicone rubber that is radially constrained by symmetrical double-helix threading. When this actuator is pressurized the stresses from the pre-straining are released resulting in axial expansion. The big advantage of this type of design is the much easier modeling and control compared to McKibben actuators, as well as having only very limited radial expansion.
A recently developed pneumatic actuator is the SR-AFO [Thalman et al., 2020], which aids the user in plantar flexion. This research shows a very promising application of a soft actuator for rehabilitation. This actuator consists of a series of connected chambers, which are inflated from a single connection point. When the actuator is pressurized each of the chambers changes it shape from a flat rectangle to a cylindrical shape, as this optimizes the volume to surface area ratio. This change in shape shortens the length of the actuator, which results in a pulling force. The SR-AFO is very similar to the previously described PAM's where it consists of a layer which contains the air, while the other layer limits the strain. The strain limiting layer allows significantly larger pressures to be used than when this actuator would consist of only a membrane material.
Another promising research performed recently is the IAC by Sridar et al. [Sridar et al., 2020]. This research also presents an inflatable soft actuator, which consist of a strain limiting layer and a membrane like middle layer to contain the air. The strain limiting layer is a fabric (Nylon 40D), while the membrane layer consists of two sheets of thermoplastic polyurethane (TPU) with it's edges molten together. This research improves this very basic actuator design by implementing 3D printed paddles, which significantly reduces the required volume to be inflated to achieve a similar stroke.
Attempts have been made at developing a portable solution for generating high flow rates and pressures required for tasks like fast-paced walking or running. The use of pneumatic systems in wearable applications like this, are still hard to achieve due to these high requirements, while also being low weight. An attempt to create a faster flow rate pneumatic source has also been made by Sridar et al. in [Sridar et al., 2020]. While the results of this research are very promising, there is still room for improvement.
There are several options available to increase the effectiveness of these actuators. The goal is to increase the output force of the actuators without increasing the weight of the system, while keeping in mind that weight added at certain locations is more problematic than at other locations. For pneumatic actuators this can be achieved by increasing the operating pressure or improving the design of the actuator. Increasing the operating pressure does not come without risks. While increasing the operating pressure was for instance achieved by applying a strain limiting layer to the inflatable membrane, this option is only available in a limited range. On top of that, increasing the operating pressure will also require a more powerful source, which generally increases the weight of the system,

which is not desired. Design improvements can be made to increase the output force of the actuator, while keeping air volume consumed constant. This would allow for a less powerful pneumatic source to be used, which in turn decreases the weight of the system. If the same source would be used, larger supporting forces to the user would be possible. The preference between these two depends on the exact application of the actuator.
This paper introduces a novel design aimed at achieving equivalent force output while consuming significantly less air. This would allow for a less powerful pneumatic source to be used, which could potentially lead to a fully unthethered setup. The novel proposed design can be used as a building block for future soft pneumatic actuator designs, using low-cost, light-weight materials. The new design can also be combined with other state of the art research like presented by [Sridar et al., 2020], where the soft inflatable pouch from this research can be enhanced with the 3D printed paddles presented in the aforementioned paper.

2 Proposed concept

In many previous designs for soft inflatable actuators including the one mentioned in the 1 Introduction by Sridar et al. [Sridar et al., 2020] the inflatable actuator consists of an airtight material surrounded by a strain limiting sleeve. A schematic example of a soft inflatable actuator application can be seen in Figure 6a, where the inflation of the actuator results in the extension of the knee. The strain limiting sleeve allows the inflatable actuator to take the shape of the strain limiting layer whenever it is pressurized, which is a similar concept to a soccer ball. This is used to provide the work done by the actuator. Since the work done to inflate the actuator is directly proportional to the volume of the actuator, reducing the volume of air required to inflate the soft actuator allows for faster inflation and reduction of the energy required. Being able to achieve this reduction in volume while maintaining similar levels of output force can significantly reduce the energy required and in turn reduce the size of the pneumatic source.
The proposed design change to achieve this reduction in air consumption is to use a hollow cylinder instead of a solid cylindrical pouch, which is schematically shown in Figure 6b. In this image the original design requires the inflation of the entire cylinder. In the proposed concept the red area would be removed and thus only the outside area would have to be inflated, significantly reducing inflation volume. It should be noted that the previously used soft inflatable actuator designs are not necessarily shaped as a cylinder, but rather as a pouch with flat sides, of which an example can be seen in Figure 7a and 7b. In this research paper both designs are shaped in a cylindrical shape instead, to allow for easier testing and a better comparison. The hypothesis is that the proposed design is able to achieve output forces similar to those of the original solid cylinder design, while significantly reducing the volume of air consumed during inflation.

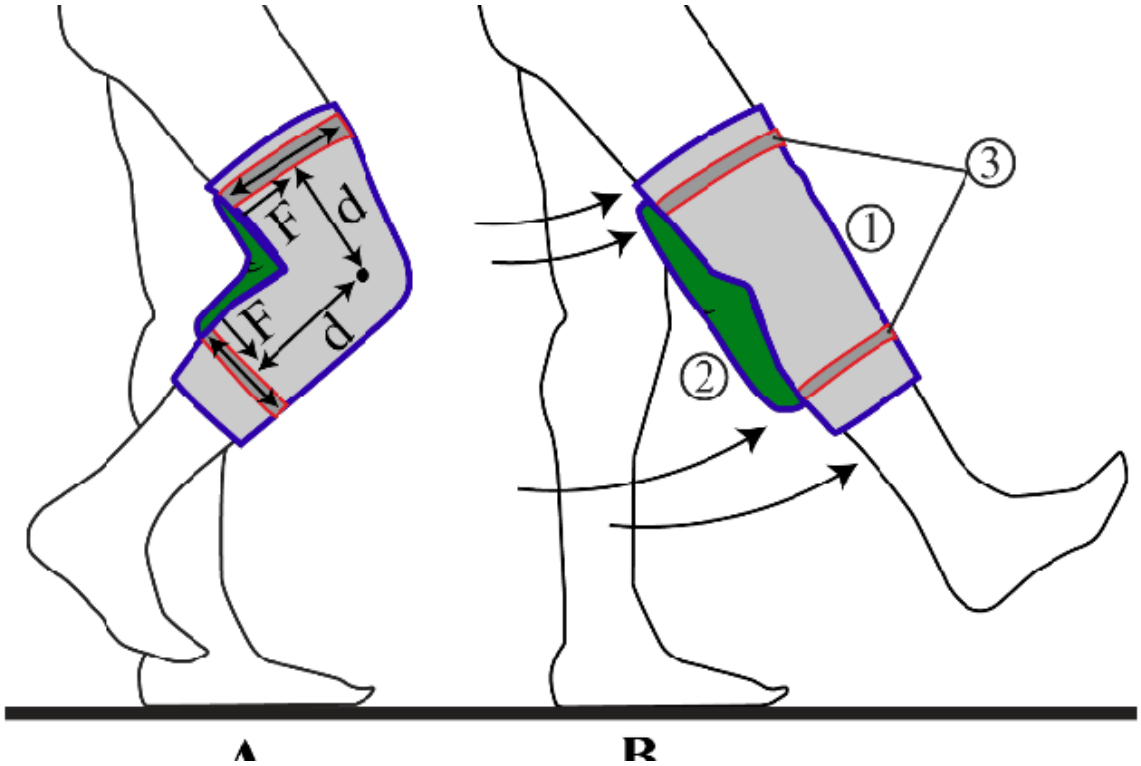

(a) Illustration of force and torque relationship in the exosuit. (1) The knee-sleeve. (2) The inflatable actuators. (3) The hook and loop straps. (A): User in mid-swing gait phase and start of actuator inflation. (B): User at the end of the swing gait phase and completely inflated actuators. [Sridar et al., 2017]

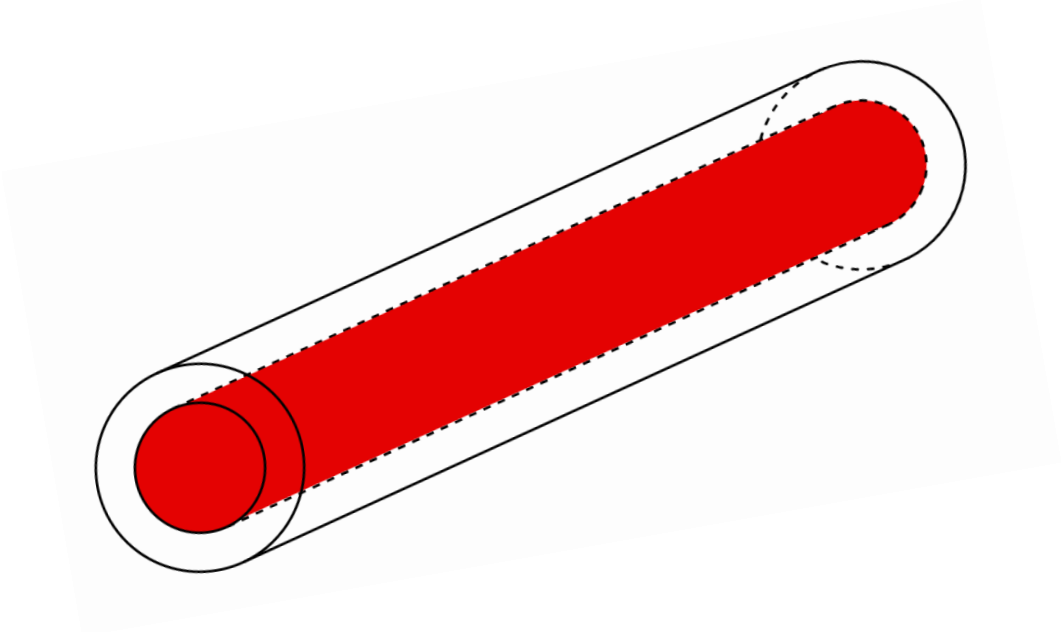

(b) Schematic example of volume reduction hollow cylinder compared to solid cylinder. Red volume is removed in hollow cylinder design

Figure 6: Soft inflatable actuator application and proposed design improvement

(a) Example of previous solid cylinder design (b) Example of previous solid cylinder design after inflation

Figure 7: Examples of solid pouch inflatable actuators

2.1 Theoretical calculations

To support the claims of the improved effective strength of the newly proposed hollow cylinder design, theoretical calculations are performed as well as experimental tests on the produced prototypes. When a cylinder is subjected to an axial load the behaviour can be determined by two different effects. The prototype will be dominated by compressive failure if the designed prototype is short and relatively wide. If the produced prototype is long and slender the behaviour will be dominated by the buckling behaviour and if the prototype cannot be classified as either, the behaviour will be determined by a combination of the two. Furthermore, it is expected that the behaviour of the prototypes in a bending test can be approximated by the Timoshenko beam equations, if beam is relatively short and wide, while the solution can be simplified to the Euler-Bernoulli beam equation if the beams are long and slender. The Timoshenko beam model is only applicable for solid materials and an adaptation to this model should be used instead when inflatables are considered [Le van and Wielgosz, 2005], [Nguyen et al., 2015].

2.1.1 Buckling behaviour

The maximum buckling load can be approximated using Euler's formula for long slender columns, however if the beam is not long and slender, the critical compression load will determine the failure instead. A visual representation of the proposed design can be found in Figure 6b. In this image the entire cylinder, including the red part, will be inflatable for the solid cylinder design. The hollow cylinder design will consist only of the white part, where the red part is removed from solid cylinder. Both designs will have identical dimensions, with the only distinction being the removal of the central portion of the cylinder. This modification reduces the volume necessary to reach inflation.
To evaluate if the prototypes are classified as long and slender beams, the slenderness ratio is used. The slenderness ratio is calculated according to,

$$\lambda = \frac{l}{k} \tag{1}$$

where, k is the radius of gyration and l is the effective length of the beam. The effective length of the beam can be found using,

$$l = LK \tag{2}$$

where, L is the unsupported length of the beam, and K is the column effective length factor, which can be found according to,

- $K = 1.0$ for both ends hinged
- $K = 0.5$ for both ends fixed
- $K = 0.7$ for one end fixed and the other hinged
- $K = 2.0$ for one end fixed and one free to move laterally

For the tests performed on the prototypes, both ends can be considered fixed, which would result in a effective length of the beam of 9 cm, because the cylinders unsupported length is 18 cm. The radius of gyration for the solid cylinder can be found using,

$$k = \sqrt{\frac{I}{A}} \tag{3}$$

where I is the second moment of area and A is the area of the cylinder. Equation 1-3 are found in [Hibbeler, 2014]. The second moment of area for a cylinder can be found according to,

$$I = \frac{\pi}{4}(r_{\text{out}}^4 - r_{\text{in}}^4) \tag{4}$$

where r_{out} is the outer radius of the cylinder, while r_{in} is the inner radius of the cylinder, which are 4.5 cm and 2.5 cm, respectively for the hollow cylinder. For a solid cylinder the inner radius is equal to 0, which removes this term from the equation. The area of the cylinder can be found by,

$$A = \pi(r_{\text{out}}^2 - r_{\text{in}}^2). \tag{5}$$

The effective length is equal for both designs, since both cylinder have the same length and method of support, which is 9 cm. The radius of gyration is however different for the different designs. For the solid cylinder the second moment of area is 322.1 cm^4, while for the hollow cylinder the second moment of area is 291.4 cm^4. The area for the solid cylinder is 63.6 cm^2 while the hollow cylinder has an area of 44.0 cm^2. This results in a respective radius of gyration of 2.3 cm and 2.6 cm. Substituting the found values into equation 1, results in a slenderness ratio of 4 and 3.5, for the solid cylinder and the hollow cylinder respectively. These very low slenderness ratio's show that the major contributor to the failing mechanism will be the compressive failure, whereas if the slenderness ratio would have been high, the contribution would have been mostly due to the buckling behaviour.
If a different prototype is designed to achieve a long and slender behavior, where buckling becomes the primary failure mode, Euler's formula can be utilized to estimate the maximum force at which buckling occurs. Euler's formula requires the beam to be long, slender and assumes perfect axial loading, which leads to:

$$F = \frac{\pi^2 EI}{(KL)^2} \tag{6}$$

where F is the maximum force, E the modulus of elasticity, I the smallest second moment of area of the cross section of the column, L the unsupported length of the column and K the column effective length factor that depends on the boundary conditions of the column. From this formula it can be seen that the difference between the two proposed designs should come from the I term. The second moment of area of the cylinder is found according to equation 4. Since both cylinders have the same length, same support and are made using almost the same materials this should leave only the area moment of inertia as the variable between the different designs in an ideal situation. This would mean that the second moment of area can be optimized for any design given a certain area. For a circular shape this optimal shape would be an infinitely large diameter, with in infinitely thin wall. This is however not optimal for practical reasons, which include wall buckling and no longer being a slender beam. However, when keeping the outer radius fixed and by changing the inner radius it can be shown that the force carried by the center material is much less than the force carried by the outside material. A visual representation of the change of inner radius can be seen in Figure 8.

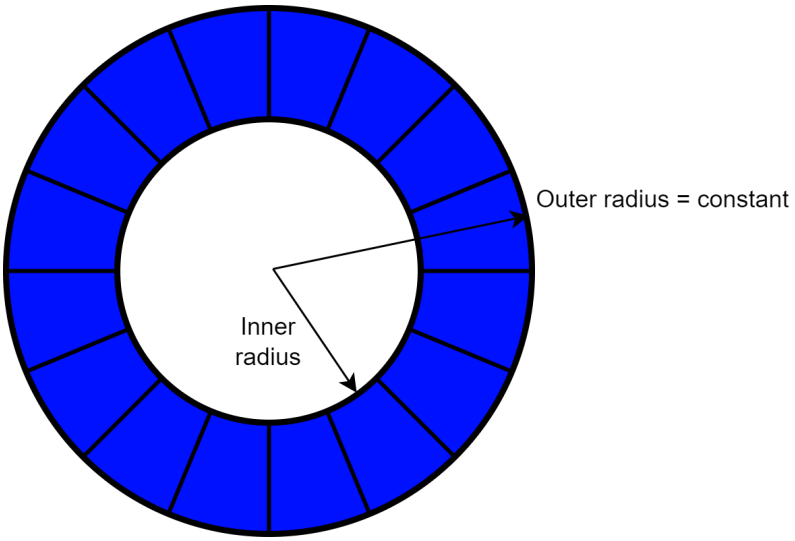

Figure 8: Design intend of hollow cylinder

The inner radius can be expressed as a function of x and the outer radius r_{out} according to

$$r_{\text{in}} = x r_{\text{out}}. \tag{7}$$

Substituting this equation into the equation 4, gives the following relation for the second moment of area,

$$I = \frac{\pi r_{\text{out}}^4 (1 - x^4)}{4} \tag{8}$$

in which x is between 0 and 1. Since x is raised to the 4th power, it can be noticed that the major buckling strength is provided by the outer most material, since x^4 has a rapidly increasing value as it approaches 1. As an example it can be shown that while a fourth of the mass is located in the region for $x = 0.5$,

$$A = \pi r_{\text{out}}^2 (1 - x^2) = \pi r_{\text{out}}^2 (1 - 0.25) = 0.75 \pi r_{\text{out}}^2 \tag{9}$$

it only accounts for $1 - 0.5^4 = 6.25\%$ of the second moment of area,

$$I = \frac{\pi r_{\text{out}}^4 (1 - x^4)}{4} = \frac{\pi r_{\text{out}}^4 (1 - 0.0625)}{4} = \frac{0.9375 \pi r_{\text{out}}^4}{4}. \tag{10}$$

With the insight that only a very small portion of the strength is generated by the center of the cylinder, it shows that the strength per unit air consumed can be greatly increased by removing the center portion of the design. It should however be noted that this is only the case for long and slender beams and not for the low slenderness ratio of the tested prototypes. If the outer radius is fixed the maximum theoretical improvement that can be gained is a factor of 2 as can be shown by,

$$\frac{I_{\text{h}}}{I_{\text{s}}} / \frac{A_{\text{h}}}{A_{\text{s}}} = \frac{\frac{\pi r_{\text{out}}^4 (1 - x^4)}{4}}{\frac{\pi r_{\text{out}}^4}{4}} / \frac{\pi r_{\text{out}}^2 (1 - x^2)}{\pi r_{\text{out}}^2} = \frac{1 - x^4}{1 - x^2} \rightarrow \lim_{x \to 1} = 2. \tag{11}$$

In this equation x is the inner radius of the cylinder, while r_{out} is the outer radius of the cylinder. The subscripts $_{\text{h}}$ and $_{\text{s}}$ represent the hollow and solid cylinder, respectively.

2.1.2 Compressive failure

The main failure mode will be caused by the compressive strength of the prototypes, which is highly dependent on the pressure inside the prototypes. The stress relation is given according to,

$$\sigma = \frac{F}{A} \tag{12}$$

where, σ is the stress and has the dimension of pressure, F is the applied force, A is the cross-sectional area, which is a function of the force, but is generally taken as the initial area. Assuming that the textile sleeve and the

balloons of the prototype have negligible compressive strength, leaves a force balance between the pressure inside the prototype and the applied force. The value for the force can be approximated using a simplified approach to the problem in combination with Boyle's law,

$$P_1 V_1 = P_2 V_2. \tag{13}$$

Boyle's law describes the relation between the pressure inside a container and the volume, where P and V denote the pressure and the volume respectively, while the 1 and 2 denote two different configurations. The initial volume and the volume in state 2 can be found according to,

$$V = A(L - d), \tag{14}$$

where A is the cross-sectional area, L is the initial length of the cylinder, while d is the displacement applied to the cylinder in the axial direction.
When the volume of the container increases, this will be accompanied by a decrease in pressure and vice versa, assuming the temperature is constant. The results from the experimental tests can be validated using equation 13 in combination with equation 12 and the insight that there should be a force balance between the pressure inside the prototype and the external force applied to the prototype.

2.1.3 Bending stiffness

The bending stiffness of a cylinder is also highly dependent on the second moment of area, similar to how long and slender beams are dependent on the second moment of area. Similarly, most of the load carrying capability is achieved by the outer material. The bending of the beam, which is clamped and has a point load on the free end, can be approximated using Timoshenko beam theory, which states that

$$\begin{aligned} p(x) &= \frac{d^2}{dx^2}\left(EI\frac{d\alpha}{dx}\right), \\ \frac{dw}{dx} &= \alpha - \frac{1}{\kappa AG}\frac{d}{dx}\left(EI\frac{d\alpha}{dx}\right), \end{aligned} \tag{15}$$

and can be rewritten to,

$$\begin{aligned} M(x) &= -EI\frac{d\alpha(x)}{dx}, \\ 0 &= \frac{d}{dx}\left(\frac{dw}{dx} - \alpha(x)\right) + \frac{p(x)}{\kappa GA}, \end{aligned} \tag{16}$$

where E is the elastic modulus, I the second moment of area, $\alpha(x)$ is a function that describes the angle of rotation of the normal with respect to the mid-surface of the beam, $M(x)$ is the bending moment for a imaginary small section located at x, w is the displacement in the z-direction, $p(x)$ is a distributed load, κ is a shear coefficient, which is dependent on the geometry of the cross-section, A is the cross sectional area and G is the shear modulus. The shear coefficient for the Timoshenko beam can be found using [Hutchinson, 2000], where the shear coefficient for a circular cross-section is described according to,

$$\kappa = \frac{6\left(a^2+b^2\right)^2(1+\nu)^2}{7a^4+34a^2b^2+7b^4+\nu\left(12a^4+48a^2b^2+12b^4\right)+\nu^2\left(4a^4+16a^2b^2+4b^4\right)} \tag{17}$$

where a is the inner radius of the cylinder, b the outer radius and ν the Poisson ratio. The formula found in [Stephen, 1980],

$$\kappa = \frac{6\left(m^2+1\right)^2(v+1)^2}{v\left(12\,m^4+48\,m^2+12\right)+37\,m^2+7\,m^4+v^2\left(4\,m^4+16\,m^2+4\right)+7}, \tag{18}$$

is very similar formula to the one found in [Hutchinson, 2000] however this formula uses the ratio between the inner and outer radius, which is m and is defined as $\frac{a}{b}$. Equation 18 seems to be the correct definition for the shear coefficient as this value is limited at approximately $[0.5, 1]$, for a value of ν between $[0, 0.5]$. The value found in equation 17 is dependent on size of the cross-section rather than the ratio between the two. Furthermore, equation 17 is dependent on the units used for a and b, which seems illogical for a dimensionless number. Combining the equations in equation 16 together (given a homogeneous beam of constant cross-section) can be used to show the large similarity to the Euler-Bernoulli equation, which leads to,

$$
\begin{aligned}
EI\frac{d^4w}{dx^4} &= p(x) - \frac{EI}{\kappa AG}\frac{d^2p}{dx^2}, \\
EI\frac{d^4w}{dx^4} &= p(x)
\end{aligned}
\tag{19}
$$

where the first equation is the Timoshenko beam equation and the second equation the Euler-bernoulli beam equation. The two equations are very similar with the difference being that the Timoshenko beam equation has an added second order term which accounts for the shear deformation. When the slenderness ratio of the beam increases, the influence of the second term decreases to the point where for long slender beams both equations approximate the same solution.
An analysis can be done using equation 16 to show the influence of the different parameters on the deflection and thus the bending stiffness of a beam. For the example a cantilever beam is used, which is clamped on the left hand side and has a free end on the right hand side, which is subjected to a point load. Furthermore, the positive x direction is to the right, thus from the clamped end towards the free end and z is pointing upwards. A free body diagram has been created for this problem to find the equilibrium conditions for a infinitesimally small portion of the beam, which can be seen in Figure 9.

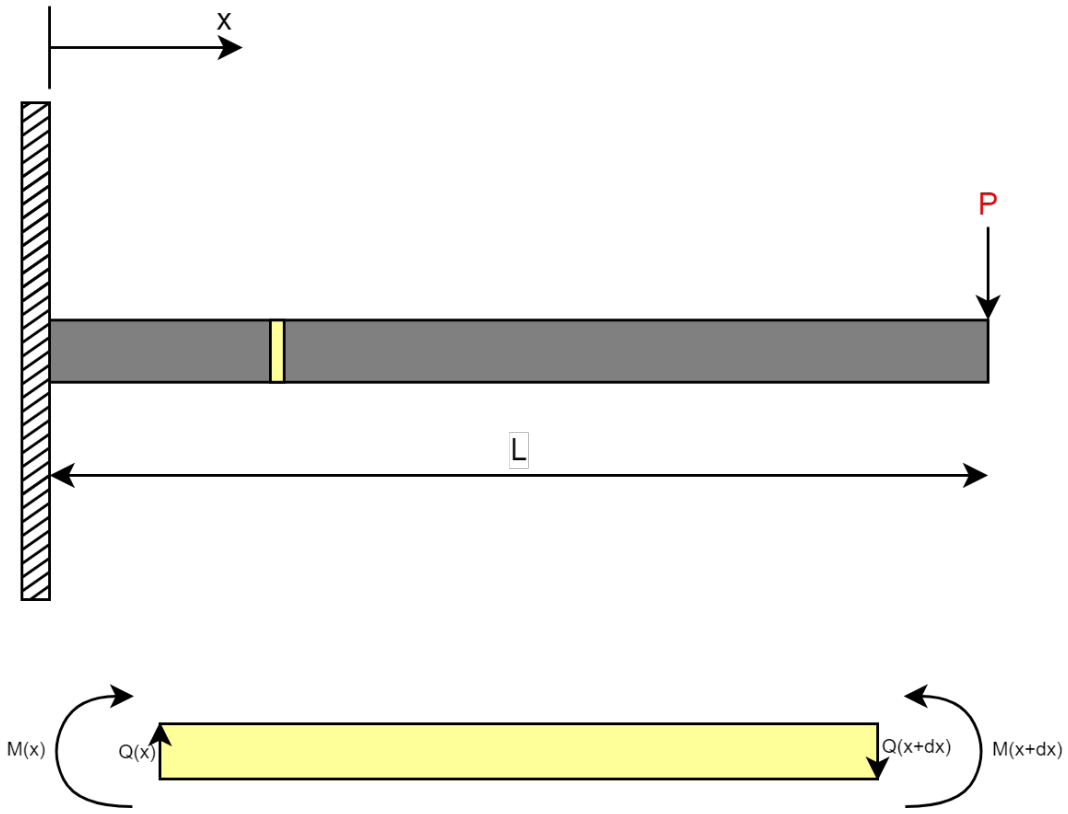

Figure 9: Free body diagram for cantilever beam

From the free body diagram equilibrium equations can be found,

$$
\begin{aligned}
M(x) &= P(L-x), \\
Q(x) &= P,
\end{aligned}
\tag{20}
$$

as well as boundary conditions due to the clamped side,

$$
\begin{aligned}
\frac{dw(0)}{dx} &= \alpha(0) = 0, \\
w(0) &= 0.
\end{aligned}
\tag{21}
$$

Using the first equilibrium equation and the first equation from 16 a differential equation for equilibrium is found,

$$
-EI\frac{d\alpha}{dx} = M(x) = P(L-x). \tag{22}
$$

This equation can be integrated and subsequently solved using the first boundary condition,

$$EI\alpha(x) = -\frac{Px(2L-x)}{2} + C_1 \rightarrow EI\alpha(x=0) = 0 = -\frac{0P(2L-0)}{2} + C_1 \rightarrow C_1 = 0. \tag{23}$$

With the first equation solved the second equation from 16 can be solved as well, by integrating and rewriting it to give,

$$\frac{dw}{dx} - \alpha(x) + \int \frac{p(x)}{\kappa GA} = 0 \rightarrow \frac{dw}{dx} = -\frac{Q(x)}{\kappa GA} + \alpha(x). \tag{24}$$

Substituting in the solution for $\alpha(x)$ and the equilibrium equation for $Q(x)$, which leads to,

$$\frac{dw}{dx} = -\frac{P}{\kappa GA} - \frac{Px(2L-x)}{2EI} \rightarrow w(x) = -\frac{Px}{\kappa GA} - \frac{Px^2(3L-x)}{6EI} + C_2. \tag{25}$$

Now applying the boundary condition that $w(x) = 0$ gives the equation for the displacement of a beam according to Timoshenko,

$$\begin{aligned} w(x=0) = -\frac{0P}{\kappa GA} - \frac{0P(3L-x)}{6EI} + C_2 \rightarrow C_2 = 0, \\ w(x) = -\frac{Px}{\kappa GA} - \frac{Px^2(3L-x)}{6EI}. \end{aligned} \tag{26}$$

Using the equation for displacement it can be shown that for two prototypes which have the same material properties and boundary conditions the equation can be reduced to,

$$w(x) = -\frac{C_3}{\kappa A} - \frac{C_4}{I}, \tag{27}$$

where C_3 and C_4 are constants which represent the material properties and the boundary conditions. In this equation it can quickly be noticed that the only terms left are the geometry dependent terms. All of the geometry dependent terms are in the denominator, which means that for an increase in any of the geometry dependent parameters a decrease in deflection can be expected. This decrease in deflection means that the bending stiffness of the prototype is higher and is thus able to provide larger forces in an actuator design. The design challenge is to create a prototype with a maximized area, shear coefficient and second moment of area. However, increasing the area for this purpose also directly increase the amount of air consumed by the prototype and is thus not advised as the optimization problem is to have the highest stiffness per volume air consumed, which is directly proportional to the surface area. The shear coefficient can be found according to equation 18. The maximum and minimum values for κ can be determined. This can be visualized by creating a surface plot of the function, with on the one axis m and on the other axis ν. This graph can be seen in Figure 10.

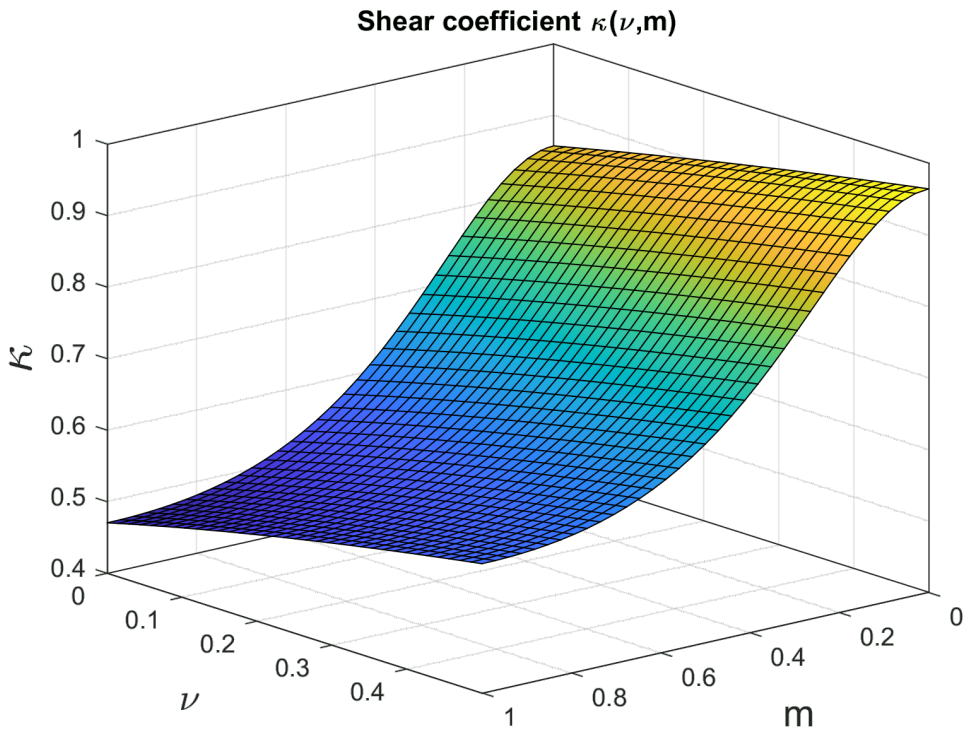

Figure 10: 3D surface plot of the shear coefficient as function of ν and m

From this graph it can be seen that the highest value for κ is always achieved for highest values of ν and for the lowest value of m. This means that highest bending stiffness is achieved when cylinder is solid, which both optimizes the surface area as well as the shear coefficient. Having the highest value for both the surface area and the shear coefficient requires a higher volume as well, this means that even though the stiffness is increased, the strength per volume consumed does not have to be higher.
The second term in equation 27 only depends on the second moment of area and a constant which entails all the material properties and boundary conditions. This term is also inversely proportional to the displacement, meaning that an increase in the second moment of area would results in a decrease in displacement. Similarly to how the buckling strength is increased by increasing the second moment of area, the bending stiffness is increased when the second moment of area is increased. This means that a similar conclusion can be drawn as before, which is that the optimal geometric configuration is a infinitesimally thin wall, which achieves the highest ratio of $\frac{I}{A}$ and thus the highest bending stiffness per unit air consumed by the prototype. In practice this will not be the optimal configuration due to other effects that will become dominant when the wall thickness decreases too far.
In equation 26, the first term only has a small impact on the overall deformation if the beam is long and slender. If the beam is short and relatively thick, like the produced prototype this term has a significant impact on the final solution. When the beam becomes longer and more slender the solution approximates the solution from the well known Euler-Bernoulli beam equation and this term can be neglected.
The equations used above are however only valid for solid materials. For inflatables the equation changes slightly to include terms which account for the internal pressure and also include the pressure dependency of the materials. The pressure dependency of the materials is however ignored for now. Both cylinder designs are created from the same material and the exact material properties are hard to determine. The equation which describes the displacement of an inflatable beam can be found in [Le van and Wielgosz, 2005], [Le van and Wielgosz, 2006], [Nguyen et al., 2015] and is also shown below, albeit with the variables changed to match the previous used variables.

$$w(x) = -\frac{Px}{F_p + \kappa G S_o} - \frac{P}{(E + F_p/S_o)\, I_o}\left(\frac{L_o x^2}{2} - \frac{x^3}{6}\right), \tag{28}$$

where F_p is the force due to the internal pressure, S is the cross-sectional area of the walls, while the other variables are the same as before. The subscript $_o$ denotes the reference geometries, which are pressure dependent. However, as mentioned before, this pressure dependency is ignored for now. This equation shows very large similarities to the previously mentioned Timoshenko beam equations 26. The difference is the added pressure term in the

denominators. Furthermore the cross-sectional area changes as well as the second moment of area, since these are based on the wall thickness here, rather than full geometry. The force F_p is the force applied to the end of the cylinder due to pressure inside, which can be defined as,

$$F_p = pA_o, \tag{29}$$

where p is the internal pressure and A_o is the cross-sectional area, similar as was used for the Timoshenko beam, which also includes the inflated part. The addition of the pressure dependent terms changes the equation such that the pressure dependent terms can be interpreted as changing the material properties. An increase in the pressure can be interpreted as an increase in the bending and shear stiffness of the beam.

3 Methodology

In the previous section different theoretical calculations have been performed, which will be modelled for the created prototypes in upcoming sections. These models will be compared with the results from the created prototypes. Multiple different prototypes with different production strategies have been explored to try and achieve the designed volume reduction without reducing the output force of the prototype. The explored production methods mostly serve as a prove of concept and better production methods can be explored if the hypothesis of this paper is confirmed.
After choosing a suitable production method for the prototypes, each of the produced prototypes of the cylinders are subjected to an axial load test with the same test settings. The performed tests are continued until either the maximum load, maximum displacement or buckling is achieved. Buckling is a sudden change in shape caused by reaching a critical load level, when the load is increased gradually. Loading beyond the point of buckling can cause the complete loss of being able to carry the load, which is why the test was ended shortly after reaching the point of buckling.
Furthermore, actuation speed tests are conducted to show the achieved increase in inflation speed by the geometrical change proposed. During this test the time to reach inflation of the different prototypes is compared to show the benefit of the reduced volume of the proposed design changes.
Lastly, bending tests are performed on the produced prototypes as well to characterize the bending strength of the original solid cylinder design as well as the newly proposed hollow cylinder design. The results from all these tests will also be compared to the theoretical models. Comparing these results should show the validity of the models, help locate potential issues in the test setup and find possible further improvements that can be made to the prototypes for even better results.

3.1 Prototype designs

Different designs and production methods have been explored to produce a representative prototype. All of the proposed prototypes consist of a strain limiting layer in the form of a woven fabric in combination with a airtight material inside to form the air pocket.
The first prototype design was created using a cylinder with a woven double walled design, where the cylinder was woven using small ribbons, as can be seen in Figure 11. Figure 11b shows the concept for a woven cylinder design, where the yellow ribbons would be double walled to allow the air pocket to be inserted in between the two walls. In Figure 11c the achieved prototype can be seen, where the downwards ribbons are double walled. Figure 11a shows a schematic overview for the design. This design however, does not achieve the wanted behaviour since there are still areas where the air pocket can inflate without any strain limiting, this is most clearly seen in the last section cut from the schematic overview. All the places on the yellow double walled ribbon where no red ribbon is present allows for the air bladder to expand unrestricted. During inflation of the air pockets they would only have been supported partially by the ribbons in the radial direction. This is due to the nature in which weaving is used, even in a double weaving design. The non supported parts would have been able to inflate too easily and the strains from the air pockets would have been too high, causing ruptures/explosions of the material of the air pockets, especially at higher pressures. Furthermore, if this problem could have been solved, a similar problem would still remain where there are small gaps between each of the rows of the woven ribbons, where the air pocket would be able to achieve higher strains, which would once again result in ruptures and explosions.

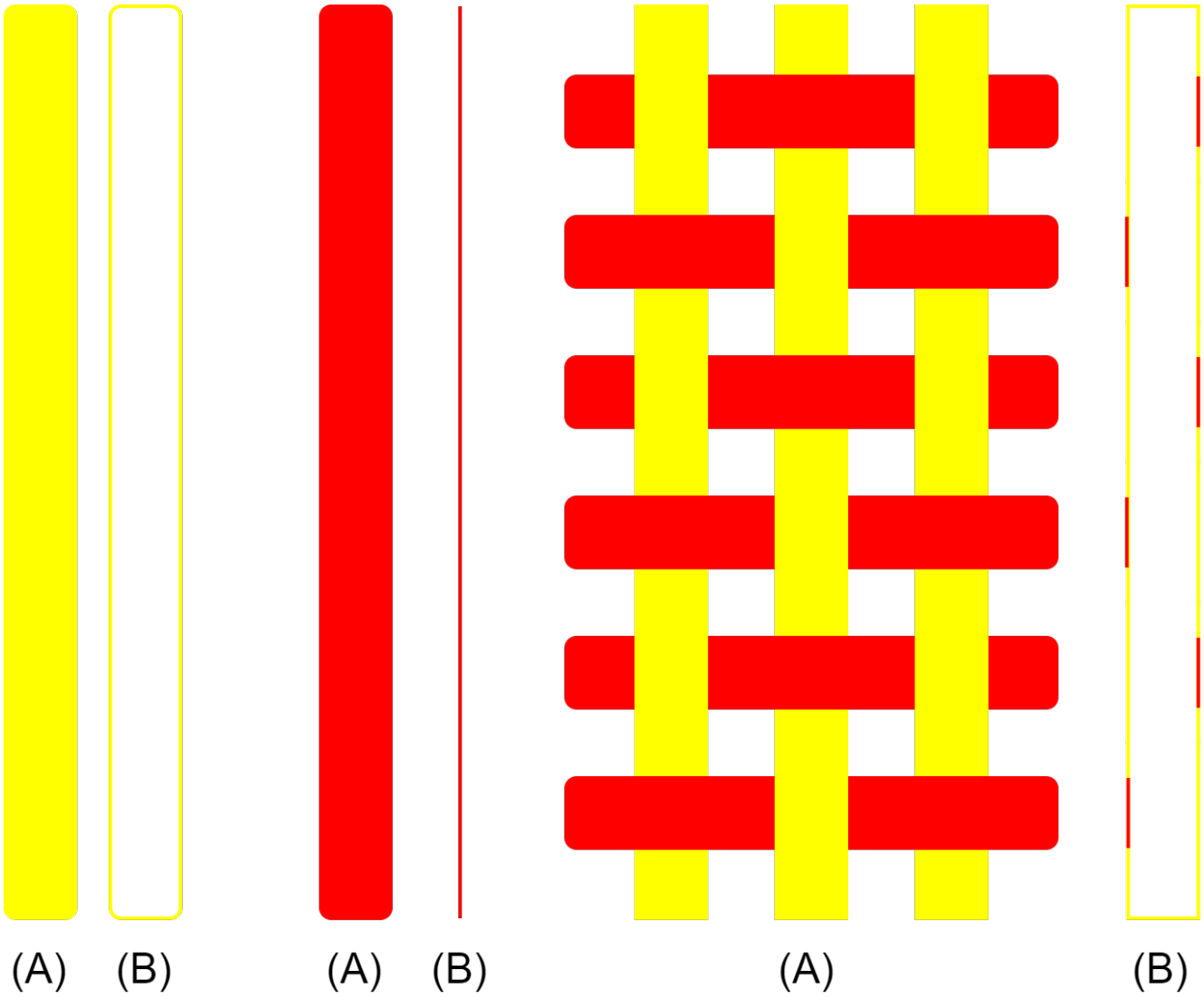

(a) Schematic overview of woven cylinder design concept. (A) Front view of ribbons, (B) Side view of ribbons, where the white area inside the yellow ribbon is hollow.

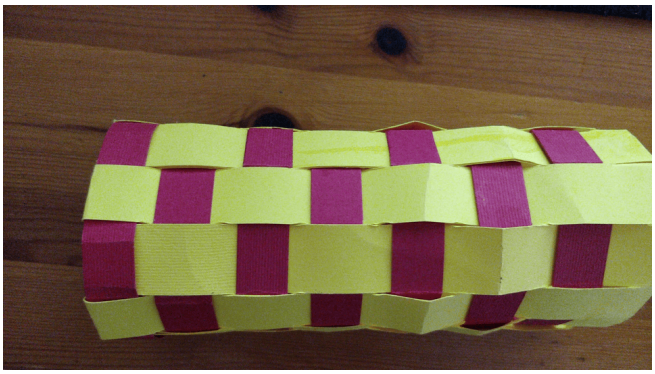

(b) Concept design for a woven hollow cylinder

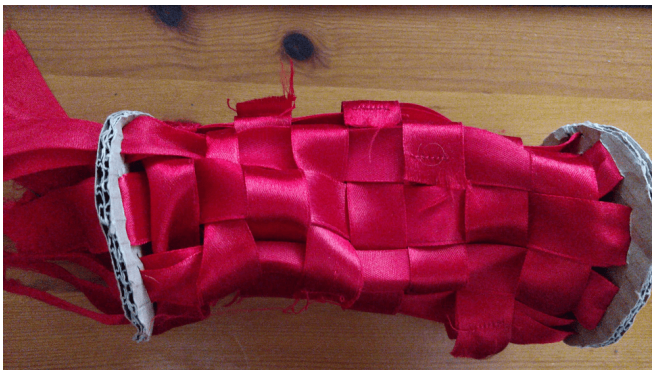

(c) Prototype design for a woven double walled hollow cylinder

Figure 11: Woven hollow cylinder design concept

The next proposed design was using a waterproof fabric impregnated with thermoplastic polyurethane (TPU). This design process consisted of cutting two sheets of the impregnated fabric with the same dimensions, consecutively melting the two sheets on top of each other, using a heat press, with a sheet of baking paper with a certain pattern between them. The baking paper sheet prevents the melting together of the TPU at the places where the baking paper is located. This method has been used in multiple previous studies as well [Thalman et al., 2019], [Natividad

et al., 2017]. A schematic overview of the design can be seen in Figure 12a. This method allows for making a flat airtight sheet with pockets that can be filled with air. When air is pumped into the designed pouch, each of the pockets takes a circular shape because a circle has the best area to circumference ratio. When the two ends of the sheet are molten together as well, the sheet now forms a cylinder with inflatable walls, of which an schematic drawing can be seen in Figure 12b. The problem with this design is that the material ruptures relatively easily at the edge of the molten lines when it is inflated, as well as the delamination of the sheets. A schematic overview of the weak points in the design can be seen in Figure 12c. These two problems together make that the cylinder fails at relatively low pressures. The performance of this design was improved by increasing the wall thickness between each of the cylindrical air pockets. The increased wall thickness solved the problem of the delamination of the sheets, however the rupture which occurred at the edge of the melting line between each of the pockets still remained. A visual representation of the achieved design can be seen in Figure 13.

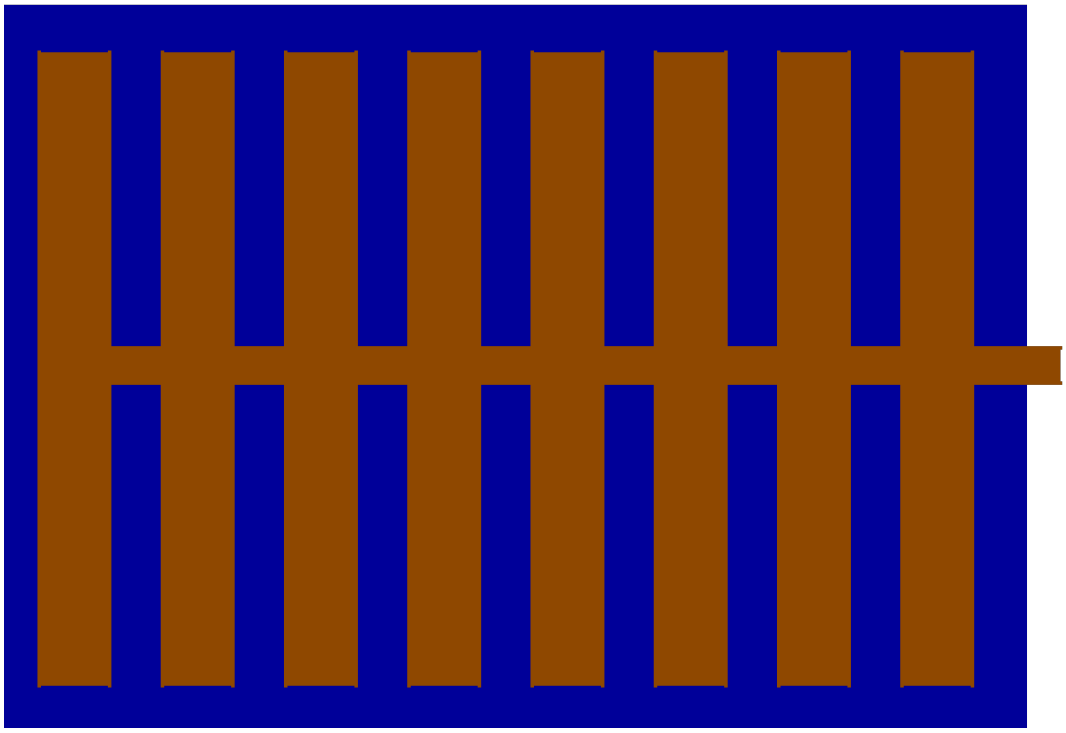

(a) Schematic overview of TPU impregnated fabric hollow cylinder design

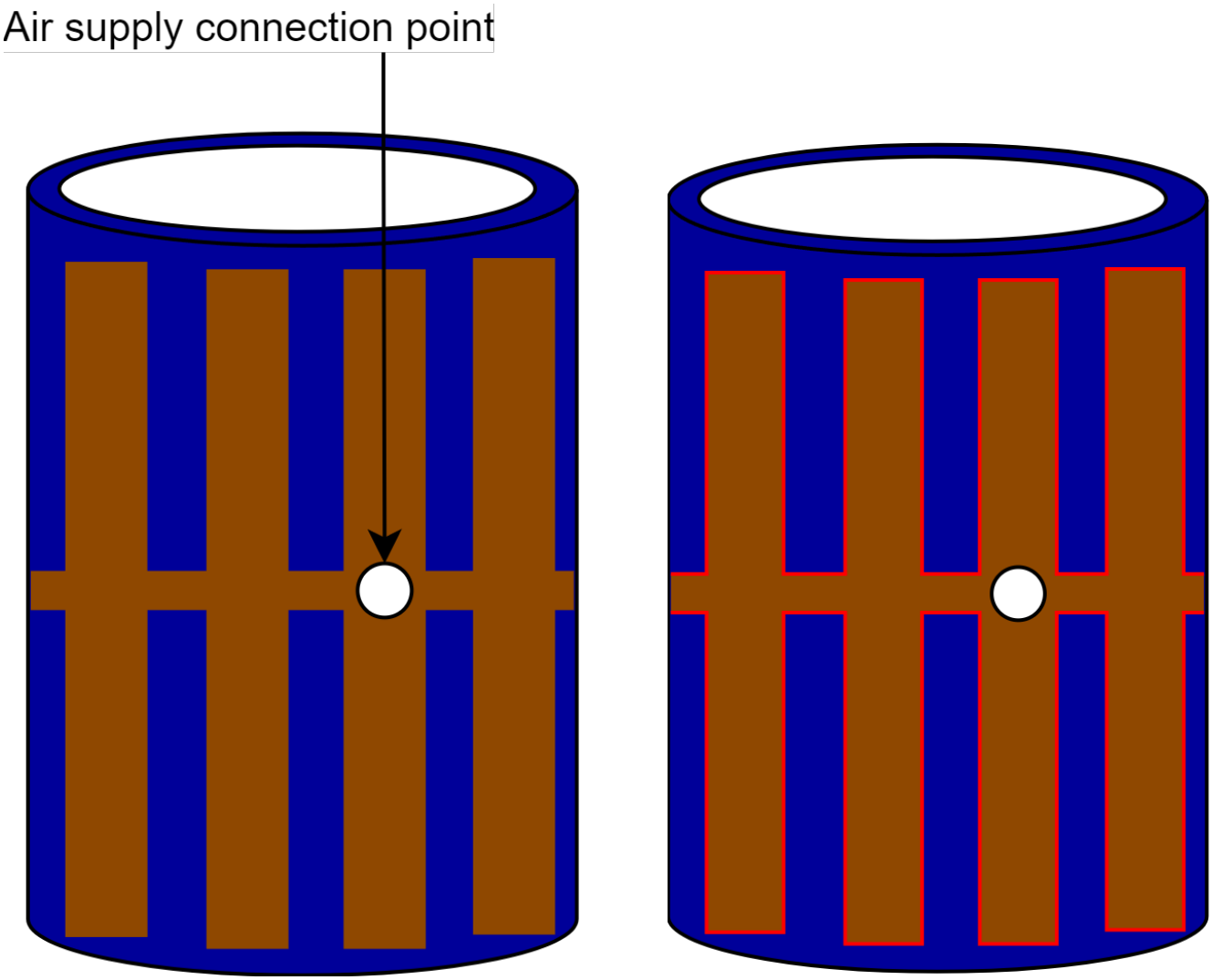

(b) Schematic over of TPU impregnated fabric hollow cylinder

(c) Red lines mark the weak points in the design

Figure 12: Schematic overview of hollow cylinder created using a heat press and the TPU impregnated fabric[24]

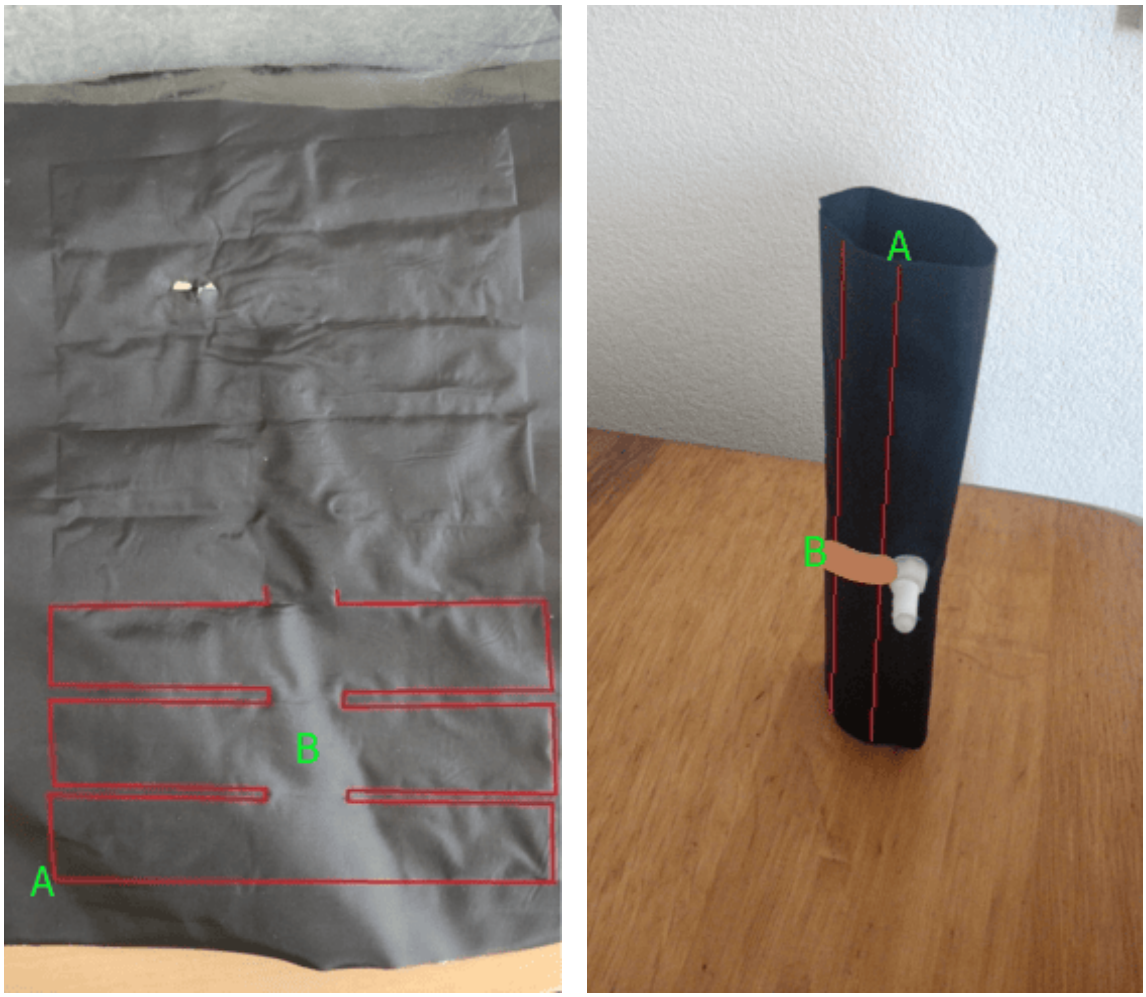

(a) Prototype design using a heat press. (A) The outline formed by the baking paper sheet of non melted material. (B) Area inside the red lines is the shape of the baking paper.

(b) Prototype design using an impulse sealer. (A) Weld lines formed by the impulse sealer. (B) The brown line is the baking paper which is used to create interconnections of the created chambers.

Figure 13: Prototype design fabric impregnated with TPU

A similar design was created using an impulse sealer, the PFS-400, which is normally used to seal plastic bags. The created prototype can be seen in Figure 13b. The red lines in this image represent the seal lines which were created using the impulse sealer, whereas the much thicker brown line represents the small strip of baking paper which is between the two sheets of the fabric. The piece of baking paper allows the different pockets to be inflated using a single inflation point on the prototype. Using this impulse sealer instead of having to cut the entire shape out of baking paper saved a considerable amount of time, but at the same time this also reduced the overall strength of the design, making the problem of rupture and delamination even more prevalent.
The next that was created is a cylinder from textile using sewing and filling the void of this cylinder using balloons as air pockets. Using a relatively thick textile, a very strong cylinder can be created, but this also increases the stiffness when the balloons are not inflated. In general, soft pneumatic actuators aim to have the stiffness of the non inflated actuator to be as low as possible, while the stiffness should be as high as possible in the inflated state. To quantify this a bit more, most designs compare the non-inflated stiffness with the stiffness in the inflated state and use difference between these as a measurement of how well the design performs. This means that the lowest possible non-inflated stiffness or the highest inflated stiffness are not necessarily the best, if the difference between the inflated and deflated state for this design would be low. If this design were to be implemented in an application, a suitable textile should be selected, which can withstand the forces in the inflated state, while keeping the stiffness as low as possible in the non inflated state. This is however highly dependent on the application of the soft actuator.

3.2 Design of the textile sleeve

To be able to create a prototype using a textile cylinder with balloons for air pockets, a fabrication method would have to be designed. Creating a hollow cylinder using sewing is much more difficult than creating a solid cylindrical pouch. The design from the first mentioned prototype was used as inspiration for this prototype, where hollow shafts had to be created in which the balloon can be inserted. The strain had to be limited in all directions by the textile or some other method to avoid rupture. This was achieved by using two sheets of textile sewed in a pattern, which can be seen in Figure 14a. The pattern starts with the part of the inner wall of the chamber. The textile has a folded part which forms the side wall of the chamber, thus allowing the textile to move to the other wall and back down again, which is represented by the mountain like shape in the schematic overview. This is a repeating pattern for as many air pockets as desired, which is ten for this specific prototype, which can be seen in Figure 15a. Note that the number of chambers in Figure 15a is larger than 10, because the picture is from an older design that used a larger number of chambers. To create the prototype as seen in the figure, the other wall had to be attached to the shape presented in Figure 14a. This is done by sewing over the blue and yellow dashed lines in the figure, for the entire length of the cylinder. In each of the pockets shown, an air bladder will be inserted to allow for inflation. In the initial design there was no difference between the wall length on the inside and the outside of each of the pockets, which results in each of the pockets being square. This results in a non circular shape when the two ends of the sheet of chambers are sown together. Having a non circular shape results in problems during inflation, because the inside of the hollow cylinder has a circumference which is too large. To overcome this problem the lengths of the inner, side and outer walls of each of the pockets were scaled such that the final shape is cylindrical upon inflation. This was achieved by assuming that the inner and outer walls of the cylinder are two concentric cylinders with different diameters when the air pockets are inflated. The out diameter of the cylinder was set to 9 cm, while the inner diameter was 5 cm, leaving the side walls with a length of 2 cm. Using the circumference of a cylinder being πd and the information that there are 10 chambers, results in the length of the walls being 1.57 cm and 2.83 cm for the inside and outside respectively, which can be seen in Figure 15b.

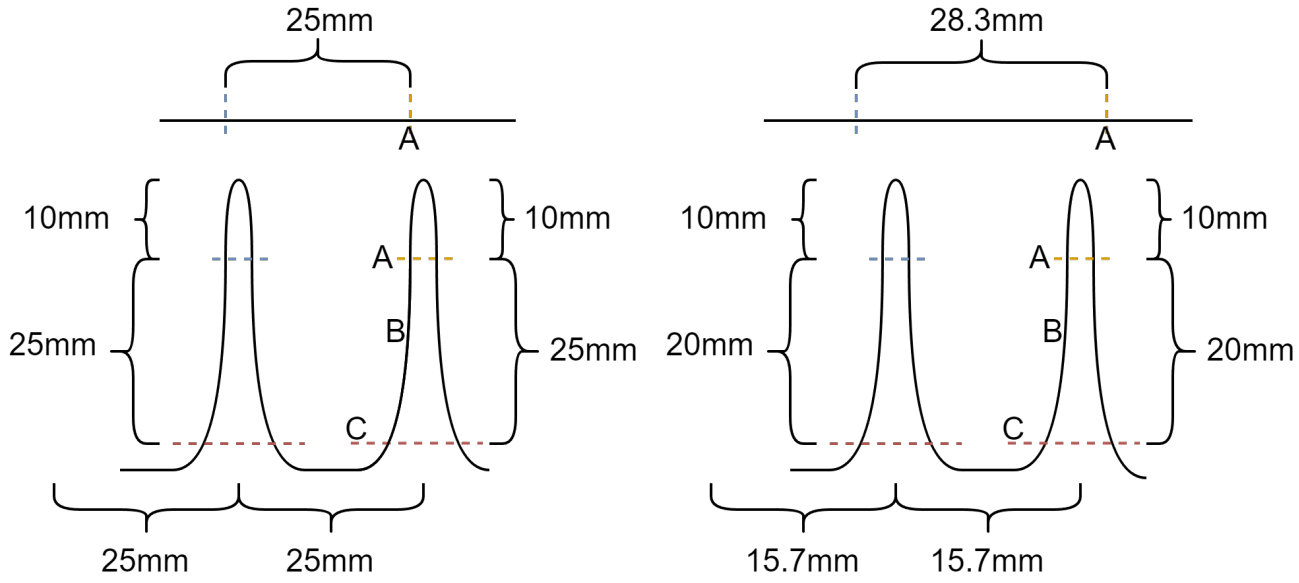

(a) Schematic overview of the chamber design for the hollow cylinder

(b) Schematic overview of the improved chamber design for the hollow cylinder

Figure 14: Schematic overview of the design for the hollow cylinder. Both lines marked with (A) are a single sewing line that connects both sheets. (B) Inner walls of hollow cylinder connecting the inner and outer cylinder. (C) Sewing line used to form inner cylinder of the textile sleeve.

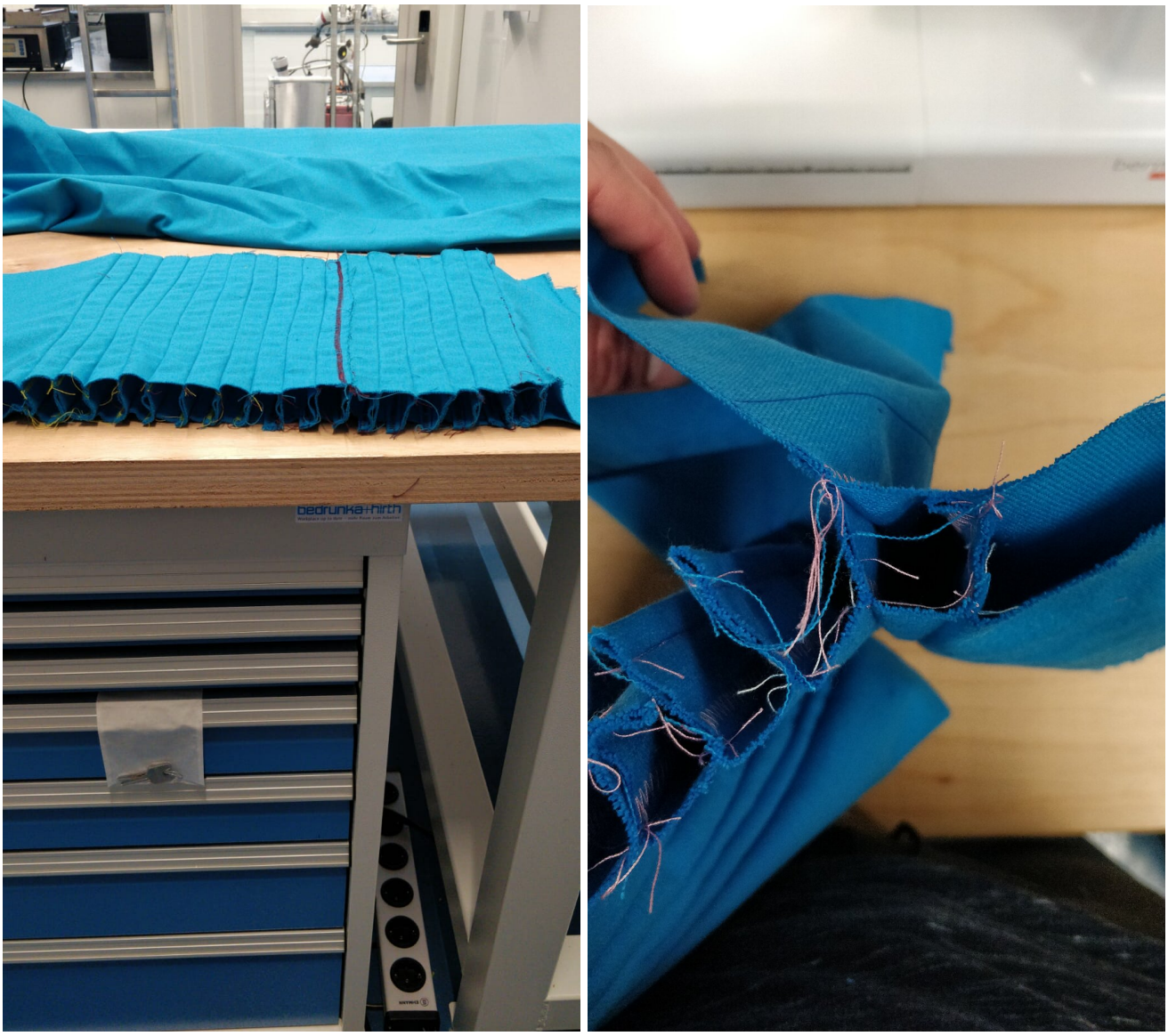

(a) Side view of the hollow cylinder before attaching start and end together

(b) Side view of the improved chamber design for the hollow cylinder

Figure 15: Side views of the hollow cylinder design

3.3 Limiting strain in longitudinal direction

In order to limit the strain of the air pockets in the longitudinal direction, the top and bottom of the cylinder will have to be closed off as well. There are several options available to do this, including sewing them closed, leaving only a small hole for the air supply or creating some kind of disk that can be inserted and attached, with holes in it for air supply tubes. The first solution, sewing the top and bottom closed, seems to achieve the goal with relatively low effort and no extra parts. However, applying this simple strategy proved to be very difficult to achieve. The first problem that arose when trying to sow the top of the cylinder closed is that a small hole has to be left for the air supply to the air pocket. The air supply to the air pocket is achieved by small tubes, which means that a hole with the same diameter as the air tube has to be left open when sowing the top and bottom. This is hard to do when sewing by hand, but it is achievable. The fit between the hole and the tube however, has to be very tight, otherwise the air pocket will try to push the tube out of the fitting and try to expend through the hole as well. If the balloon starts to expand out of the hole, the strain is no longer limited and the balloon will rupture. The major upside of sewing the top and bottom of the cylinder closed with respect to creating a disk which is inserted, is that the inserted disk will be solid and hard, which transforms the fully soft actuator into a hybrid soft actuator, which might not be desired depending on application. For this research it was decided to still go for the cylindrical disks on the top and bottom, because the goal of this research is to determine the characteristics of the new soft

pneumatic actuator design. For this purpose having a hybrid soft actuator is fine. For specific applications and even more so if the improved design is used in mass fabrication, the disks can be replaced by a sewing technique or even an entirely different technique can be used. The sewing technique would be a lot easier to apply to mass fabrication, since robotic sewing can achieve a much higher accuracy, making it a feasible solution. It would also be cheaper in production than using the disks, which involves extra material costs and longer production times.
The chosen solution for closing the top and bottom of the cylinder are 3D printed disks, which can be inserted into the textile sleeve and attached to the sleeve to prevent separation. The disks are designed using Solidworks and are shown in Figure 16, for the exact dimensions, other views and the corresponding Solidworks files, see Appendix A.1.

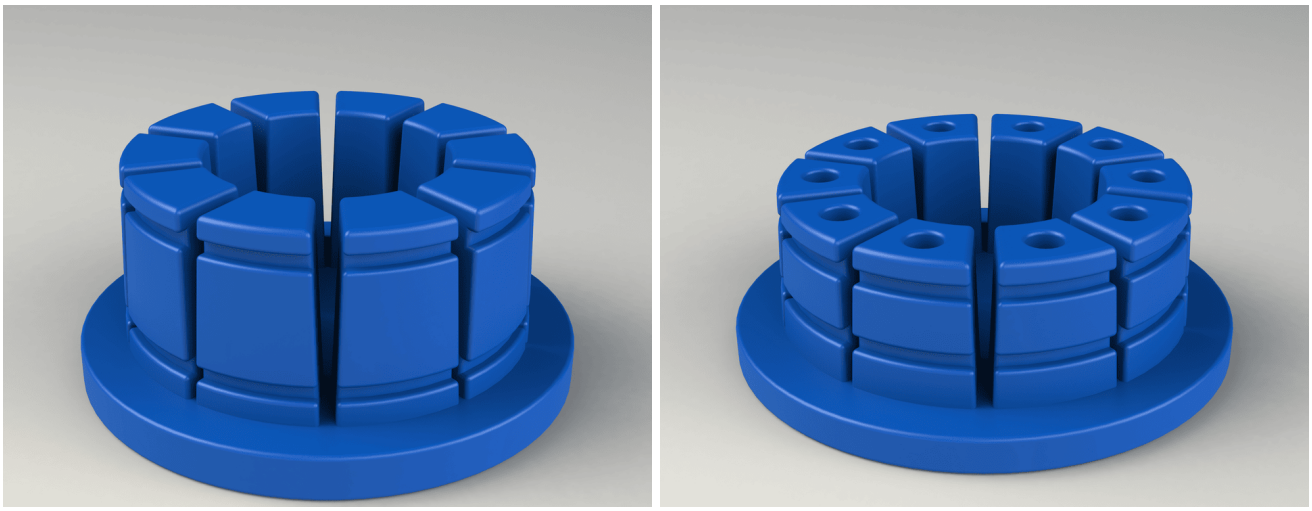

(a) Bottom disk

(b) Top disk, which has the air supply holes

Figure 16: Top and bottom closing disk for the hollow cylinder

For the disk of the hollow cylinder each of the upstanding parts are inserted into a chamber. The air supply tubes are passed through the holes in each of the upstanding parts and come out the top of the disk where they are attached to a 10 WAY PNEUMATIC UNI-FIT MANIFOLD, 10X6MM^{TM}. The 10 way manifold is also attached to the pneumatic air source and the pressure gauge, which both use the 10 mm fittings. The slits which can be seen on the outside of each of the standers are there to increase the grip of the zip ties which are used to secure the textile sleeve to the disks. This combination of zip ties and slits in the disks however, proved to not be secure enough for higher pressures, which is why it was decided to add an additional constraint. Two hose clamps were attached to each other, to form a larger diameter hose clamp, which in turn was attached between the zip ties. Two hose clamps were used, because the correct size hose clamp was not available at the time the tests were performed. The added hose clamp was able to be tightened with larger forces, allowing for a better connection between the textile sleeve and the disk, leaving no movement. It does however have to be noted that some caution is to be used when tightening the hose clamps, to prevent damage to the standers of the disk. The closing of the hose clamp is able to provide forces larger than the standers are able to withstand, which would result in breakage of the 3D printed disk, if the hose clamp is closed with too much force. Each of the standers are tapered allowing them to be inserted more easily in each of the chambers of the textile sleeve. The textile sleeve is slit onto the disk until it cannot be moved further upwards anymore, creating a tight hold between the disk and the textile sleeve. The gap between each of the standers is defined as being 2°, except for one gap which is double the width, 4°. One of the gaps is larger due to the production method used for the textile sleeve, which consists of first creating each of the chambers in a line, after which the 2 ends of the created sheet are sown together. The sowing together of the two ends causes the point where they are joined together to be twice as thick as the walls of all the other chambers. The holes for the air supply tubes are also tapered which serves the same purpose as the tapering of the standers, namely to allow for easy insertion and subsequently a tight fitting between the hole and the tube.

3.4 Design of air pockets

The sleeve of the cylinder has been designed, however the textile is not air tight, thus air bladders will have to be designed that can be inflated. A few solutions will be proposed here, with each their advantages and disadvantages. The first proposed design is creating air bladders using two sheets of silicon rubber. The two sheets are fixed together with either of the two previously proposed techniques for the TPU material in Section 3.1, using either the heat

press or the impulse sealer. Using the impulse sealer the air bladder can be created relatively fast by creating a line weld on each of the four sides of the rectangular air bladder. One of the short sides will leave a small opening for the air supply tubes, which is achieved by putting a small piece of baking paper between the two layers when applying the line weld. This hole can be slightly smaller than the diameter of the tube, due to the highly elastic properties of the silicon rubber. This design for the air bladder results in the same problems as for the prototype design, where the weld lines are the weak points, which separate, creating leakages.
Using the heat press instead of the impulse sealer, it takes slightly longer to achieve a prototype, but it also offers a much stronger seal. The sides of the air bladder are no longer the weak point when being inflated. To be able to supply air to the air bladder, a small piece of baking paper was also left on one of the short sides of the two sheets, similar to the impulse sealer method. The achieved shape for the air bladder is very similar to a hot water bottle. The air bladder can be seen in Figure 17, where the blue part on the left hand side, is part of the air supply tube that is inserted into the air bladder. The designed air bladder seemed very promising, because it can be created in any size that is preferred and can achieve high strains. However when the air bladder is inflated inside the textile sleeve, the air bladder ruptured at relatively low pressures. The rupture of the air bladder tends to always happen at the same spot on the air bladder, pointing to underlying problems with the design. The most likely cause of the rupture of the air bladder is the high friction between the textile sleeve and the air bladder. The relatively small area between the inner and outer wall of the textile sleeve, leaves little room for the air bladder to move in. The air bladder first expands radially causing very high friction between the textile sleeve and the air bladder, subsequently when the pressure is increased further the air bladder tries to expend further towards the outer most edges at the top and bottom of the cylindrical pocket. This expansion causes very high local strains, due to the blocked movement, resulting in ruptures at the bottom of the air bladder. The shape of the air bladder has a slight mismatch with the shape of the cylindrical pocket in which it is inserted because the pocket has the same shape over the entire length, but the air bladder has a line shape at the top and bottom due to the welding. A visual representation of the misfit between the cylindrical pocket and the air bladder can be seen in Figure 18. For the figures it has to be noted that the mismatch between the air bladder and the textile sleeve is exaggerated. Furthermore, it can be seen that the main mismatch will be around the very top and bottom of the chamber, due to the weld lines that are located there. If the diameter of the air bladder is increased, the problem of the mismatched shape in the radial direction will become much less noticeable due to lower required strains. A similar conclusion might be formed for the longitudinal direction by increasing length of the air bladder. This was attempted by pre-straining the air bladder and having the length be sufficiently long. The mismatch problem was partly solved by pre-straining the balloon, by having it attached at the top and bottom of the textile chamber, however the rupture point moves from the bottom of the air bladder to the top near the air inlet. This is most likely caused by the same underlying problem where the air bladder tries to match the shape of the textile chamber, which results in high local strains causing rupture. This problem will remain due to the air inlet which is installed into the top disk and the line weld at this same point on the air bladder, which limits the influence from adding extra length to the air bladder and the high local strain to fill the very edges will remain.

Figure 17: Custom silicon air bladder

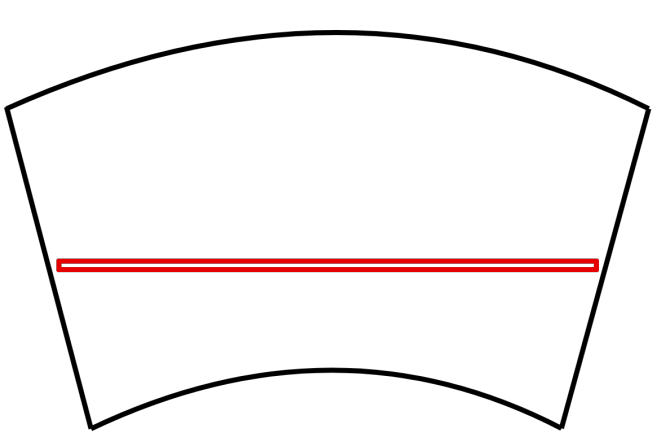

(a) Top view of a chamber, with the deflated air bladder in red

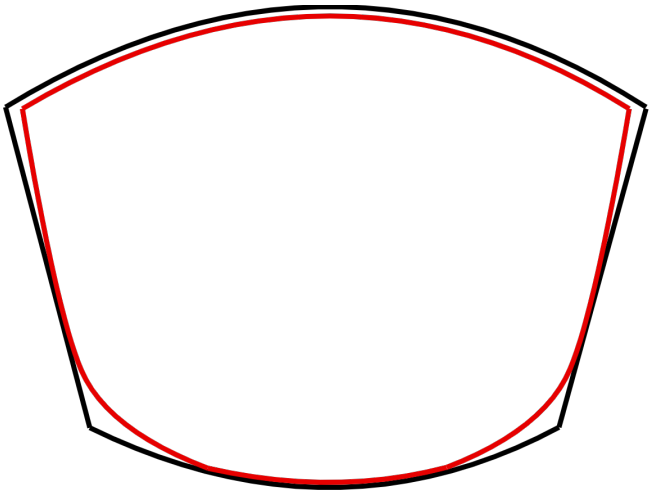

(b) Top view of a chamber, with the inflated air bladder in red

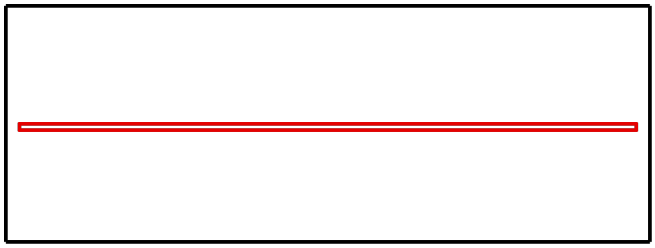

(c) Side view of a chamber, with the deflated air bladder in red

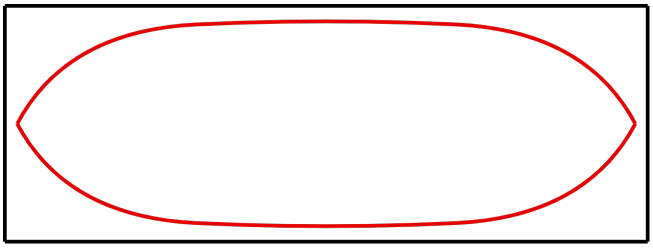

(d) Side view of a chamber, with the inflated air bladder in red

Figure 18: Schematic overview of a textile chamber and the air bladder in both inflated and deflated state

A different air bladder was proposed to try and solve the previously experienced problems with high friction and local strains. Creating air bladders from the textile impregnated TPU material should result in a much lower friction between the textile sleeve and the air bladder, since the textile impregnated TPU has a smooth surface and is far less sticky. The textile impregnated TPU air bladder however, has some limitations of its own, including small strains and difficulty getting an airtight fit with the air supply tube. The low strains are not preferred, but should not pose any problems during inflation and usage of the prototype. The downside of only allowing small strains is that the designed air bladder should very closely match the shape of the textile chamber or should even be slightly larger since the strain is still limited by the textile chamber. This might however cause some rimpling of the air bladder, with unknown consequences. It is however expected that this rimpling will not result in any noticeable effects. The leakage of the textile impregnated TPU air bladder is located at the connection point between the air supply tube and the inlet of the air bladder. This is because the TPU material does not act elastic like the silicon rubber air bladder which gets a tight fit around the air inlet tube. This problem can be solved by using a combination of rope with tape to get a tight fight around the air inlet tube. The air inlet tube itself is from a soft plastic material which can be compressed relatively easily, but inserting a piece of a hard plastic tube inside, allows for a tight fit to be created between the air bladder inlet and the air supply tube, since the hard plastic tube blocks the compression. With the air leakage problem solved, the problem with the limited strain still remains, which can be solved partially by using a slightly larger air bladder than the textile chamber. This however still leaves a challenge to fill the outer edges of the textile chamber, similar to the silicon air bladder, since the sides of the air bladder are lines, whereas the textile chamber is shaped more like a circle. Even if this is solved by using a larger length and diameter air bladder the problem at the top remains. The air inlet is flush with the disk, which would mean that in order for this to work, the top of the air bladder should not inflate, but be compressed by the inflated part below.

The problem with the previously proposed solution is their high friction and the mismatch between the shape of the textile chamber and air bladder. To solve this problem condoms were proposed as a possible solution. Condoms are able to achieve very high strain, they are lubed to reduce friction and their inflated shape is a close match to a cylinder. The lube on the condoms however, did not solve the problem with the friction, since the lube is absorbed by the textile and did not lower the friction between the condom and the textile chamber. The ability to achieve high strains and the good match between the shapes still seemed promising. The achieved pressures with the condom, were much higher than those with the previously proposed solution, however they were still relatively low when the condom ruptured, at around 80 kPa. The ruptures of the condom were once again located at the extremities of the air bladder, namely the top and bottom. The rupture was most likely caused by the high friction between the condom and the side walls, causing the condom to rupture when trying to match the shape of the textile chamber. The local strains become very high when the condom is stuck to the wall and than at higher pressures tries to match the shape of the textile chamber more closely.

Another proposed solution is to use party balloons as air bladders. The chosen balloons are Qualatex traditional assortiment. The party balloons can be bought from various party stores or online, requiring no work to be produced while being low cost. The balloons also require relatively low effort to be attached to the air supply tube. This was done by first cutting off the very top of the balloon, because this part is slightly thicker and would cause problems with insertion into the holes of the top disk of the cylinder. Next the air supply tube is inserted into the balloon, which is attached similarly to how the TPU air bladder was attached, namely using a combination of robe and tape. Also similar to the TPU air bladder, a hard plastic tube is inserted into the soft air supply tube again to allow a secure attachment of the rope to the balloon, without closing the air supply tube due to the compression. The downside of using the party balloons is that their behaviour is not consistent between balloons and sometimes not even consistent between different inflation cycles of the same balloon. The first inflation cycle of the party balloon requires significantly higher pressures than consecutive inflation cycles, which is why the balloons are inflated once before they are inserted into the textile sleeve. The non consistent behaviour of the balloons should however have no influence on the results of the tests, because the tests are quasi-static, with a given start pressure, after which no further air is added.

The balloons also suffered from a similar problem the silicon rubber air bladders did, which is that they exploded at relatively low pressures. This was most likely caused by the fact that the balloons are longer than the textile chamber which means they are shoved into the chamber. This combined with the way the balloons inflate, most likely caused them to rupture at low pressures. The balloons do not inflate evenly across the entire length of the balloon, but instead, the inflation propagates along the length of the balloon from an initial spot, which is almost always located at the beginning of the balloon. This once again led to a similar issue that affected all the other designs: the friction between the textile walls and the balloon remained relatively high. When combined with the balloon's propagating behavior, it resulted in very high local strain, leading to ruptures. To address this problem, a slight modification was made to the design, similar to the silicon rubber bladder, which is that the balloons were pre-strained. This solution could also have been applied to the condom design, however the balloons are thicker

than the condoms, which makes them more robust for ruptures. This pre-straining was done by first inflating the balloon outside of the textile chamber to determine the length of the balloon that was needed to fully fill the textile chamber. At this point a rope was tied around the balloon to make sure the balloon would not be able to inflate past this point. This was done for all the balloons. After this the balloons were inserted into their respective textile chambers and the top of the prototype was attached to the textile sleeve with the zip ties. The balloons were pulled out of the bottom side of the textile chambers until the point where the rope was wrapped around the balloon. With all of the balloons strained out of the bottom side of the textile sleeve, the bottom disk was inserted to the textile sleeve and the zip ties were attached to secure them together. Due to the problem of the separation of the disk from the textile sleeve at higher pressures, it was decided to also use a hose clamp to get a more secure connection, as was described previously in Section 3.3. The balloons are kept in place by the zip ties, which causes them to be pre-strained inside the textile sleeve. The final prototype can be seen in Figure 19, in both the deflated and inflated state. It should be noted that depicted prototypes are different iterations of the same hollow cylinder prototype.

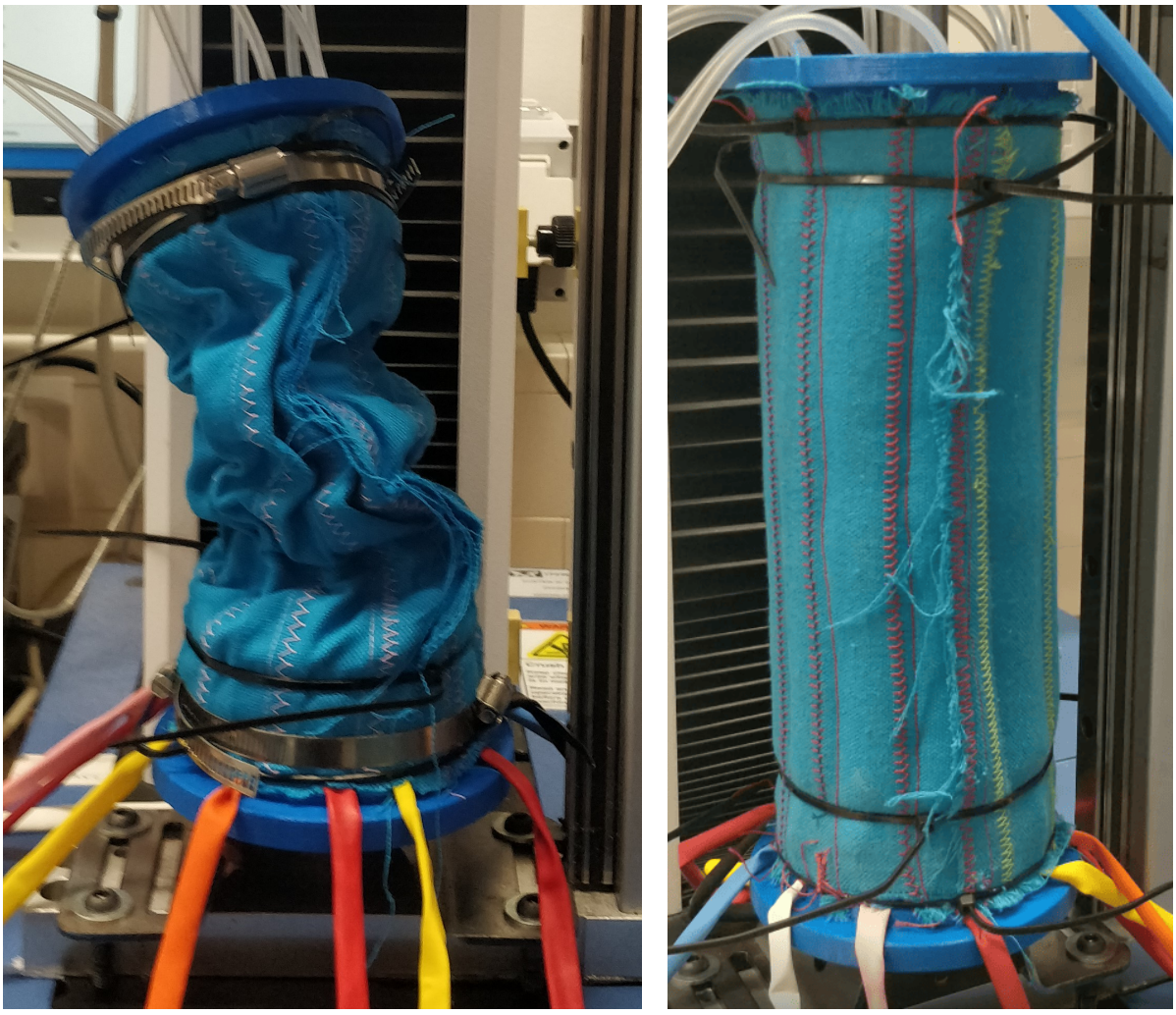

(a) Final prototype in the deflated state

(b) Final prototype in the inflated state

Figure 19: Final prototype for the hollow cylinder

3.5 Design of the solid cylinder

To be able to compare the achieved forces from the hollow cylinder design with the already existing solid pouch design, another prototype had to be created. This prototype was created with the same dimensions, to allow for a good comparison. The balloons however are not able to reach large enough strains to be used with the solid cylinder design. The earlier proposed condoms can be used to overcome this limitation, because they allow for large strains and their initial diameter is already larger as well. The condom nicely matches the shape of the cylinder and the problem with the high friction is not prevalent for the solid cylinder. This is due to the condom

reaching the maximum axial elongation before the radial expansion reaches the textile walls. To be able to attach the condom to the air supply tube, the lube was first removed such that the tape is able to stick to the condom. A rope is tied around the tube again, similar to the balloons used in the hollow cylinder design and then the tape is placed over the rope to secure it even further.
The solid cylinder also requires a top and bottom disk to close the top and bottom of the textile sleeve. The disks were chosen as the method to close the top and bottom, to have the design of the hollow and solid cylinder be as similar as possible. The disk required for the solid cylinder has the same dimensions as the hollow cylinder disks, however the standers are not needed because there is only a single large chamber. This results in the disks that can be seen in Figure 20, for the exact dimensions, other views and the corresponding Solidworks files, see Appendix A.2. Initially, both the hollow cylinder design as well as the solid cylinder design used zip ties to attach the disks to the textile sleeve. The zip ties however, were not strong enough to keep the textile sleeve attached to the disks for the higher pressures, especially the solid cylinder design. The connection between the textile sleeve and the disk slipped at lower pressures for the solid cylinder compared to the hollow cylinder. This has two causes, with the first one being the larger force exerted by the pressurized air in the solid cylinder design. The second reason being the reduced contact area, combined with the lower radial stiffness of the textile sleeve of the solid cylinder compared to the hollow one. The hollow cylinder textile sleeve has a higher radial stiffness, due to the connections between the inner and outer wall, requiring a larger force to cause the slippage between the disk and the textile sleeve. To improve the connection between the textile sleeve and the disk, a custom clamp was 3D printed. The custom clamps are a negative of the disks, with some small adjustments, such that the slits made for the zip ties are now used as insertion points for the clamps, which can be seen in Figure 21. For the exact dimensions, other views and the corresponding Solidworks files, see Appendix A.3. The clamps are secured together with bolts. The clamps offer a much stronger grip on the textile than the zip ties, due to the higher contact area and the ability to close them with a much larger force. If a similar amount of force was applied to close the zip ties, it would simply break the zip ties, which is why the customs clamps were needed.

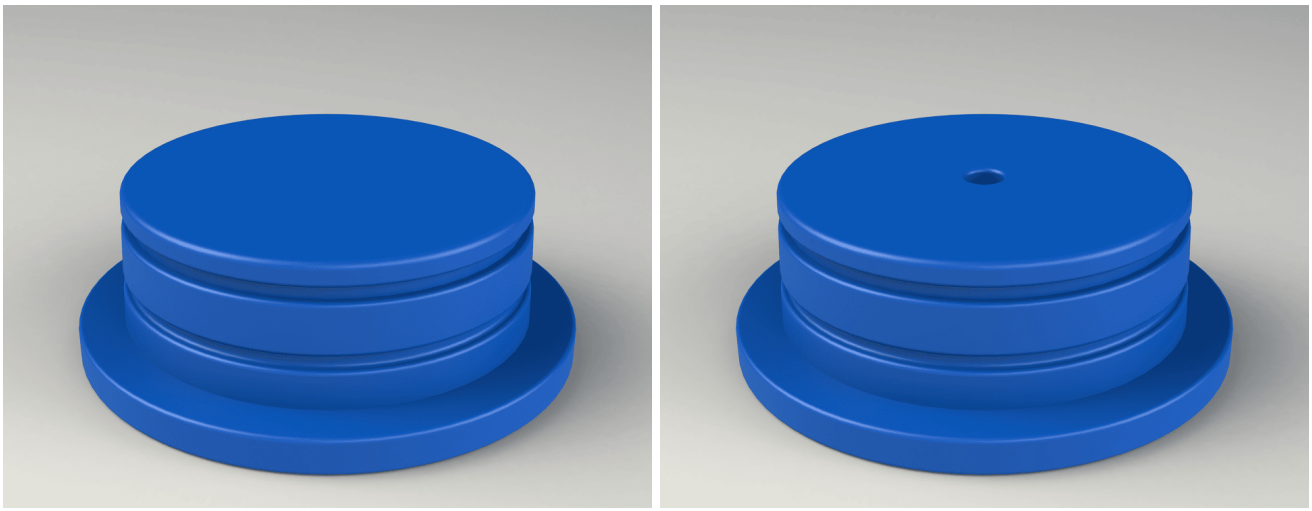

(a) Bottom disk

(b) Top disk, which has the air supply hole

Figure 20: Top and bottom closing disk for the solid cylinder

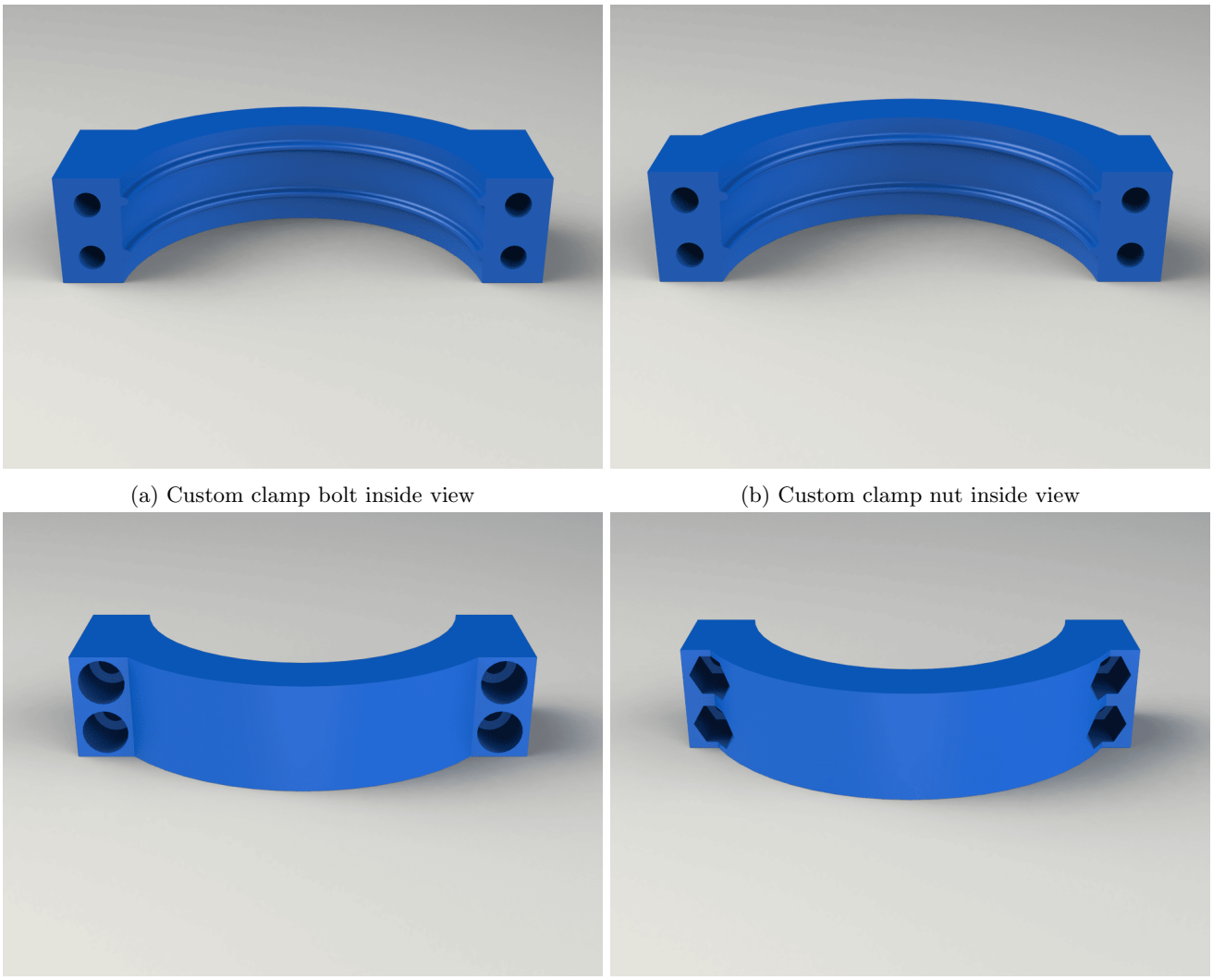

(a) Custom clamp bolt inside view

(b) Custom clamp nut inside view

(c) Custom clamp view from side with bolt head

(d) Custom clamp view from side with nut

Figure 21: Different views of the custom clamp for the solid cylinder

3.6 Test setup

To measure the force required to achieve buckling of the cylinder, a single column universal testing machine (UTM) is used, which was the INSTRON3343. In order to be able to test the cylinder, a custom setup had to be used inside the tester, of which a schematic overview can be seen in Figure 22. The custom setup consists of a linear slider on a rigid frame that is attached to the bottom plate of the UTM, which can be seen in Figure 23a. The slider in combination with the rigid frame is used to make sure that all the forces generated by the cylinders are only transferred to the UTM in the vertical direction, to make sure the load cell is not damaged by out of plane forces. A beam is attached to the slider, which in turn is attached to the load cell. The connection between the beam and the load cell is achieved using a coated metal wire. At the bottom of the beam, a small cylindrical piece of metal is attached using the same metal wire that is used to attach it to the load cell. This cylindrical piece of metal pushes down on the cylinder during the test, which can be seen in Figure 23b. At the bottom side of the UTM, a stander is attached over the rigid frame to have room for the air supply of the cylinder, which can be seen in Figure 23c. Double sided tape is attached to the top of the standers to increase the friction between prototype and the standers, to limit the movement of the bottom of the cylinder during the tests. The air supply during the tests was controlled by a pressurized air tank, Batavia volumia 7061061 portable Air Tank, for which the output pressure can be controlled using a knob.

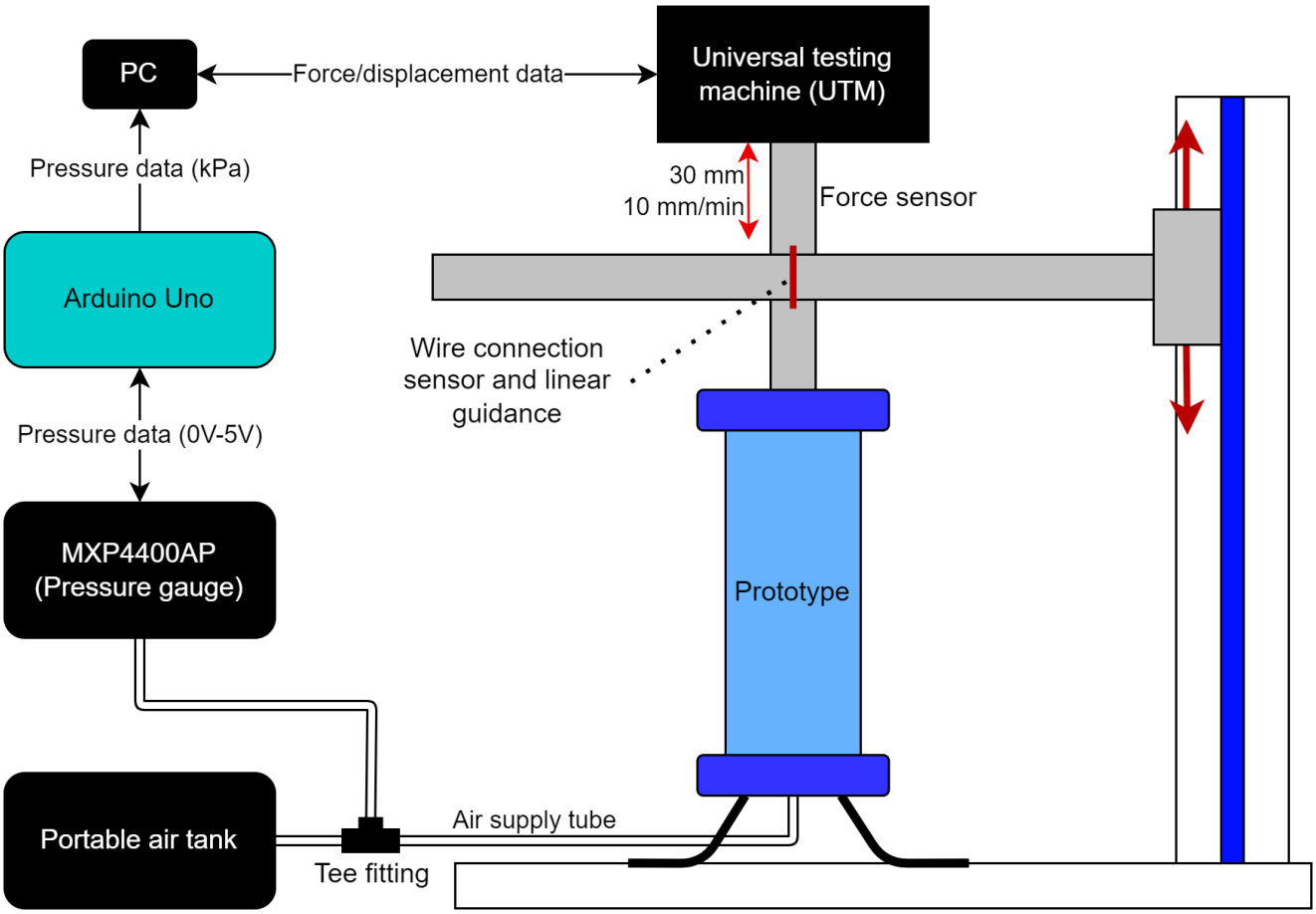

Figure 22: Schematic overview of the test setup for compression tests

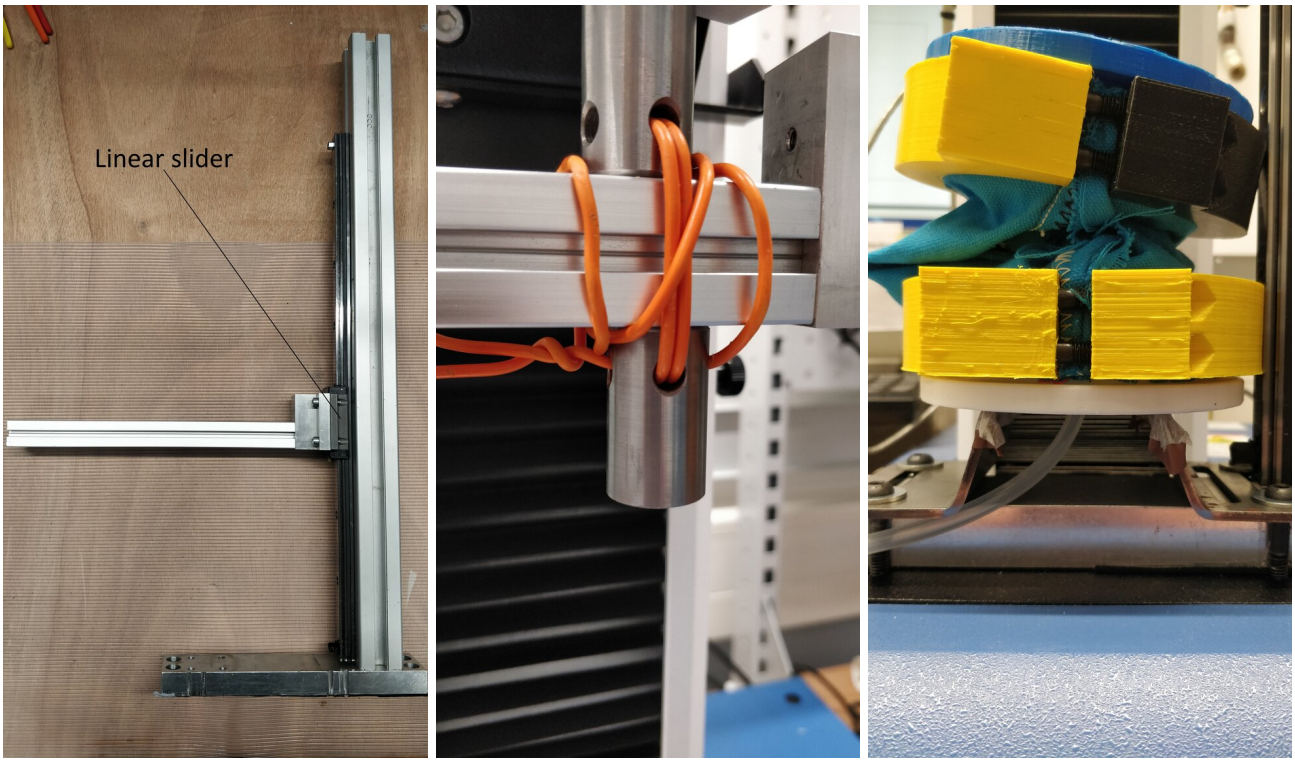

(a) Rigid frame with linear slider (b) Connection of load cell to slider bar and cylindrical metal pusher (c) Close-up view of risers in the test setup

Figure 23: Custom test setup in the UTM

3.6.1 Pressure gauge

The pressure is monitored using the MXP4400AP absolute pressure gauge. The pressure gauge has been calibrated using a digital pressure sensor. It was assumed that the ratio between the output voltage and the pressure was linear. This assumption seems to be correct since the digital pressure sensor readings match with the readings from the MPX4400AP over the entire working range of the MPX4400AP, which is between 0 kPa and 400 kPa. The equation to convert the analog value to the pressure is as follows:

$$P = \frac{P_{\max}(x - \delta)}{b}, \tag{30}$$

where x is the output voltage sent by the pressure gauge to the arduino uno, which converts the output voltage from the pressure gauge to a digital value. The offset between 0 kPa and the digital value output by the pressure gauge is δ, with a value of 239 for this specific sensor. The maximum pressure which the pressure gauge can measure is $P_{\max}$, which is used for scaling the digital value to a useful pressure reading. For further calibration of the pressure gauge the value of b has to be determined. The value for b is found by iteratively changing the value for b to have the output pressure match with the pressure reading from the digital pressure sensor. This is done for a few different known pressures, which gives a value of 994 for this specific pressure gauge.
The MPX4400AP absolute pressure gauge is used instead of the digital pressure sensor for a few reasons. The first reason is that the digital pressure sensor is relatively slow with changing the pressure reading to the actual pressure. However, the main reason for using the MPX4400AP in combination with the arduino uno is that this setup is attached to a computer which allows for easy processing of the data. The output from arduino uno can be saved to a text file allowing for easy creation of graphs and further processing of the data.

3.6.2 Test conditions

The force output of each of the cylinders was measured for a prescribed displacement of 30 mm downwards with a speed of 10 mm/min. The test was aborted either when the maximum displacement of 30 mm was achieved or the maximum force of 750 N was achieved. The maximum force limit was included in this test because the pressure gauge is rated up to 1000 N and a safety margin was used in order to not go over this limit. The last termination criterion for the test was when the prototype would buckle. This was observed manually and the test was ended

shortly after the buckling would occur. The buckling could be observed both visually on the specimen as well as in the results of the test. This test was repeated over a range of pressures from 25 kPa to 125 kPa, however the tests at 125 kPa did not produce any useful results, because both cylinders experienced rupture of the balloons during experiments at this pressure. During the test, the output force, displacement and pressure were monitored.
For each prototype three tests were done at each pressure. However, due to a rupture of the textile of the solid cylinder during the first test at 100 kPa the results were not sufficient. The prototype had to be recreated, which was done using the same process as before, but performing the tests at each pressure resulted in significantly different results than those obtained during the initial tests. The results from the newly created prototype were significantly higher than for the first prototype. With this in mind and the results of the hollow prototype being lower than expected, it was decided to also recreate this prototype to try and achieve better results, similar to the solid prototype. This results in a total of six pressure-displacement curves for each prototype design, along with their respective pressure measurements, except for the solid cylinder at 100 kPa, due to the failure of the first prototype.
Trying to achieve results for the solid cylinder at 125 kPa, resulted in another rupture of the textile of prototype. With this rupture again occurring at the the sewing line and the relative low effort of creating a new solid cylinder, it was decided to create a third prototype, however this time a different sewing pattern was used to close the textile sleeve. It was decided to redo the tests at 100 kPa, because initially the maximum force of 750 N was reached before buckling occurred using the second solid cylinder prototype. In the new tests it was decided to have a smaller safety margin of only 100 N for the force sensor, which means the maximum force is now 900 N. This results in there being six measurement results for each pressure for each prototype design. The third prototype iteration is also the one that is used for the actuation speed tests.

3.7 Actuation speed

The reduction of the volume of the actuator not only allows for a less powerful air supply, but also provides increased inflation and deflation speeds. The increased inflation and deflation speeds make the actuator more suitable for dynamic applications like fast-paced walking or even running. To support the claim of the increased inflation speeds an actuation speed test was performed. This consists of inflating each prototype to a predetermined pressure using a pressure supply at a given input pressure. The inflation is controlled using a valve system that can either be set to open or closed, by pressing a button. This valve system is attached to the same pressurized air tank as during the previous experiments. The output pressure knob of the pressurized air tank was set to 100 kPa, which results in the output pressure of this air tank to be slightly lower. This is probably due to a bad calibration of the pressure gauge on the portable air tank. The test starts with a fully deflated prototype, after which the the arduino uno with the connected pressure gauge is turned on. Next, the button is pressed and hold to open the valve, which starts to inflate the prototype and the test is continued until the pressure gauge has a reading of at least 85 kPa. This is done to make sure the pressure inside the prototype is well passed the threshold of 75 kPa, which is the pressure at which the time taken is observed. This test is performed three times for each prototype and is only done for the last produced version of each of the prototypes. It was decided to not perform the inflation test for the 100 kPa, due to previous failures of the prototypes at this pressure.

3.8 Bending test

A possible application of the produced actuators is to help with the extension of the knee. The extension of the knee would be supported by the actuator when it inflates, if it is attached to a point above and below the knee joint, similar to the setup which can be seen in Figure 24. To facilitate this movement, the compression strength of the prototypes is not of much interest. Instead the bending stiffness will determine the efficiency of the actuator. When the actuator is deflated the knee should not experience any influence from the soft actuator, but when the actuator is inflated it will become a solid cylinder, which will create a moment around the knee joint to help the leg extend. As described in Section 1 the specific force output of an actuator should be as high as possible. To determine, the possibly improved, output force of the proposed new design, a bending test is performed, for which a schematic overview of the test setup can be found in Figure 25. One side of the cylinder is clamped, while the other side is free and a prescribed transverse displacement is applied to the free end. The force resisting the bending movement of the prototype is the same force that will try to extend the knee in an actual application. The bending tests are performed on the same UTM as the other experiments. A different test setup had to be created in order to be able to clamp the prototypes and apply a force to the free end. To achieve this, an L-shaped frame was created from aluminum where on one side the prototype is clamped, while the bottom of the L-shaped frame was able to be attached to the UTM. The attachment of the L-shaped frame to the UTM was achieved by having a small metal plate, with four holes drilled into it, attached to the bottom side of the UTM using screws. This metal plate was placed over the bottom side of the L-shaped frame, locking it in place tightly and leaving no

significant movement. To be able to attach the prototypes to the L-shaped frame, a custom clamp method had to be created. This was done using two wooden plates which have a big hole in the center, with a diameter slightly larger than the prototypes, but smaller than the maximum radius from the closing disk, such that the prototype can pass through the hole, but the disks cannot. After first installment it was noticed that the wooden plates were not strong enough and flexed when closed. To overcome this problem, two small metal strips were cut, into which holes with the same radius were drilled as the four holes that were already in the wooden plates. Once installed the flex was eliminated and a tight clamp between the L-shaped frame, the wooden plates and the prototypes was achieved. The custom test setup can be seen in Figure 26.

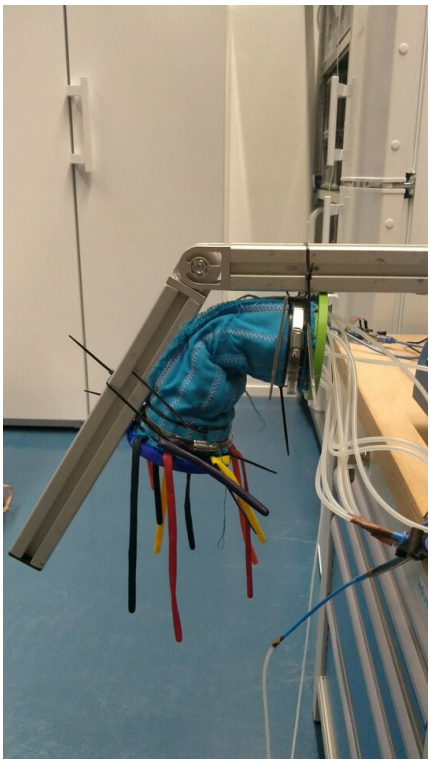

(a) Example of the actuator attached at a knee joint, in the bent state

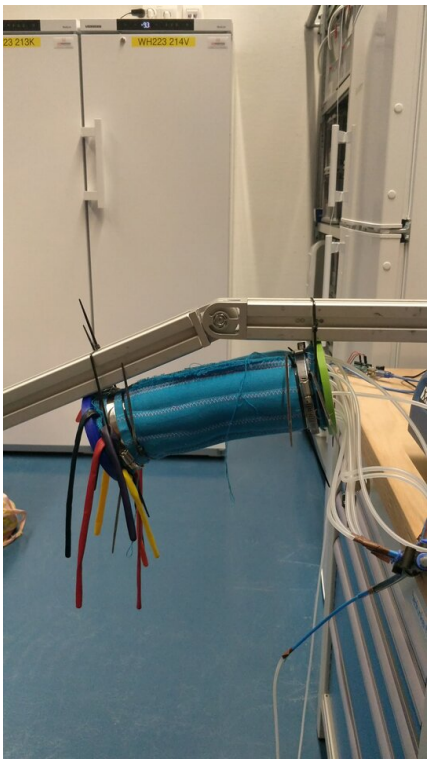

(b) Example of the actuator attached at a knee joint, in the extended state

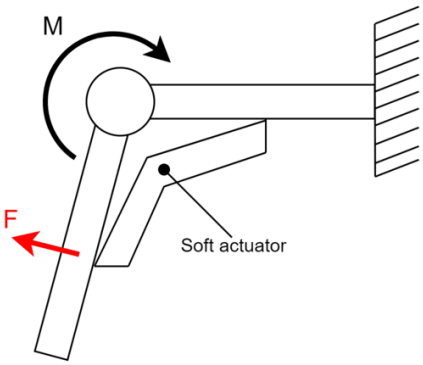

(c) Schematic overview of knee extension forces

Figure 24: Top and bottom closing disk for the solid cylinder

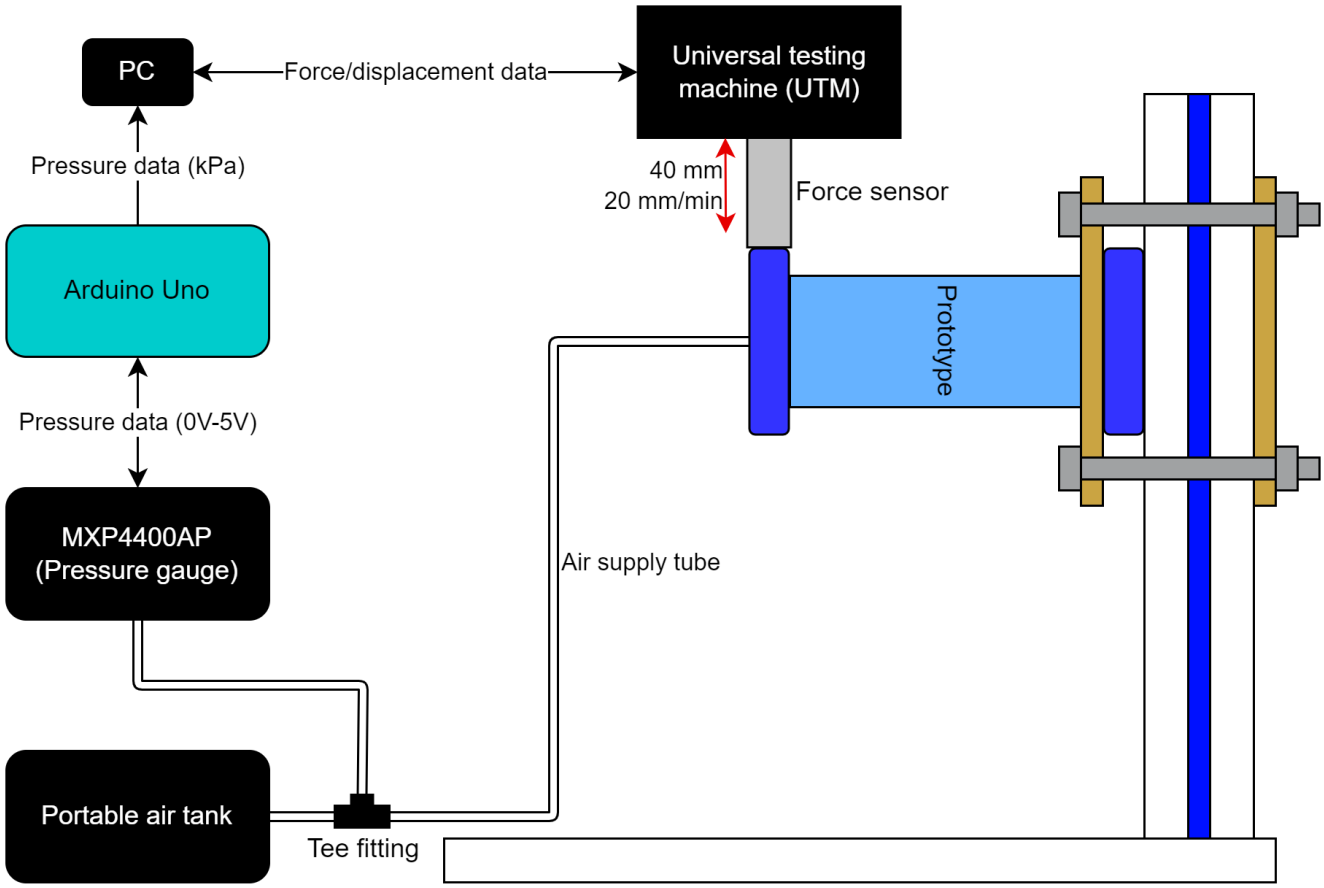

Figure 25: Schematic overview of the test setup for bending tests

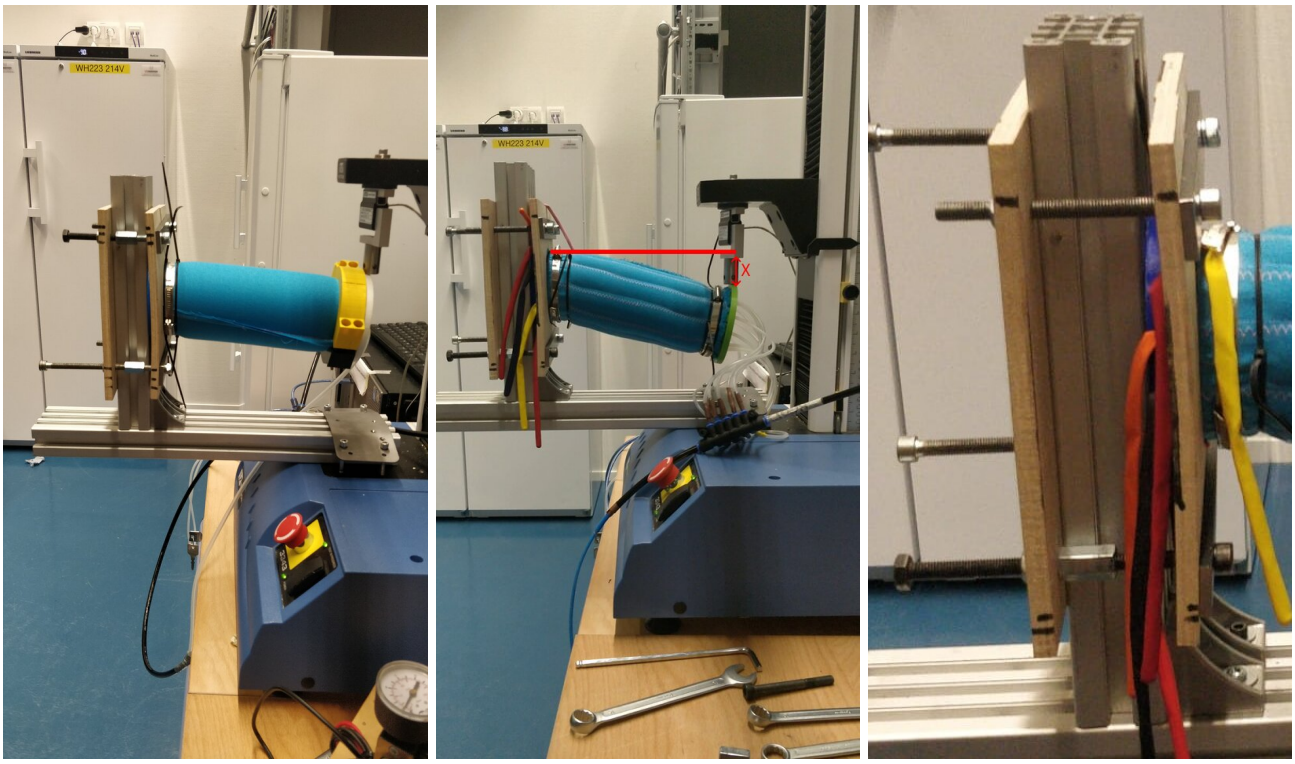

(a) Custom setup with the solid cylinder

(b) Custom setup with the hollow cylinder. The red line represents the starting position.

(c) Close-up view of clamp system

Figure 26: Custom test setup in the UTM

The prototypes were first clamped into the test setup, after which they were inflated to the desired pressure. Once the prototype was at the desired pressure the free end of the prototype was aligned with the moving head of the UTM to apply the force at the center of the free end of the prototype. The air was once again supplied by the pressurized air tank, Batavia volumia 7061061 portable Air Tank. The control of the air supply to the prototype was regulated using the same valve system used in the actuation speed tests, where the valve is opened when a button is pressed and it closes upon release of the button. Once the prototype is at the desired pressure and aligned with the UTM, the test was started together with the recording of the pressure. The pressure was collected using the same setup as in the previous tests, consisting of a computer, arduino uno and a pressure gauge. The bending test consisted of a prescribed downward displacement of 40 mm with a speed of 20 mm/min. The tests were terminated when the maximum displacement was achieved, the maximum force of 900 N was reached or when the change in measured force was higher than a certain safety threshold value. The tests were only terminated using the first criterion of reaching the maximum displacement since the forces measured where significantly lower than the threshold and the one failure of the hollow prototype did not result in a fast change in produced force. The experiments were performed for the same pressures as the compression tests, namely from 25 kPa up to and including 100 kPa with 25 kPa intervals. The bending tests were only performed on one iteration of the prototypes, which is a new iteration for the solid cylinder, while the hollow cylinder used the same iteration of the prototype as the second iteration in the compression tests. A new iteration of the solid cylinder prototype was used for the bending tests, due to a failure of the previous iteration, where the textile sleeved ripped. During the tests, the pressure, displacement and the force are recorded, which are used for post-processing in the results.

4 Results

4.1 Theoretical results

The reference dimensions were the same for all produced prototypes to allow for a fair comparison. The reference outer diameter is 9 cm, while the height is 18 cm. The air consumed can be approximated by using using the diameter, length and for the hollow cylinder also the inner diameter, which is 5 cm. Using the formulas given in section 2.1, some calculations can be done to compare the theoretical improvement of the changed design, with respect to the original design. The values found from the theoretical calculations involve simplifications to allow for calculation by hand and will be compared with the results from the tests performed on the produced prototypes. It should be noted that the material properties are unknown for the produced prototype, but an attempt has been made to measure the properties of the strain limiting layer.

4.1.1 Compression

A force balance can be created between the applied force and the pressure inside the cylinder, similar to how it was described in section 2.1 in equation 12 and 13. To find the initial volume and the volume at a secondary point, the area of the cylinder and the length at that point can be used. For the manual calculations it is assumed that the area does not change with displacement. This assumptions will most likely create small deviations from the actual results, since the cylinder diameter will change slightly with displacement. The area for the solid cylinder is 63.6 cm^2 while the area of the hollow cylinder is 44.0 cm^2. Multiplying the area with the length of the cylinder results in a volume of 1145.1 cm^3 and 791.7 cm^3, for the solid and hollow cylinder, respectively. With the assumption that the displacement during the tests is the same, a volume ratio of 69.1 % is found. Equation 12 and 13 can be rewritten into a single equation,

$$F = \frac{P_1 V_1}{V_2} A. \tag{31}$$

The ratio of $\frac{V_1}{V_2}$ will always be the same for both cylinder designs, given the assumption that the cross-sectional area is not a function of displacement and that the prototypes have the same length. With the assumption that the initial pressure is the same for both cylinders, it follows that the applied force is only a function of the cross-sectional area. This would mean that the ratio of the forces is the same as the ratio of the cross-sectional areas. The ratio between the cross-sectional areas is 69.1 %, regardless of the initial pressure and length, as long as they are the same for both designs and the walls are still significantly thick, as to not have wall buckling involved in solution of the problem. If the behaviour of the cylinders is dominated by compression, there is no improvement gained from the change in the geometry. This simplification does not include the strength of the different air bladders and the textile sleeve, but these are significantly small compared to other forces. If the produced output force per volume air consumed is the same for both designs, the best design would be the solid cylinder, due to the reduced time required to produce the prototype as well as the lower amounts of materials used and the lower stiffness in the deflated state. Furthermore, the footprint of the solid cylinder design would be smaller as well for a given output force.

4.1.2 Buckling

If the behaviour would be dominated by the buckling strength instead of the compression behaviour, the effective strength would change. The behaviour starts to be dominated by buckling when the slenderness ratio is larger than a certain threshold value and is dominated by compression below a certain other threshold value. Between those two values, the behaviour is a combination of the two failure modes. The transition from compression to buckling behaviour is a gradual one, with no exact value for the slenderness ratio at which this occurs. These values are also dependant on the material properties. If it is assumed that the behaviour is dominated by the buckling strength, an analysis can be made to show the improvement of the new design with respect to the old design. This can be done according to equation 6, where it is once again assumed that the material properties are the same between the two different designs. This assumption reduces the equation such that the difference between the two designs is caused only by the second moment of area. Using equations 6-8 gives,

$$
\begin{aligned}
r_{\text{in}} &= \frac{2.5}{4.5} r_{\text{out}} = 0.55 r_{\text{out}} \\
I_1 &= \frac{\pi 4.5^4 (1 - 0^4)}{4} = \frac{\pi 4.5^4 (1)}{4} \\
I_2 &= \frac{\pi 4.5^4 (1 - 0.55^4)}{4} = \frac{\pi 4.5^4 (0.90)}{4} \\
\frac{F_2}{F_1} &= \frac{I_2}{I_1} = 0.90.
\end{aligned}
\tag{32}
$$

With the hollow cylinder only consuming the earlier mentioned 69.1 % of the air and in theory being able to achieve a force 90 % of that of the solid cylinder, it follows that it should have an effective strength of,

$$
F_{\text{eff}} = \frac{0.90}{0.691} = 1.31, \tag{33}
$$

where F_{eff} is the effective strength of the hollow cylinder with respect to the solid cylinder per unit air consumed. The effective strength ratio is further increased as the inner radius of the produced prototype increases. It should be noted that if the inner radius becomes too big other effects like wall buckling will become dominant, which might result in a significant reduction in effective strength. Furthermore, this equation is valid for normal materials and not necessarily correct for an inflatable membrane structure like the used prototypes.

4.1.3 Bending Timoshenko beam equation

A similar analysis has been performed for the bending stiffness of the prototypes. The bending of the beam can be approximated according to Timonshenko's beam theory given in equation 15. In the section 2.1 it was shown how this equation can be rewritten, when assuming that the material properties and boundary conditions are the same for both prototypes, resulting in equation 27. With the knowledge that the deflection is dominated by the second term of this equation, the optimization problem will be dominated by the second moment of area. With the problem depending only on the second moment of area, similar to the equation for buckling, the same conclusion can be drawn that the effective strength will be about 1.3 times as high. The actual effective strength will be slightly lower, due to the decrease in area, which results in a slightly larger displacement. Furthermore, the value for κ will decrease as well for a prototype with thinner walls. For this specific prototype the value for m is $\frac{2.5}{4.5}$, which leads to a value of κ of,

$$
\begin{aligned}
\kappa_{\text{h}} &= \frac{6 \left({\frac{2.5}{4.5}}^2 + 1 \right)^2 (v+1)^2}{v \left(12 \cdot {\frac{2.5}{4.5}}^4 + 48 \cdot {\frac{2.5}{4.5}}^2 + 12 \right) + 37 \cdot {\frac{2.5}{4.5}}^2 + 7 \cdot {\frac{2.5}{4.5}}^4 + v^2 \left(4 \cdot {\frac{2.5}{4.5}}^4 + 16 \cdot {\frac{2.5}{4.5}}^2 + 4 \right) + 7} \\
&= \frac{22472 \, (v+1)^2}{2187 \left(\frac{61144 \, v^2}{6561} + \frac{61144 \, v}{2187} + \frac{125227}{6561} \right)}.
\end{aligned}
\tag{34}
$$

The value of κ for the solid cylinder prototype is found when $m = 0$ is substituted into equation 18, leading to,

$$
\kappa_{\text{s}} = \frac{6 \left(0^2 + 1 \right)^2 (v+1)^2}{v \left(12 \cdot 0^4 + 48 \cdot 0^2 + 12 \right) + 37 \cdot 0^2 + 7 \cdot 0^4 + v^2 \left(4 \cdot 0^4 + 16 \cdot 0^2 + 4 \right) + 7} = \frac{6 \, (v+1)^2}{4 \, v^2 + 12 \, v + 7}. \tag{35}
$$

A general formula can be derived to describe the maximum displacement for both the Timoshenko beam equation and the inflatable beam model, allowing for an investigation of the differences between the different models. The general formula for the maximum displacement using the Timoshenko beam equations is,

$$
w_{\text{h}} = -\frac{4 \, L^3 \, P}{3 \, E \, {r_{\text{out}}}^4 \, \pi \, (1 - m^4)} - \frac{L \, P \, \left(v \, \left(12 \, m^4 + 48 \, m^2 + 12 \right) + 37 \, m^2 + 7 \, m^4 + v^2 \, \left(4 \, m^4 + 16 \, m^2 + 4 \right) + 7 \right)}{6 \, G \, {r_{\text{out}}}^2 \, \pi \, \left(1 - m^2 \right) \left(m^2 + 1 \right)^2 (v+1)^2}. \tag{36}
$$

Dividing this equation, by the same equation, but with $m = 0$ substituted in, gives the relative strength of the hollow cylinder with respect to the solid cylinder,

$$
\begin{aligned}
\frac{w_{\mathrm{s}}}{w_{\mathrm{h}}} &= \frac{\frac{4\,L^3\,P}{3\,E\,{r_{\mathrm{out}}}^4\,\pi} + \frac{L\,P\left(4\,v^2+12\,v+7\right)}{6\,G\,{r_{\mathrm{out}}}^2\,\pi\,(v+1)^2}}{\frac{4\,L^3\,P}{3\,E\,{r_{\mathrm{out}}}^4\,\pi\,(1-m^4)} + \frac{L\,P\,(v\,(12\,m^4+48\,m^2+12)+37\,m^2+7\,m^4+v^2\,(4\,m^4+16\,m^2+4)+7)}{6\,G\,{r_{\mathrm{out}}}^2\,\pi\,(1-m^2)\,(m^2+1)^2\,(v+1)^2}} \\
&= \frac{\left(m^2+1\right)^2\left(1-m^4\right)\left(1-m^2\right)\left(8L^2G\left(\nu+1\right)^2+Er_{\mathrm{out}}^2\left(4\nu^2+12\nu+7\right)\right)}{8L^2G\left(\nu+1\right)^2\left(m^2+1\right)^2\left(1-m^2\right)+Er_{\mathrm{out}}^2C\left(1-m^4\right)} \\
&= \frac{\left(1-m^2\right)\left(m^2+1\right)^2\left(8L^2G\left(\nu+1\right)^2+Er_{\mathrm{out}}^2\left(4\nu^2+12\nu+7\right)\right)}{8L^2G\left(\nu+1\right)^2\left(m^2+1\right)+Er_{\mathrm{out}}^2C} \\
C &= \nu\left(12m^4+48m^2+12\right)+37m^2+7m^4+\nu^2\left(4m^4+16m^2+4\right)+7
\end{aligned}
\tag{37}
$$

The equation above gives the relative strength of the hollow cylinder with respect to the solid cylinder, however, a more interesting measurement would be the relative strength per unit air consumed. To arrive at the relative strength per unit air consumed, the equation above has to be divided by the ratio of air consumed between the solid and hollow cylinder,

$$
\frac{V_{\mathrm{h}}}{V_{\mathrm{s}}} = \frac{A_{\mathrm{h}}}{A_{\mathrm{s}}} = 1-m^2, \tag{38}
$$

where the assumption is made that both cylinders have the same length and the radius is constant along the length. Combining equations 37 and 38 gives,

$$
\begin{aligned}
F_{\mathrm{eff}} &= \frac{\left(m^2+1\right)^2\left(1-m^4\right)\left(8L^2G\left(\nu+1\right)^2+Er_{\mathrm{out}}^2\left(4\nu^2+12\nu+7\right)\right)}{8L^2G\left(\nu+1\right)^2\left(m^2+1\right)^2\left(1-m^2\right)+Er_{\mathrm{out}}^2C\left(1-m^4\right)} \\
C &= \nu\left(12m^4+48m^2+12\right)+37m^2+7m^4+\nu^2\left(4m^4+16m^2+4\right)+7
\end{aligned}
\tag{39}
$$

This equation can be rewritten to be a function of $\frac{G}{E}$ instead, by dividing both numerator and denominator by E, resulting in,

$$
\begin{aligned}
F_{\mathrm{eff}} &= \frac{\left(m^2+1\right)^2\left(1-m^4\right)\left(8L^2\frac{G}{E}\left(\nu+1\right)^2+r_{\mathrm{out}}^2\left(4\nu^2+12\nu+7\right)\right)}{8L^2\frac{G}{E}\left(\nu+1\right)^2\left(m^2+1\right)^2\left(1-m^2\right)+r_{\mathrm{out}}^2C\left(1-m^4\right)} \\
C &= \nu\left(12m^4+48m^2+12\right)+37m^2+7m^4+\nu^2\left(4m^4+16m^2+4\right)+7
\end{aligned}
\tag{40}
$$

This equation can be visualized in a 3D surface plot as a function of $\frac{G}{E}$ and m. From this plot the influence of these variables on the effective strength can be seen and the optimal inner radius can be determined for a given value of $\frac{G}{E}$. An example plot is created and can be seen in figure 27, where $\nu = 0.3$, $r_{\mathrm{out}} = 4.5\,\mathrm{cm}$, $L = 18\,\mathrm{cm}$ has been used for this specific plot. From this plot it can be observed that any decrease in inner wall radius would result in a decrease in the relative strength. In figure 27b it can be seen however, that for very low values of $\frac{G}{E}$ the optimal design would be the solid cylinder rather than a hollow cylinder.
Changing any of the parameters results in a very similar plot, but the data is shifted. Changing the value of r_{out}, to a larger value, the breakpoint of where an increase in inner radius results in a decrease in the effective strength moves to the right and is thus also reducing the effective strength at higher ratio's of $\frac{G}{E}$. Similarly it can be shown that for an increase in L the breakpoint moves to the left and has an opposite effect of an increase in r_{out}. Even more specific, if the ratio $\frac{r_{\mathrm{out}}}{L}$ stays constant, the solution stays the same as well. This also means that the equation can be further reduced by dividing by L^2, to be dependent on one less variable as follows,

$$
\begin{aligned}
F_{\mathrm{eff}} &= \frac{\left(m^2+1\right)^2\left(1-m^4\right)\left(8\frac{G}{E}\left(\nu+1\right)^2+C_2^2\left(4\nu^2+12\nu+7\right)\right)}{8\frac{G}{E}\left(\nu+1\right)^2\left(m^2+1\right)^2\left(1-m^2\right)+C_2^2C\left(1-m^4\right)} \\
C &= \nu\left(12m^4+48m^2+12\right)+37m^2+7m^4+\nu^2\left(4m^4+16m^2+4\right)+7 \\
C_2 &= \frac{r_{\mathrm{out}}}{L}.
\end{aligned}
\tag{41}
$$

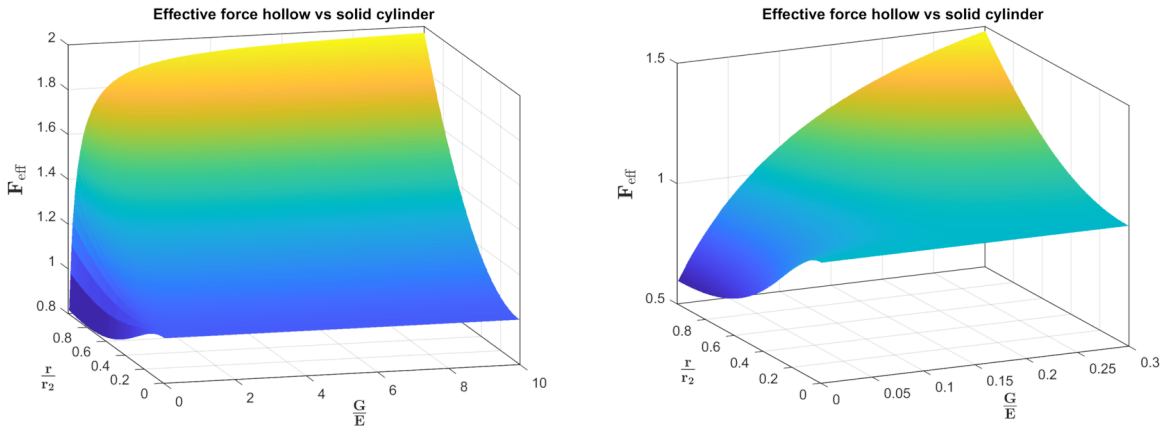

(a) Large range for $\frac{G}{E}$

(b) Zoomed in view of region of interest

Figure 27: 3D surface plots of the theoretic effective strength ratio between the hollow and solid cylinder per unit air consumed as a function of m and $\frac{G}{E}$.

The last variable that can be changed is ν, which should be in the range $[0, 0.5]$ for the materials considered here. Using a lower value for ν results in a slightly higher effective force. For isotropic materials the Poisson ratio ν, Young's modulus E and the shear modulus G are related according to,

$$G = \frac{E}{2\,(1+\nu)}. \tag{42}$$

The influence of the different possible values for the Poisson ratio can be determined by plotting effective strength as a function of the inner diameter ratio and the Poisson ratio, while keep the ratio for $\frac{G}{E}$ constant, which can be seen in figure 28. From this graph it can easily be observed that having the lowest possible value for the Poisson ratio results in the highest effective strength. The value for the Poisson ratio is material dependent and is thus not easily changed.

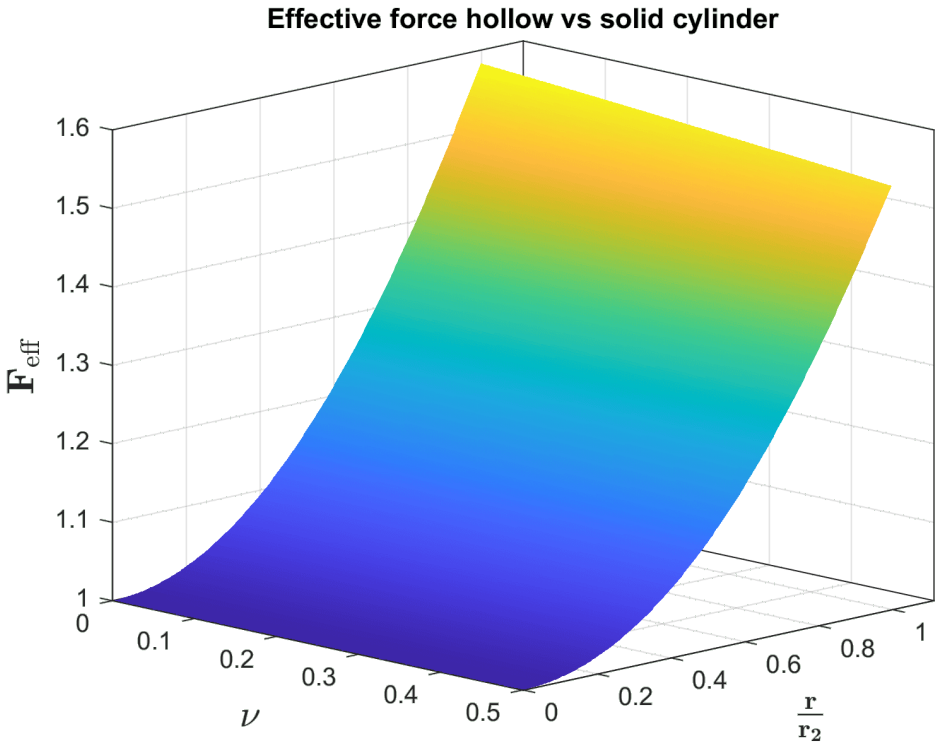

Figure 28: 3D surface plot of the theoretic effective strength ratio between the hollow and solid cylinder per unit air consumed as a function of ν and m.

4.1.4 Bending inflatable beam equation

A very similar approach as for the Timoshenko beam equation can be applied to equation 28. It does have to be noted that the formula has changed with respect to the Timoshenko beam equation, which used the variable A in the location of what is now variable S. The new definition for this variable is the cross-sectional area of only the strain limiting material and no longer the cross-sectional area of the inflated part, which will have a significant influence on the found values. The same change has been made for the second moment of area, I.
A few simplifications will have to be introduced. The shear coefficient is no longer substituted into the formula but is represented by κ and κ_2 for the solid and hollow cylinder respectively. Equation 18 is still applicable. Furthermore, m will no longer be used, but instead r and r_2 will be used, which are the outer and inner radius respectively. Another variable introduced is h, which represents the wall thickness. It is assumed to be identical for the inner and outer walls. Using m would also require the introduction of m_2 and possibly m_3 to account for sections to be calculated, which would just complicate the equation further. A quick overview of the variables to be substituted into equation 28 is given below.

$$
\begin{aligned}
\kappa &= \frac{6\,(v+1)^2}{4\,v^2+12\,v+7}\\
\kappa_2 &= \frac{6\left(\left(\frac{r_2}{r}\right)^2+1\right)^2(v+1)^2}{v\left(12\left(\frac{r_2}{r}\right)^4+48\left(\frac{r_2}{r}\right)^2+12\right)+37\left(\frac{r_2}{r}\right)^2r^2+7\left(\frac{r_2}{r}\right)^4+v^2\left(4\left(\frac{r_2}{r}\right)^4+16\left(\frac{r_2}{r}\right)^2+4\right)+7}\\
A_s &= \pi r^2\\
A_h &= \pi\left(r^2-r_2^2\right)\\
S_s &= \frac{\pi\left(r^2-(r-h)^2\right)}{2}\\
S_h &= A_s+\frac{\pi\left(r_2^2-(r_2-h)^2\right)}{4}\\
I_s &= \frac{\pi\left(r^4-(r-h)^4\right)}{4}\\
I_h &= I_s+\frac{\pi\left(r_2^4-(r_2-h)^4\right)}{4}\\
F_p &= pA,
\end{aligned}
\tag{43}
$$

where p is the pressure. By examining at the equations given above in combination with equation 28, several observations can be made about the ratio between the hollow and the solid cylinder design. Since the values for S and I are always larger for the hollow cylinder, it can be observed from equation 28 that when the values for the shear and Young's modulus are significantly larger than the internal pressure, the hollow cylinder will outperform the solid cylinder and vice versa. When the values for the Young's and shear modulus are significantly larger it is possible that the hollow cylinder will outperform the solid cylinder without the volume normalization.
The first step in comparing the two different designs based on the inflatable beam model is to divide the displacement of the solid cylinder by the displacement of the hollow cylinder, resulting in the following expression:

$$
\frac{w_s}{w_h}=\frac{\frac{L\,P}{G\,\kappa\,\pi\left(r^2-(h-r)^2\right)+\pi\,p\,r^2}+\frac{4\,L^3\,P}{\pi\left(r^4-(h-r)^4\right)\left(3\,E+\frac{3\,p\,r^2}{r^2-(h-r)^2}\right)}}{\frac{L\,P}{G\,\kappa_2\left(\pi\left(r^2-(h-r)^2\right)+\pi\left(r_2^2-(h-r_2)^2\right)\right)+\pi\,p\left(r^2-r_2^2\right)}+\frac{4L^3\,P}{\left(3\,E+\frac{3\,\pi\,p\left(r^2-r_2^2\right)}{\pi\left(r^2-(h-r)^2\right)+\pi\left(r_2^2-(h-r_2)^2\right)}\right)\left(\pi\left(r^4-(h-r)^4\right)+\pi\left(r_2^4-(h-r_2)^4\right)\right)}}
\tag{44}
$$

This equation can be simplified by removing $\frac{LP}{\pi}$, since this term appears in each of the components, which result in,

$$
\frac{w_s}{w_h}=\frac{\frac{1}{G\,\kappa\left(r^2-(h-r)^2\right)+p\,r^2}+\frac{4\,L^2}{3\left(r^4-(h-r)^4\right)\left(E+\frac{p\,r^2}{r^2-(h-r)^2}\right)}}{\frac{1}{G\,\kappa_2\left(r^2-(h-r)^2+r_2^2-(h-r_2)^2\right)+p\left(r^2-r_2^2\right)}+\frac{4L^2}{3\left(r^4-(h-r)^4+r_2^4-(h-r_2)^4\right)\left(E+\frac{p\left(r^2-r_2^2\right)}{r^2-(h-r)^2+r_2^2-(h-r_2)^2}\right)}}
\tag{45}
$$

$$\frac{w_s}{w_h} = \frac{\frac{1}{G\,\kappa,(2hr-h^2)+p\,r^2} + \frac{4\,L^2}{3\left(r^4-(h-r)^4\right)\left(E+\frac{p\,r^2}{2hr-h^2}\right)}}{\frac{1}{G\,\kappa_2\,(2hr-2h^2+2hr_2)+p\left(r^2-r_2^2\right)} + \frac{4L^2}{3\left(r^4-(h-r)^4+r_2^4-(h-r_2)^4\right)\left(E+\frac{p\left(r^2-r_2^2\right)}{2hr-2h^2+2hr_2}\right)}} \tag{46}$$

This formula represents the ratio between the displacement of the two different designs. This is however not a good measure of the performance of the two different designs with respect to each-other. For a more fair comparison the ratio will be divided by the ratio of volume consumed, which equals,

$$\frac{V_h}{V_s} = \frac{r^2}{r^2 - r_2^2}. \tag{47}$$

Dividing equation 46 by the volume ratio given above results in,

$$F_{\text{eff}} = \frac{\frac{r^2}{G\,\kappa\,(2hr-h^2)+p\,r^2} + \frac{4\,L^2\,r^2}{3\left(r^4-(h-r)^4\right)\left(E+\frac{p\,r^2}{2hr-h^2}\right)}}{\frac{r^2-r_2^2}{G\,\kappa_2\,(2hr-2h^2+2hr_2)+p\left(r^2-r_2^2\right)} + \frac{4L^2\left(r^2-r_2^2\right)}{3\left(r^4-(h-r)^4+r_2^4-(h-r_2)^4\right)\left(E+\frac{p\left(r^2-r_2^2\right)}{2hr-2h^2+2hr_2}\right)}}. \tag{48}$$

This equation differs quite significantly from the relation achieved in equation 41. This is mostly caused by the fact that in equation 41 the cross-section is taking as a solid, whereas for equation 48 the cross-section is taken as a thin walled structure, which is a more realistic approach for the prototypes created. The ratio per unit volume obtained for the inflatable model, however, is significantly more complex compared to the one derived using the Timoshenko beam equation. This increased complexity makes it more challenging to make direct observations from the formula. Something that can be derived from this formula directly is that an increase in the pressure will always result in a reduction of the relative strength of the hollow cylinder with respect to the solid cylinder. This is caused by the fact that pressure in the numerator terms is multiplied by r^2, while the pressure in the denominator term is multiplied by $r^2 - r_2^2$, which is always smaller than the term in the numerator.
Furthermore, a similar but opposite observation can be made about the shear modulus. An increase in the shear modulus will result in an increase in the effective strength of the hollow cylinder with respect to the solid cylinder. This is caused by the fact that,

$$\frac{2hr - h^2}{2hr - 2h^2 + 2hr_2} > 1 \tag{49}$$

is never true for the values that can be used for h, r and r_2, which are always positive, where $r > r_2 > h$. Furthermore, it can be shown that for the same range of the variables that,

$$\frac{r^4 - (h-r)^4}{r^4 - (h-r)^4 + r^2 - (h-r_2)^4} > 1 \tag{50}$$

is never true either, which means that an increase in the Young's modulus will always result in an increase in the effective strength of the hollow cylinder with respect to the solid cylinder. This is caused by the fact that the hollow cylinder has a larger cross-sectional area for which these variables work, while having a lower cross-sectional area which is filled with air.
In the Timoshenko beam theory the ratio per unit volume remained constant as long as the ratio between $\frac{L}{r}$ stayed constant. This is no longer the case, albeit that the changes in the effective strength ratio are not very significantly when the length, the inner and outer radius are all changed with the same factor.
Similarly, it should be noted that the previously found relationship between the shear modulus and Young's modulus $\frac{G}{E}$ is no longer valid. Keeping the ratio between these two variables constant, no longer means that the effective strength per unit volume stays constant. This is caused by the added pressure dependent terms in the denominator of equation 28. The reference values given in table 2 are used to perform a similar analysis as the one performed for the Timoshenko beam model. These are measured values based on the reference geometrical design, with the exception of the Poisson ratio and shear modulus. The shear modulus corresponds to an isotropic material, which is not necessarily the case for the materials used, but measuring the actual value for this variable was very difficult. The influence of a variable on the effective strength ratio per unit volume will become clear when all the other variables are kept constant while this variable changes value.

Table 2: Reference values used for graphs below and optimal values to maximize cylinder strength

Variable	Reference value	Maximize strength
ν	0.3	0.0
r	0.045 m	∞
r_2	0.025 m	-
h	0.0005 m	∞
L	0.18 m	0
p	100 kPa	∞
G	$\frac{E}{2(1+\nu)}$	∞
E	2.2 MPa	∞

Keeping all the variables constant, but changing the value ν, results in a graph with similar conclusion as for the Timoshenko beam model. However, the outperformance of the hollow cylinder with respect to the solid cylinder is a lot larger for this model. The graph can be seen in figure 29. The optimal geometry and value for ν are achieved when $\nu = 0$, while the optimal value for m corresponding to this is 1, which represents a hollow cylinder with an infinitesimally thin wall. The shape of this graph is also dependent on the ratio between the other variables, but the conclusion with respect to ν remains the same where an increase in ν responds to a decrease in the relative performance of the hollow cylinder with respect to the solid cylinder. This is in line with the expectation made above for the shear modulus. The shear modulus introduces ν into the equation with an inverse relation between ν and the shear modulus. An increase in the shear modulus results in an increase in the effective strength ratio, while a decrease in ν will achieve the the same. This is true while using the reference values, however, if different values are used, the optimal value for $\frac{r_2}{r}$ can shift. More specifically if the effective strength per unit volume of the hollow cylinder is lower than that of the solid cylinder for all values of $\frac{r_2}{r} \neq 0$, than the value of ν does not matter. This would result in the optimal geometry being the solid cylinder, which would mean that the ratio is always 1 since both designs would be the same.

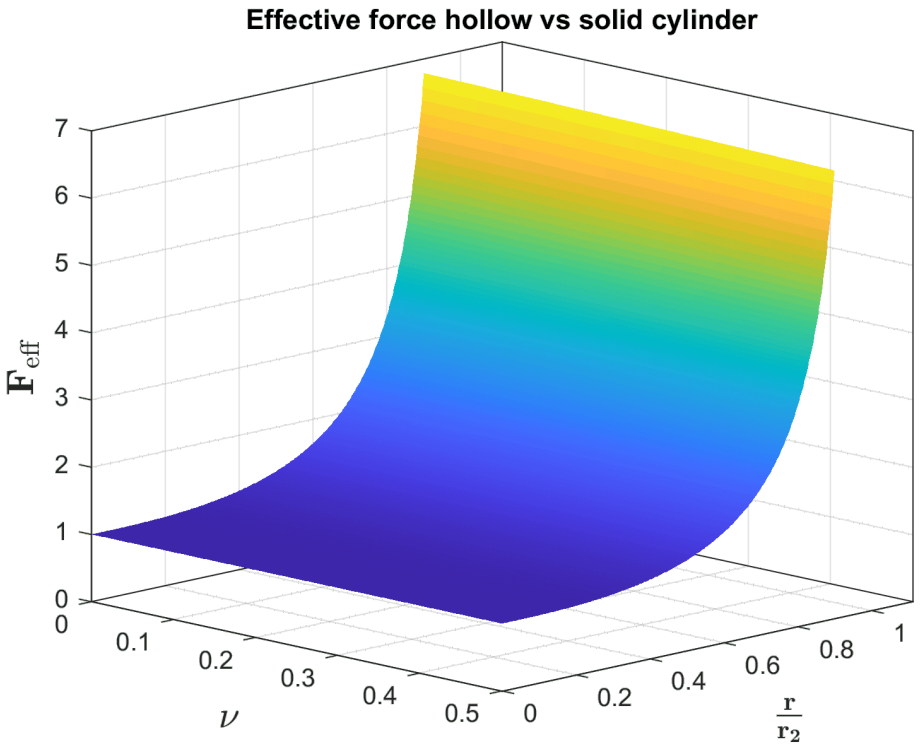

Figure 29: 3D surface plot of the theoretic effective strength ratio between the hollow and solid cylinder per unit air consumed as a function of ν and $\frac{r}{r_2}$.

Using the reference value for ν while having p be variable results in an interesting optimization problem. When the pressure is small relative to the values of the Young's and shear modulus, results in the optimal shape being the hollow cylinder, which can be seen in figure 30a. As the pressure increases and gets closer to the same order of magnitude as the Young's and shear modulus, moving towards a hollow cylinder does not always result in an increase in the effective strength, which can be seen in figure 30b. This means that to optimize the design, increasing the hollowness of the cylinder is not always beneficial. However, after decreasing the inner volume enough the hollow cylinder starts to outperform the solid cylinder again. As the pressure increases even further and becomes larger than the Young's and shear modulus, the optimal shape becomes the solid cylinder. This does not mean that an increase in the pressure will result in a lower strength of the design, just that relative strength between the hollow and solid cylinder design changes. Furthermore, having the internal pressure higher than the Young's modulus of the material is not realistic as this would result in a rupture of the material. In conclusion, for pressures that are realistically possible, the optimal design would be to have the cylinder as hollow as possible, but as the pressure starts to approach the same order of magnitude as the Young's modulus and shear modulus, having a solid cylinder might be beneficial compared to a hollow cylinder.

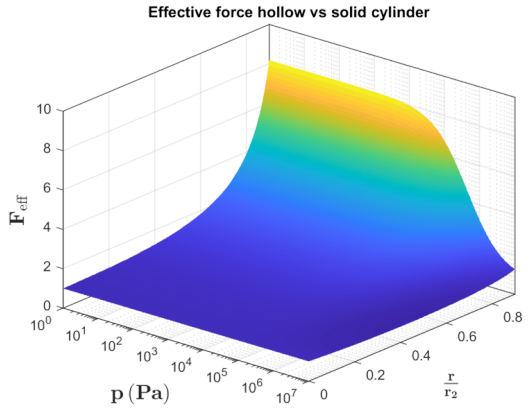

(a) Low internal pressure relative to Young's modulus and shear modulus

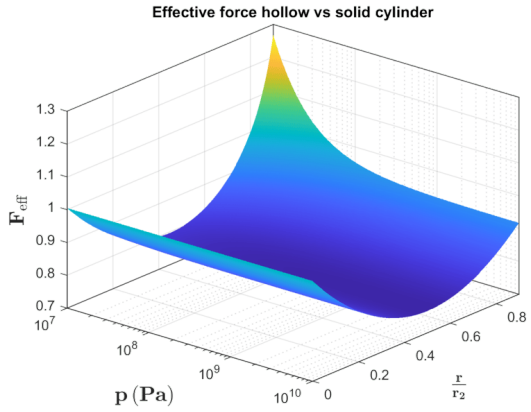

(b) High internal pressure relative to Young's modulus and shear modulus

Figure 30: 3D surface plots of the theoretic effective strength ratio between the hollow and solid cylinder per unit air consumed as a function of $\frac{r}{r_2}$ and the internal pressure.

When having the length of both designs be variable a quite simple graphs is formed. Any increase in the length of both cylinders will result in a better relative performance of the hollow cylinder compared to the solid cylinder. When the length and the radius are similar in size any increase in length will still result in a better relative performance of the hollow cylinder, however, when the length is significantly larger than the radius this effect decreases and seems to have an asymptote. The surface plots representing this can be found in figure 31.

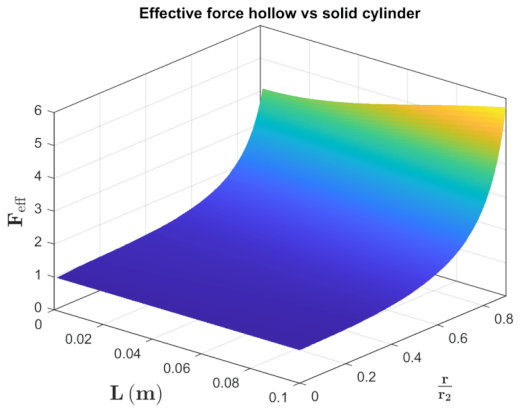

(a) Low values for the length

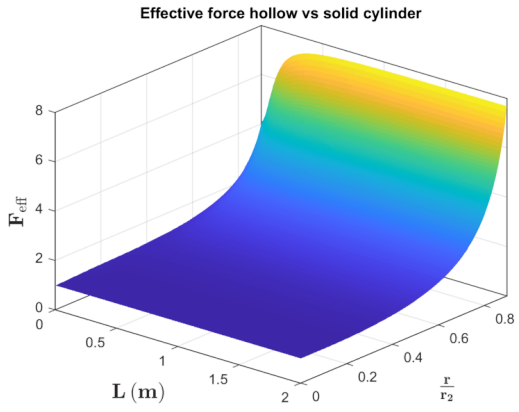

(b) Larger range for the length

Figure 31: 3D surface plots of the theoretic effective strength ratio between the hollow and solid cylinder per unit air consumed as a function of $\frac{r}{r_2}$ and the length of the cylinder.

The last two variables that can be changed are the shear and Young's modulus. For isotropic materials these two variables are directly link by equation 42. Changing the value for E, while keeping the relation given in equation 42 true, results in the observation that the optimal geometry is dependent on the Young's modulus value, which can be seen in figure 32. Similar to what was shown for the pressure, the Young's modulus graphs can be divided into two sections. The first section is for a low Young's modulus compared to the value used for the pressure. When the Young's modulus is relatively small compared to the pressure used, the optimal design is just using the solid cylinder. When the Young's modulus is large compared to the pressure the hollow cylinder design outperforms the solid cylinder. This is the same conclusion that was found when the pressure was used as the variable.
Next, the shear modulus was taken as the variable that is changed. This means that it is no longer directly related to the Young's modulus. Instead, the Young's modulus is treated as a static value while the shear modulus is varied. The corresponding graph can be found in figure 33. Similar to when the Young's modulus was changed, an increase in the shear modulus leads to an increase in the effective strength ratio of the hollow cylinder with respect to the solid cylinder. The main difference between the graph for the Young's modulus, which also incorporates

an increasing shear modulus, and the graph for just the shear modulus is mostly located in the lower region. In the graph for the Young's modulus, the hollow cylinder design did not outperform the solid cylinder design at all inner radii, however, it does when only the shear modulus is changed. However, this is dependent on the values used for the other variables. If the value for the Young's modulus and pressure are both set to 10 Pa instead of the reference values, the graph shown in figure 34 is obtained and a similar graph can be obtained when both of them are set to a same, much higher value of 1 GPa. The main difference is the location of the small bump, which is located close to the chosen value for the Young's modulus and pressure.
To obtain the surface plots given in figure 35, the value of either the Young's modulus or pressure was set to a very low value, while the other values were kept at their reference values. When the Young's modulus is lowered significantly, while the pressure it kept the same, results in a rather simple graph. When this is the case, the hollow cylinder will always outperform the solid cylinder, regardless of the value for the shear modulus. The graph obtained when lowering the pressure significantly is a lot more interesting where three different transitions can be seen. For low values of the shear modulus, the displacement of the cylinder is dominated by the shear modulus dependent term in equation 28. For high values of the shear modulus the behaviour is dominated by the Young's modulus dependent term. For the very low values of the shear modulus the behaviour is determined by the pressure dependent term in the part of the equation that is also dependent on the shear modulus. As the shear modulus starts to increase, it starts becoming large enough to the point where the pressure barely has any influence. As the shear modulus keeps increasing and starts to become similar in value to the Young's modulus, a combination of both determines the deformation. Increasing the shear modulus even further results in the behaviour being determined almost solely by the Young's modulus.

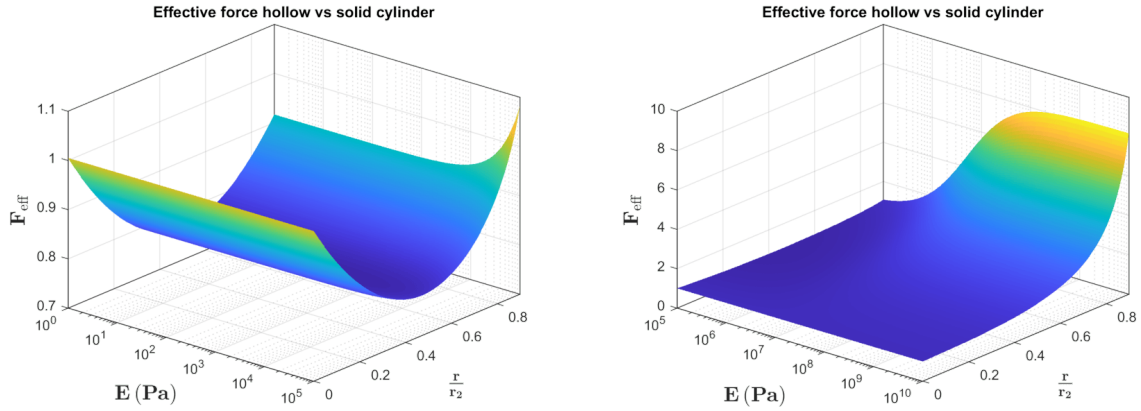

(a) Low Young's modulus relative to internal pressure (b) High Young's modulus relative to internal pressure

Figure 32: 3D surface plots of the theoretic effective strength ratio between the hollow and solid cylinder per unit air consumed as a function of $\frac{r}{r_2}$ and the Young's modulus.

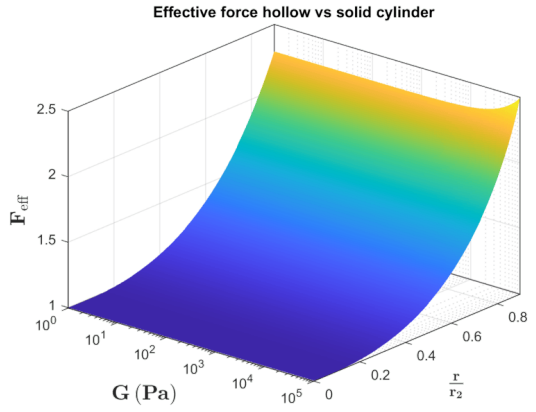

(a) Low shear modulus relative to internal pressure and Young's modulus

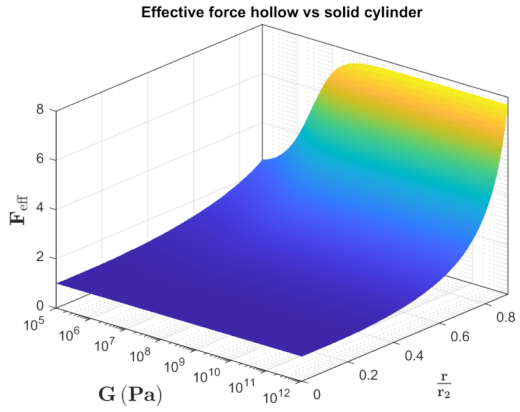

(b) High shear modulus relative to internal pressure and Young's modulus

Figure 33: 3D surface plots of the theoretic effective strength ratio between the hollow and solid cylinder per unit air consumed as a function of $\frac{r}{r_2}$ and the shear modulus.

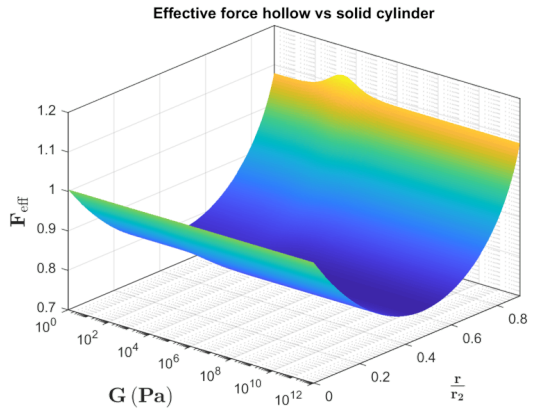

(a) Low pressure and Young's modulus

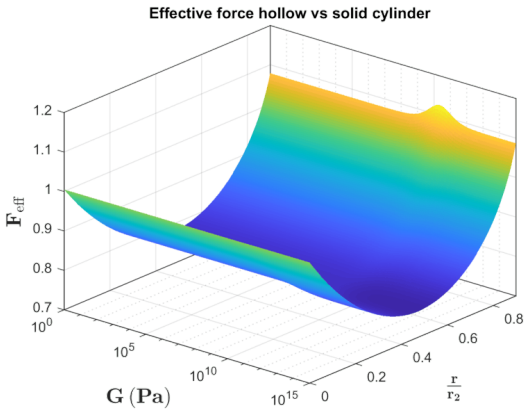

(b) High pressure and Young's modulus

Figure 34: 3D surface plots of the theoretic effective strength ratio between the hollow and solid cylinder per unit air consumed as a function of $\frac{r}{r_2}$ and the shear modulus.

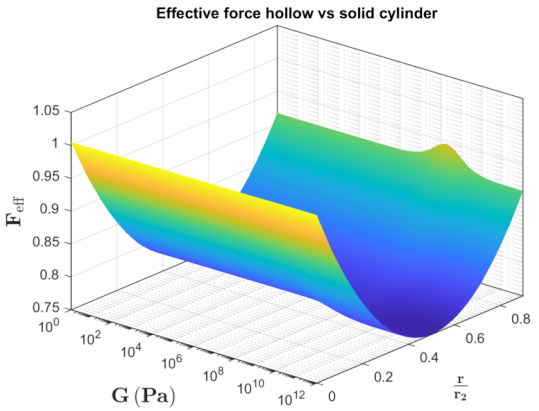

(a) Low Young's modulus

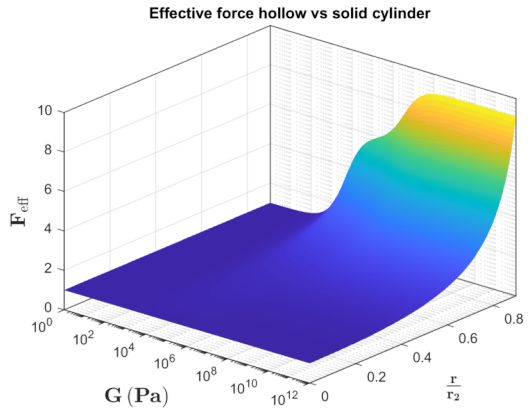

(b) Low pressure

Figure 35: 3D surface plots of the theoretic effective strength ratio between the hollow and solid cylinder per unit air consumed as a function of $\frac{r}{r_2}$ and the shear modulus.

To achieve the optimal values for each parameter and generate the largest output force on an absolute scale, one must refer to equation 28. The highest bending strength is achieved when the value for $w(x)$ is as low as possible, which is achieved by selecting the values of the variables as given in table 2. The optimization to achieve the highest possible output force is the exact same as for the Timoshenko beam equation, with the addition of also maximizing the pressure and wall thickness. Selecting the variables based on the aforementioned list would yield the strongest possible beam. However, as the variables approach infinity, the required volume of air does so as well. Designing a beam using these variables would not lead to the optimal force per unit air consumed. Beyond a certain point, the additional volume required outweighs the gained strength, in relative terms. Furthermore, having a very high Young's and shear modulus would prevent bending in the deflated state as well, eliminating the use of the actuator.
With all of the above observations and conclusions it can be stated that there is no distinctive better or worse design if all of the material properties can change independently over a large range. However, if the materials for the design are chosen using the guidelines above, the hollow cylinder design can outperform the solid cylinder design by a significant amount.
A few notes that should be made about the optimization problem is that this is solely based on the mathematical values not considering further implications of the chosen values. For example, choosing a material with an extremely low Young's modulus might, in theory, enable the production of a significantly stronger hollow cylinder compared to the solid cylinder. However, this does not necessarily indicate that it is the optimal value for this parameter. A very low Young's modulus would also cause the material to fail at much lower forces.

4.2 Prototype results

In order to characterize the newly proposed design and make a meaningful comparison with the old design, tests need to be performed. As described in the Methodology 3.6, the tests are performed on an UTM for a range of different pressures. The first performed test is for the solid cylinder at 25 kPa. The pressure of 25 kPa is relatively low and it could be observed that the solid cylinder design would not be able to withstand very high forces, since it was still flexible. With increasing pressures the stiffness of the prototypes increased.

4.2.1 Fitting pressure data

The data from the pressure sensor has a low resolution, resulting in a curve that looks like a step function. Assuming that the cross-sectional area remains approximately constant, due to the strain limiting behaviour of the textile sleeve and using equation 14, it can be demonstrated that the pressure exhibits an exponential behaviour with an asymptote. The asymptote is located at the point where the displacement equals the initial length. This would mean that the volume is equal to zero, resulting in an infinite pressure. The behaviour in the area of interest, which is relatively small displacements, follows a near linear behaviour. A polynomial fit function is used to approximate this behaviour. A first-order fit would be the most appropriate as this would enforce a linear relationship between the pressure and displacement. Figure 36a displays an example of the data and the corresponding first-order fit. It is evident that the first-order fit achieves a good alignment with the measured data. For some tests however, the fit is slightly less accurate due to an increased amount of leading values, which can be seen in figure 36b. These leading values are caused by the fact that both the test machine and the collecting of the pressure data had to be started manually and individually. For some tests, the time difference between starting both recordings was smaller than for other tests, which results in a different number of leading values for different tests. These leading values only have a very small influence on the data and the corresponding fit. Furthermore, due to some small fabrication errors in the created prototypes, the disk is not fully horizontal. This slight tilt of the disk further amplifies the effect of a less steep increase in pressure at the start of the experiments. Due to the tilt of the disk, the prescribed displacement of the UTM will only compress a portion of the cylinder causing the less steep pressure increase at the start. As can be seen in the figure 36b, the first order fit is much less centered on the middle of each plateau and has a slightly less steep slope compared to the second and third order fit. For the experiments with a larger amount of leading values, the higher order fits achieve better results. Although the leading values could have been manually removed from the data set to establish a more linear relationship and improve the fit between the measured data and the expected linear relation, it was decided against doing so due to the presence of fabrication errors in the prototypes. If the plateau observed in the data was solely caused by the delayed initiation of the test, the leading data points could have been omitted.

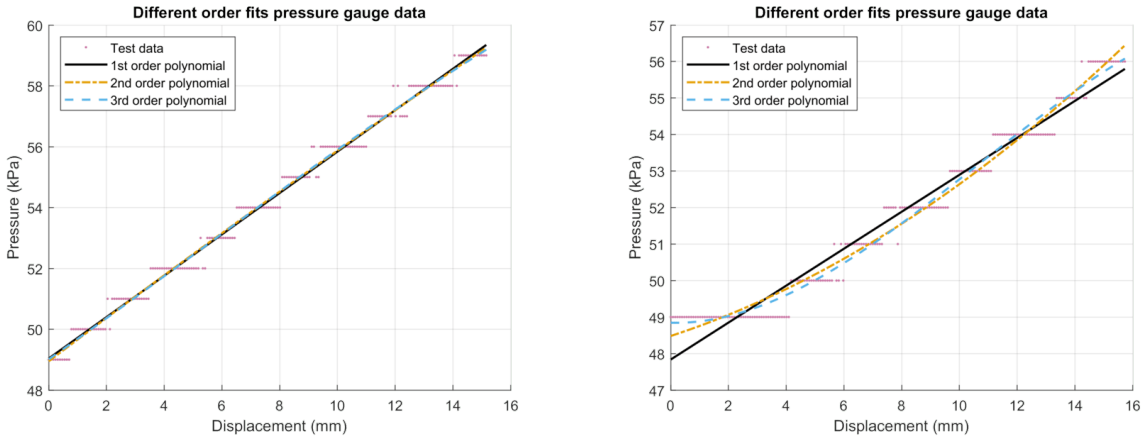

(a) Three different order polynomial fits on the pressure gauge data

(b) Three different order polynomial fits on the pressure gauge data, with more leading values

Figure 36: Polynomal fits for pressure-displacement data

4.2.2 Compression data

In figure 37 the force-displacement-pressure relation can be seen for both cylinder types. In this figure, the average of the three tests per prototype is taken for both the force and pressure, to create a clearer overview of the data. Figure 38a shows all six force-displacement relations for the solid cylinder, while figure 38b displays the corresponding relations for the hollow cylinder. In this figure and all subsequent figures, test 1,2 and 3 are conducted on the same prototype, while test 4,5 and 6 are performed on the second prototype, unless stated otherwise. In figure 39a and 39b the corresponding pressures can be seen.

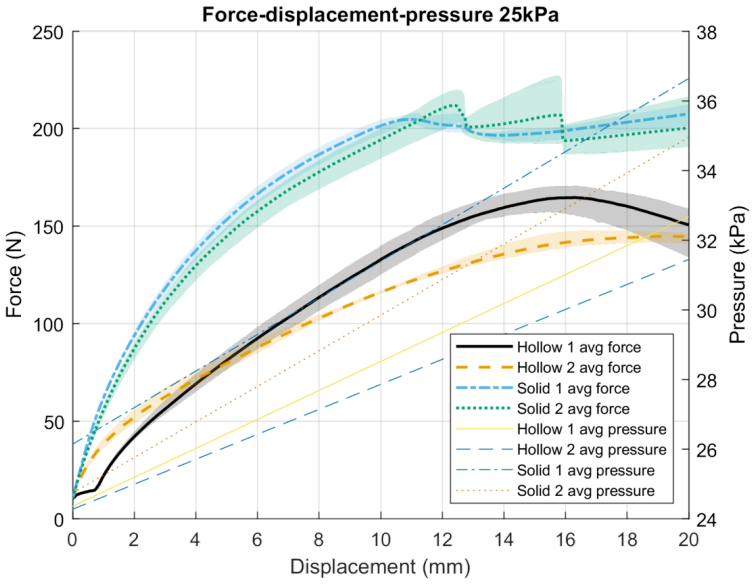

Figure 37: Force-displacement-pressure graph of both designs at 25 kPa

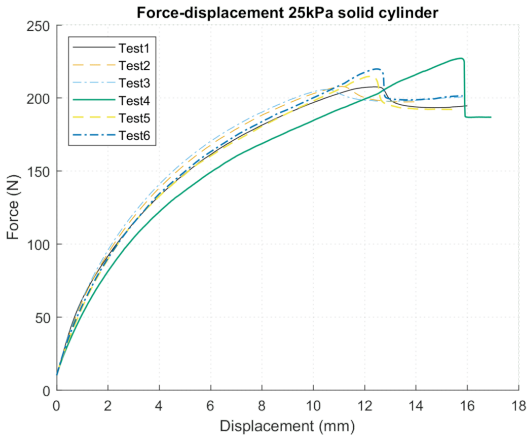

(a) Force-displacement graph of the solid cylinder design

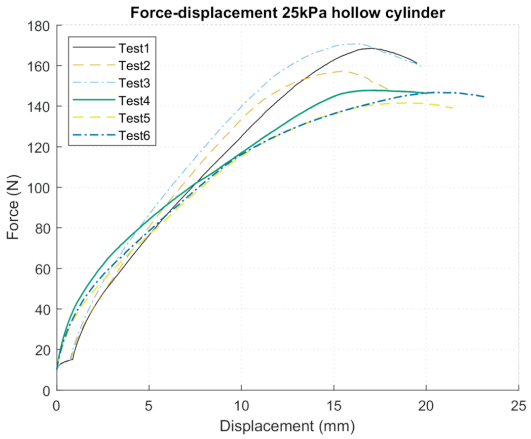

(b) Force-displacement graph of the hollow cylinder design

Figure 38: Force-displacement graphs at 25 kPa

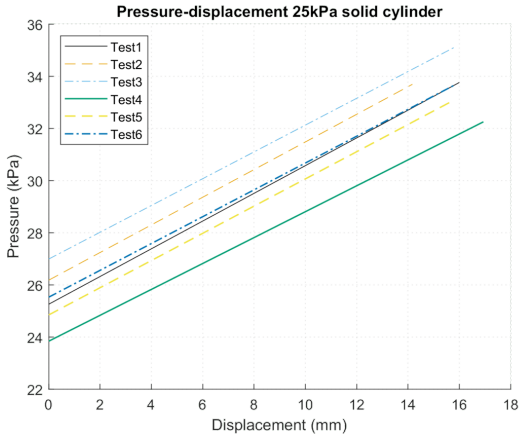

(a) Pressure-displacement graph of the solid cylinder design

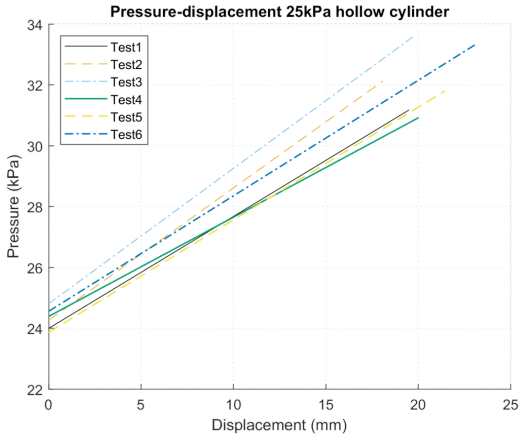

(b) Pressure-displacement graph of the hollow cylinder design

Figure 39: Pressure-displacement graphs at 25 kPa

For the solid cylinder, a sharp change in the force can be observed, which is caused by the buckling of the cylinder. As outlined in the Methodology, the test is stopped shortly after reaching the point of buckling due to concerns that the structure may not be able to withstand additional load. If the prototype is not moved between subsequent tests, the point of buckling occurs in the same place.
From the graph it can be seen that there is no further increase in the force after the structure buckles, for the solid cylinder. For the hollow cylinder it can be seen that the force keeps decreasing the further the prototype is compressed. This means that there is no noticeable extra force needed in the vertical direction to achieve further displacement. This is for a large part due to the way the soft actuator buckles. The buckling causes the top disk of the cylinder to be tilted and it keeps tilting further, the larger the displacement becomes. However, it is evident that the pressure continues to rise with increasing displacement, which indicates that the cylinder is still undergoing compression. This compression does not result in any extra forces in the axial direction due to the buckling.
The buckling from the hollow cylinder is much more gradual than for the solid cylinder and the buckling itself is also much less severe. The solid cylinder buckles somewhere around the middle of the length of the cylinder, which results in a large tilt of the top disk and also a fast and sudden drop in force. The hollow cylinder also buckles close to the middle of the cylinder, however, this buckling is much more gradual. The cylinder slowly starts to bend more and more. The hollow cylinder also has a much less sharp tilt of the top disk.
The buckling of both cylinders can already be observed slightly before the actual buckling happens. The textile sleeve starts to wrinkle, which is more visible on the solid cylinder. The wrinkling becomes more severe as the compression continues and shortly after the onset of the wrinkling the cylinder buckles, which is accompanied by an

audible sound for the solid cylinder. The hollow cylinder creates no audible sounds when buckling, most likely due to the much more gradual and change of shape. The sound produced by the buckling is louder at higher pressures. The increase in pressure as a function of the displacement is steeper for the solid cylinder design with respect to the hollow cylinder design. This same trend is visible for both the first and second iteration of each of the prototypes. This trend is also visible at all the other pressures tested. There is no clear explanation as to why this effect occurs, since the number of leading values is relatively similar for both designs. Even though the tests for the solid cylinder are generally ended at a slightly lower displacement, the pressure is the same or even higher. From the theory it is expected that the slope for the pressure curves should be the same for all the tests, since the volume of the cylinder is linearly correlated with the pressure if it is assumed that there is no radial expansion for the prototypes. A possible explanation would be that since the hollow cylinder can expand both it's inner and outer wall this would result in a bigger increase in volume with respect to the solid cylinder which can only expand it's outer wall outward. Furthermore, it is possible that the radial expansion for both cylinders is almost the same in absolute terms, which would result in a larger relative increase of the volume for the hollow cylinder with respect to the solid cylinder. This would result in a smaller increase in the pressure which can be observed as a less steep pressure-displacement curve.

All the other graphs which include the force-displacement and pressure-displacement curves are the averages. The results from each individual test are included in appendix B. Similar to the results shown in figure 38b, all the other force-displacment graphs show a small deviation between tests performed on the same prototype and a larger variation between the different iterations of the same prototype. The variations in the results from the tests are also pressure dependent, where a higher pressure results in a lower relative variation, for the same prototype.

Figure 40a, 40b and 40c, will show the force-displacement-pressure graphs for 50 kPa, 75 kPa and 100 kPa respectively. In these graphs both the pressure and force are averaged for each iteration of each prototype and this data is interpolated and extrapolated over the entire displacement work space from 0 mm to 20 mm. The fit for this data is created using the linear interpolation function within Matlab. To be able to average the data properly a fit had to be used to have the data points coincide. It was decided to also extrapolate the data over the remaining displacement up to 20 mm to have evenly spaced curves. The interpolation fit function creates straight lines between neighbouring points, which works very well for the large number of data points available in the data sets. The extrapolation using this fit function will create a linear line with the same slope as the last two data points, which is an assumption which works quite well for the data that was recorded past the point of buckling. It should be noted that this fit function creates a wrong curve for the data of the first iteration of the solid cylinder at 100 kPa, which is shown in figure 40c. This is because the test was ended by reaching the maximum force of 750 N instead of the buckling point of the cylinder, which might occur shortly after this point or might be significantly higher, but can only be roughly estimated from this data and the data from the other tests. A rough estimate for the maximum buckling force would be between 800 N to 900 N at a pressure of 100 kPa.

A small plateau in the force-displacement curves can be observed for the first three tested performed on the hollow cylinder. This small force plateau is most likely caused by an improper test setup on the day these tests are performed. All tests for the first iteration of the hollow cylinder are performed on the same day. In figure 23b the connection between the force sensor and linear guidance can be seen. The connection between these was most likely not thight enough, leaving room for small displacement between the linear guidance and the metal cylinder. This small movement can be observed in the force-displacement graphs as a force plateau, since the force required for this movement is significantly smaller than the force required for the compression of the prototype.

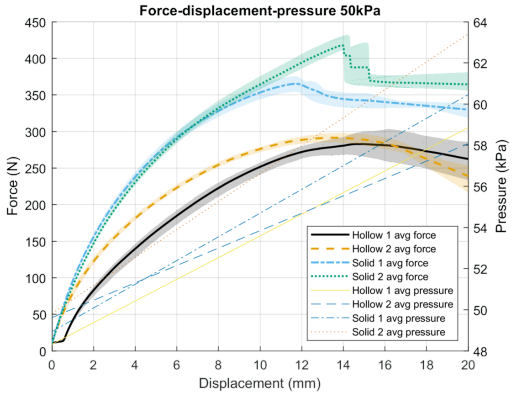

(a) Force-displacement-pressure graph of both designs at 50 kPa

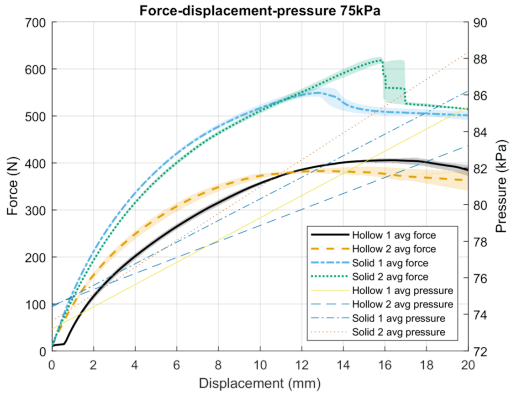

(b) Force-displacement-pressure graph of both designs at 75 kPa

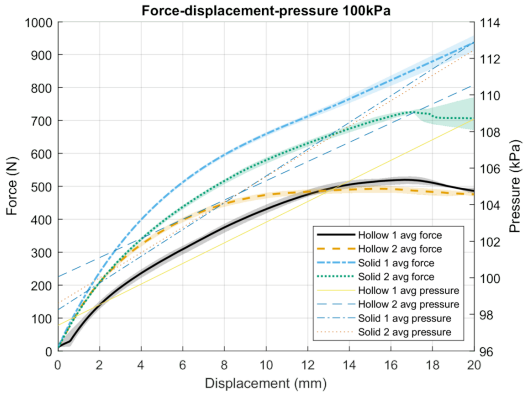

(c) Force-displacement-pressure graph of both designs at 100 kPa

Figure 40: Averaged force-displacement-pressure graphs

4.2.3 Deviations observed in data

There are a few exceptions to the previously mentioned trends in the data, which will be shown here and further elaborated on. The first deviations is that of the solid cylinder at 25 kPa, which can be seen in figure 38a. The results from both measured prototypes are very close together, whereas at higher pressure the deviation between the different iterations is much more pronounced. A possible explanation for this behaviour could be the relatively low pressures at which these tests are performed. Due to the low pressure the tilt of the top disk was much less pronounced, which seems to have a significant effect on the buckling behaviour.

For the solid cylinder the first test performed tends to always achieve a higher displacement before the point of buckling. This effect is more noticeable in the second iteration compared to the first iteration. A possible explanation for this behaviour would be that the fabric has relaxed slightly after performing the first test. The second and third test are performed shortly after the first. It was also noticed that the prototypes tend to always buckle in the same spot. It is possible that after the first failure the structure has been weakened causing it to buckle at a lower displacement.

This same effect is not visible in the graphs for the hollow cylinder design. A possible explanation for this behaviour would be the increased stiffness of the fabric structure of the hollow cylinder design. The increased stiffness would result in less relaxation of the fabric, which could explain the more consistent result.

The results from the hollow cylinder tests at 50 kPa also differ from the general trend observed in the results. The prototype was moved and rotated between Tests 1, 2 and 3. This movement seems to have resulted in a larger variation between the different tests. The movement and rotation in these tests was included to investigate the orientation dependency of the produced prototypes. The force will no longer have been applied at exactly the same location due to human factor in setting up the tests. This combined with small fabrication errors in the prototype has a noticeable impact on the results.

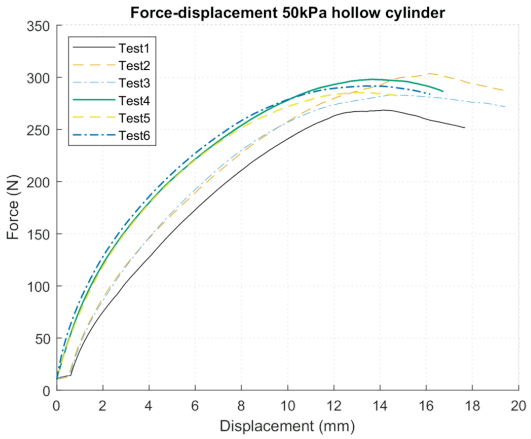

(a) Force-displacement graph of the hollow cylinder design at 50 kPa

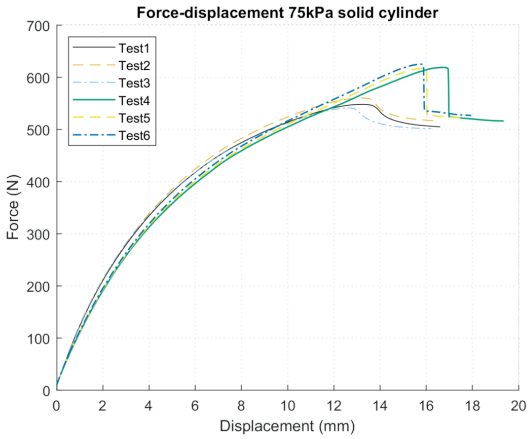

(b) Force-displacement graph of the solid cylinder design at 75 kPa

Figure 41: Force-displacement graphs of tests which deviated from the average

Similarly to the hollow cylinder at 50 kPa, the solid cylinder was moved and rotated during the tests performed on the first iteration prototype at 75 kPa. Unlike the hollow cylinder, the rotation of the solid cylinder had very little impact on the results of the solid cylinder. The solid cylinder no longer achieved the highest displacement during the first performed test, but no further impact was observed from the introduced rotations. The solid cylinder also seems to be orientation dependent, but to a much lesser degree than the hollow cylinder design. This could however also depend on the orientations taken. The difference between the hollow and solid cylinder is most likely a combination of different causes. First of all, the solid cylinder will be more axi-symmetric, due to the inconsistent behaviour of the balloons. Furthermore, the fabrication errors of the hollow cylinder will have been larger compared to the solid cylinder, due to the much more complex fabrication process.
Another test that differs from the expected behaviour is Test 4 of the hollow cylinder at 75 kPa, which can be seen in figure 42a. The pressure increase is significantly less compared to the other curves. The most likely cause for this behaviour is a small leakage in the test setup. The hose connected to the pneumatic source had a issue where at a certain orientations it would start leaking air. The effect of this slightly lower pressure can also be observed from the force-displacement graph found in figure 42b. The curve is slightly lower than the other two tests performed on the same prototype, however, the difference is so small it is within the margin of error.

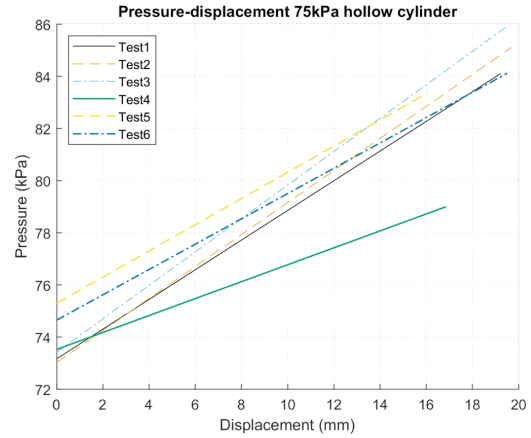

(a) Pressure-displacement graph of the hollow cylinder design at 75 kPa

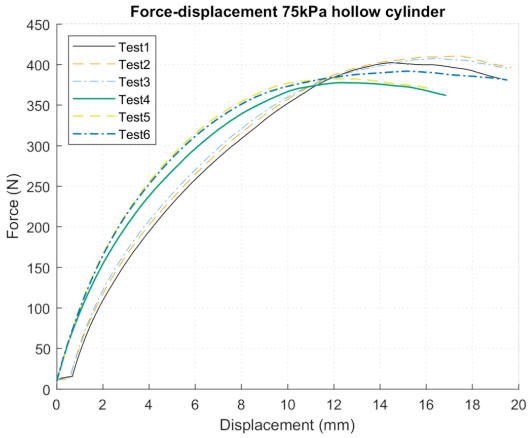

(b) Force-displacement graph of the hollow cylinder design at 75 kPa

Figure 42: Force and pressure curves for the hollow cylinder at 75kPa

The last graph which shows deviating behaviour is that of the solid cylinder at 100 kPa, which can be seen in figure 43. The initial threshold for the maximum force was set at 750 N, as was mentioned in section 3.6. In the later tests this was changed to 900 N. Furthermore, the first iteration prototype is outperforming the second iteration in these tests, which is opposite of all the other tests. This is because Test 1, 2 and 3 are performed

on the second iteration prototype, while Test 4, 5 and 6 are performed on a third iteration, as was described in section 3.6. The large differences between the results of the different iterations illustrates the influence of small fabrications errors, considering that each prototype was produced according to the same reference dimensions.

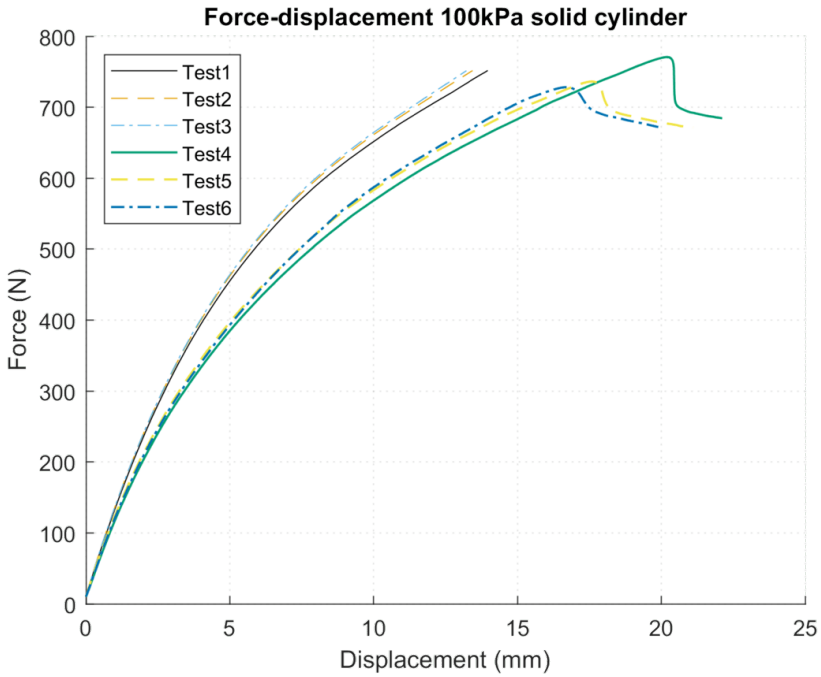

Figure 43: Force-displacement graph of the hollow cylinder design at 100 kPa

4.2.4 Comparison measurement and theoretical data for compression

A table can be created using the maximum force at the point of buckling for each prototype, showcasing the differences between the different variations of the prototypes and the influence of the pressure on these differences. The mentioned maximum force ratio's can be found in table 3, while the maximum forces can be found in table 4. In this table certain cells have been marked with a color. The cells marked with blue are outlier values. The ratio H1/H2 at 25 kPa has been marked because the ratio found is much higher than at the other pressures. A possible explanation for this would be increased impact of the structural stiffness due to the low pressures. Similarly the value for S1/S2 has been colored blue as well, since this ratio is close to 1 while this is not the case at higher pressures. A possible explanation for this would be that due to the low pressure the tilt of the top disk is much less pronounced. This tilt was mainly observed for the first iteration of the prototype and not so much for the second iteration and mostly at higher pressures.
The values marked with red are all the experiments that include the first iteration of the solid cylinder at 100 kPa. These actual ratio should be lower than the value depicted in the table since the test was stopped 750 N instead of reaching buckling, which would have resulted in a higher maximum force. The ratio S1/S2 would have been higher since S1 is in the numerator rather than the denominator. Furthermore, the ratio of S1/S2 at 100 kPa is higher than 1, unlike the other pressures. This is due to the failure described in section 3.6, which required the tests to be performed on a third iteration prototype.
The values are marked with green due to the relatively large deviation from the theoretical ratio of 0.69. The most likely explanation for this observed behaviour is the pressure dependency of the length and diameter of the prototypes in combination with small production errors.

Table 3: Table containing ratio's of maximum force achieved at buckling, where H1 and H2 are iteration 1 and 2 of the hollow prototype respectively and S1 and S2 are iteration 1 and 2 of the solid cylinder respectively. Blue highlighted are outlier values, green highlighted are outlier values away from expected ratio 0.69 and red values correspond to test from solid cylinder 1 at 100 kPa, which is terminated at 750 N, while maximum force value should be higher

	H1/H2	S1/S2	H1/S1	H1/S2	H2/S1	H2/S2
25kPa	1.1377	0.9659	0.8045	0.8790	0.7071	0.6829
50kPa	0.9705	0.8744	0.7745	0.6772	0.7980	0.6978
75kPa	1.0602	0.8883	0.7389	0.6564	0.6970	0.6192
100kPa	1.0551	1.0334	0.6932	0.7164	0.6570	0.6790

Table 4: Maximum force (N) for the average of each prototype, where H1 and H2 are iteration 1 and 2 of the hollow prototype respectively and S1 and S2 are iteration 1 and 2 of the solid cylinder respectively. Red highlighted value is due to early termination of test at 750 N, while actual maximum force should be higher

	H1	H2	S1	S2
25kPa	164.6740	144.7404	204.7019	211.9368
50kPa	282.8271	291.4204	365.1820	417.6524
75kPa	405.4950	382.4746	548.7513	617.7366
100kPa	519.6745	492.5387	749.6459	725.4397

The values for the maximum force, as shown in table 4, can be evaluated using a simplified approximation, which uses Boyle's law as given in equation 13. Evaluating this equation for the different tests at the different pressures and comparing them with the experimental results can provide insight in possible failures in the test setup if large differences are observed. The ratio between the theoretical and experimentally found pressures at the point of buckling can be found in table 5. Table 6 and table 7 represent the theoretical and measured pressures at the point of buckling respectively. Both the relative and absolute difference between the found pressures diminish as the pressure increases. The theoretical pressure can be found according to,

$$P_2 = \frac{P_1 V_1}{V_2} = \frac{P_1 \pi r_1^2 L}{\pi r_2^2 (L-d)} = \frac{P_1 r_1^2 L}{r_2^2 (L-d)}, \tag{51}$$

where r is the radius, L the length of the cylinder and d the displacement/compression in axial direction. Assuming that the values for the length, pressure and displacement are correct with a high accuracy, since they have been measured, would only leave the radius as a variable. From the results it was observed that the theoretical pressure is always lower than the experimentally observed pressure which would mean that the radius has to decrease as the cylinder is compressed. This is very counter intuitive and no explanation has been found for the observed behaviour. A constant offset or error in the measurement setup also does not account for the observed behaviour as this should lead to a increasing error rather than a decreasing error as the pressure increases. If the pressure in state 1 would have been off by a constant value it is likely that the pressure in state 2 would have been off by the same value, which would also not explain the observed behaviour. At higher pressures, the obtained pressure values fall within the margin of error, particularly when considering the low resolution of the measurement data 1 kPa and the linear fit applied to it. However, if the assumption of the constant radius between situation 1 and 2 was not made, the differences between the theoretical model and the measurement data would have been even larger, since in reality, the radius most likely increases as the cylinder is compressed.

Table 5: Ratio between the theoretically calculated pressure according to Boyle's law and the measured pressure during the experiments

	H1	H2	S1	S2
25kPa	0.860	0.792	0.872	0.855
50kPa	0.954	0.910	0.940	0.911
75kPa	0.953	0.940	0.977	0.947
100kPa	0.974	0.950	0.982	0.987

Table 6: Theoretically calculated pressure (kPa) according to Boyle's law

	H1	H2	S1	S2
25kPa	26.8	24.8	27.8	26.6
50kPa	53.5	50.4	52.3	54.0
75kPa	79.2	75.4	80.1	80.7
100kPa	103.9	102.7	106.2	108.9

Table 7: Measured pressure (kPa) at the moment of buckling

	H1	H2	S1	S2
25kPa	31.1	31.4	31.9	31.1
50kPa	56.1	55.4	55.7	59.3
75kPa	83.1	80.2	82.0	85.3
100kPa	106.8	108.1	108.1	110.4

The combination of the calculated pressure and the prototypes geometry can be used to calculate the theoretical output force of the cylinder. The ratio between the calculated output forces and the measured force at the point of buckling can be seen in table 8, while the measured and theoretical forces can be found in table 4 and table 9, respectively. The found ratio's between the theoretical model and the measurement data are quite far off from the golden ratio of 1, which would have been a perfect fit between the theoretical and measurement data. The difference between the theoretical values and measurement data was already expected due to the large differences found in the pressures.

Table 8: Ratio between the theoretically calculated force according to Boyle's law and the measured force during the experiments. Red highlighted value is due to early termination of test at 750 N, while actual maximum force should be higher

	H1	H2	S1	S2
25kPa	0.715	0.829	0.865	0.797
50kPa	0.818	0.810	0.912	0.823
75kPa	0.873	0.923	0.929	0.831
100kPa	0.908	0.977	0.901	0.955

Table 9: Maximum force (N) calculated according to Boyle's law

	H1	H2	S1	S2
25kPa	117.8	119.9	177.1	169.0
50kPa	231.4	236.1	333.0	343.6
75kPa	354.0	353.1	509.5	513.6
100kPa	472.0	481.2	675.5	693.1

4.2.5 Improved fit

To examine the pressure-sensitive behaviour and identify potential production errors, the radius of the two different prototypes was measured at the various pressures. The measurements were only performed on the latest iteration of each prototype, as the previous iterations had already failed before the additional measurements were performed. For both prototypes the diameter was measured at the middle of the prototype, where the diameter is largest, because the top and bottom are fixed at a diameter of 9.0 cm. The solid cylinder showed a stronger pressure sensitive behaviour. The measured diameters can be found in table 10 below.
Another factor that might contribute to the difference between the theoretical model and the experimental results is the initial stiffness of the cylinders. The initial stiffness of the solid cylinder is negligibly small, but the stiffness of the hollow cylinder was measured using the UTM. A force of about 10 N was required to compress the deflated hollow cylinder. The theoretical force can be calculated according to,

$$F = P_2 A + b, \tag{52}$$

where F is the force, P_2 is the pressure, A is the cross-sectional area and b is the initial stiffness of textile sleeve, which is 0 N for the solid cylinder and 10 N for the hollow cylinder prototype. Substituting the measured values into equation 52, results in table 11. It has to be noted that the measured pressure has been used for these calculations instead of the calculated pressure due to the large differences observed.

Table 10: Measured diameter (mm) at various pressures

	R_{s1}	R_{h1}	R_{s2}	R_{h2}
25kPa	90.0	92.5	93.5	89.5
50kPa	91.5	92.5	95.0	90.5
75kPa	93.0	92.5	96.5	91.0
100kPa	94.0	92.5	97.5	91.0

Table 11: Ratio between the theoretically calculated force and the measured force during the experiments corrected. Red highlighted value is due to early termination of test at 750 N, while actual maximum force should be higher

	H1	H2	S1	S2
25kPa	0.879	1.007	1.070	1.006
50kPa	0.921	0.884	1.081	1.006
75kPa	0.955	0.978	1.092	1.010
100kPa	0.952	1.017	1.076	1.137

The calculated force ratio's only achieve a good fit for the prototype of which the diameter was measured, with the exception of the hollow cylinder at 50 kPa. The cylinder was rotated during these experiments, which seems to have significantly influenced the results of these tests. Furthermore, the force ratio of the solid cylinder at 100 kPa also differs significantly from the optimal ratio of 1. This large difference can be attributed to the fact that the results from this test are actually from the third iteration prototype, which would most likely have had a different diameter.

To achieve a good fit between the measurement data and the theoretically calculated values an estimation of the diameter of the first iteration prototypes has been made as well, which can also be found in table 10, while the force ratios can be found in table 12. The change in diameter of the solid cylinder as a function of the pressure is the same as for the second iteration of the solid cylinder. For the hollow prototype the best fit is achieved when the diameter is not scaled as a function of the pressure, which is not in full agreement with the measured diameters. The diameter of the hollow cylinder is the average of two measured diameters at different orientations. It is not that unlikely that the first iteration prototype was more symmetric and would have almost no radial expansion.

Table 12: Ratio between the theoretically calculated force and the measured force during the experiments fully corrected. Red highlighted value is due to early termination of test at 750 N, while actual maximum force should be higher

	H1	H2	S1	S2
25kPa	0.990	1.007	0.992	1.006
50kPa	0.996	0.884	1.003	1.006
75kPa	1.012	0.978	1.014	1.010
100kPa	1.006	1.017	1.001	1.137

To provide a visual representation of the aforementioned experimental data, graphs depicting the volume-normalized force-displacement curves have been generated, which can be seen in figure 44. The volumes of the different prototypes have been calculated using the previously mentioned diameter values and an assumed length of 18 cm. From these curves, it is readily apparent that the performance of both the hollow and solid cylinder per unit volume is almost identical.

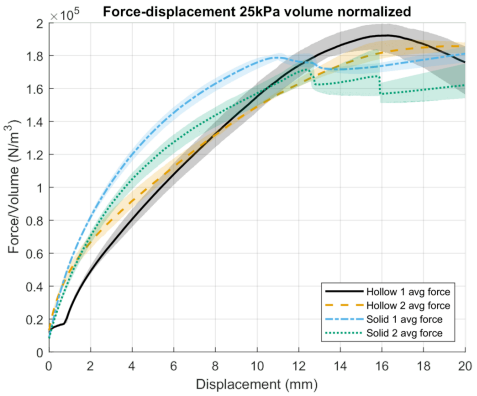

(a) Force-displacement-pressure graph of both designs at 25 kPa

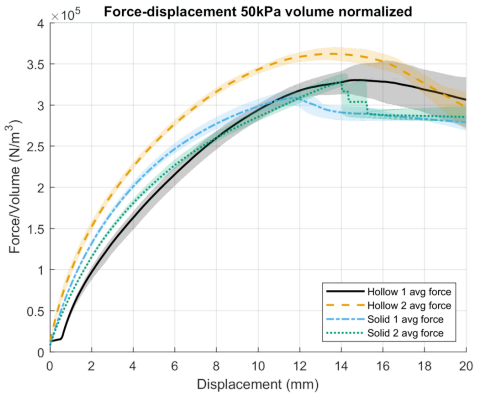

(b) Force-displacement-pressure graph of both designs at 50 kPa

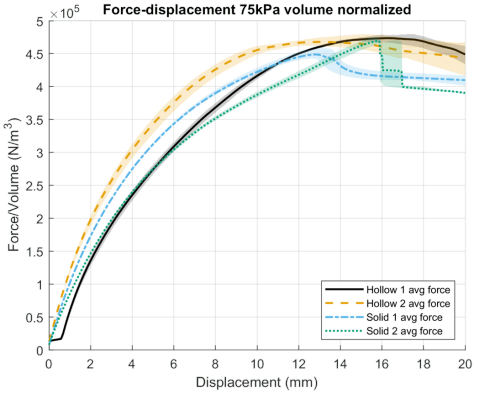

(c) Force-displacement-pressure graph of both designs at 75 kPa

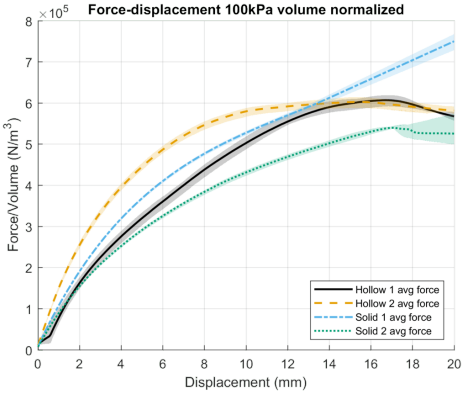

(d) Force-displacement-pressure graph of both designs at 100 kPa

Figure 44: Averaged results from compression tests volume normalized including error margins

4.3 Actuation speed test

To demonstrate the improvements in inflation speed of the new design, inflation speed tests were performed according to the method described in section 3.7. The test results are visualized in figure 45, where it can be seen that the hollow cylinder inflates faster than the solid cylinder design. The hollow cylinder is able to inflate up to the threshold pressure of 75 kPa in 90.3 % of the time it takes the solid cylinder design to achieve this same pressure. The hollow cylinder is able to achieve the pressure of 85 kPa in 93.3 % of the time it takes the solid cylinder to achieve this pressure. The lower the required pressure the larger the difference in time required to achieve this pressure. Comparing the time it takes the hollow cylinder to fully inflate with the time it takes the solid cylinder to fully inflate and reach the same pressure, shows a difference of 68 %, which is identical to the volume ratio between the two different designs. This is in line with the expectations for inflation time.
Furthermore, the minimal pressure to start inflation is higher for the hollow cylinder than for the solid cylinder design. This is solely caused by the much lower stiffness of the condom in comparison to the party balloons.
As the pressure inside the prototype approaches the pressure of the air supply, the rate at which the pressure increases over time decreases. This reduction occurs due to the diminishing difference in pressure between the prototype and the air supply.

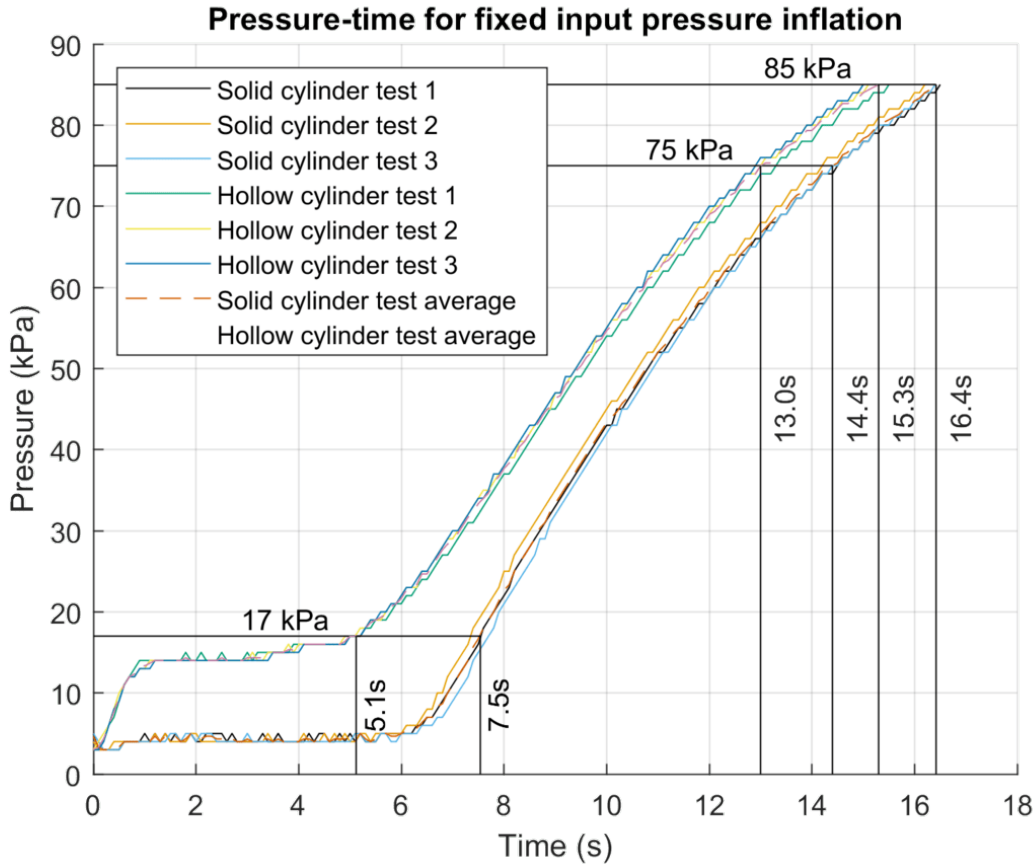

Figure 45: Pressure-time inflation test performed at a fixed input pressure of 100 kPa for both the hollow and solid cylinder design

4.4 Bending test

As was described in section 3.8, one of the possible applications of the produced soft actuators is to help with the extension of the knee. To perform this function in an efficient manner it is important to have a high bending stiffness. The bending stiffness ratio between the original design prototype and the improved hollow design prototype was determined with the help of bending tests. For the new design to be better than the original design, the force output of the actuator should be as high as possible while the internal volume should be as low as possible. Similar to the compression tests, the tests are performed over the range of 25 kPa to 100 kPa, with intervals of 25 kPa. The bending tests are only performed for a single iteration of the prototype, since it was expected that the conclusions drawn will be the same as when the tests would be performed for multiple iterations of the prototype.

4.4.1 Fitting pressure data

Similar to the pressure sensor data from the compression test, the data from the bending tests also has a low resolution of 1 kPa. As was described in section 4.2.1 a first order linear fit was applied here as well. Two example graphs for the pressure data can be seen in figure 46. In figure 46a it seems like there are quite large differences between the different tests performed, but this is only due to the very small range on the y-axis and the low resolution of the measurement data. The pressure is almost constant over the entire displacement range and only very minor deviations are observed. In figure 46b the fitted pressure from a different experiment can be seen, which has all curves close together, but also shows only very minor changes in pressure over the entire displacement range.

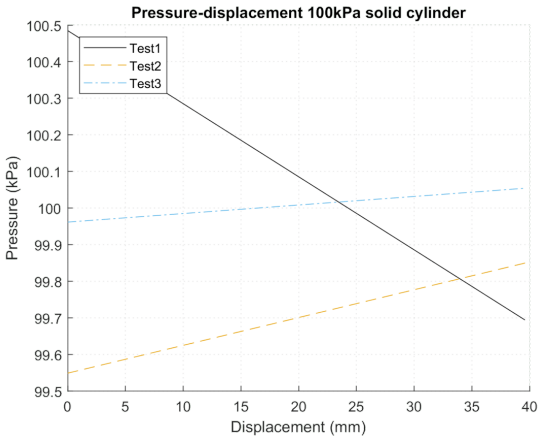

(a) Seemingly large deviations in pressure measurement data

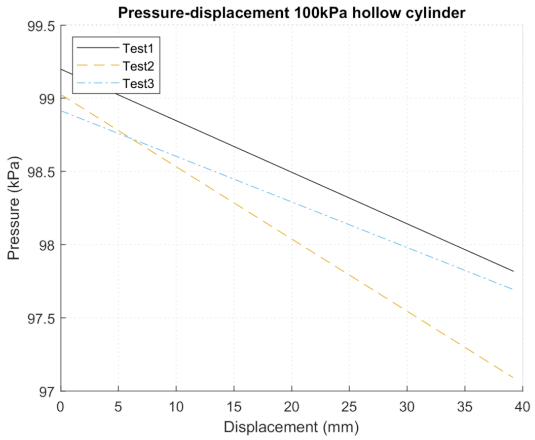

(b) Low deviations in pressure measurement data

Figure 46: Example graphs for the pressure development during the bending tests

For the test performed on the hollow cylinder at 75 kPa, which can be found in figure 47, a larger variation can be observed. This is most likely caused by a small leakage in the test setup, which allowed air to escape during the experiment. Even though the deviation is larger than in other experiments, the pressure drop is only about 3 %.

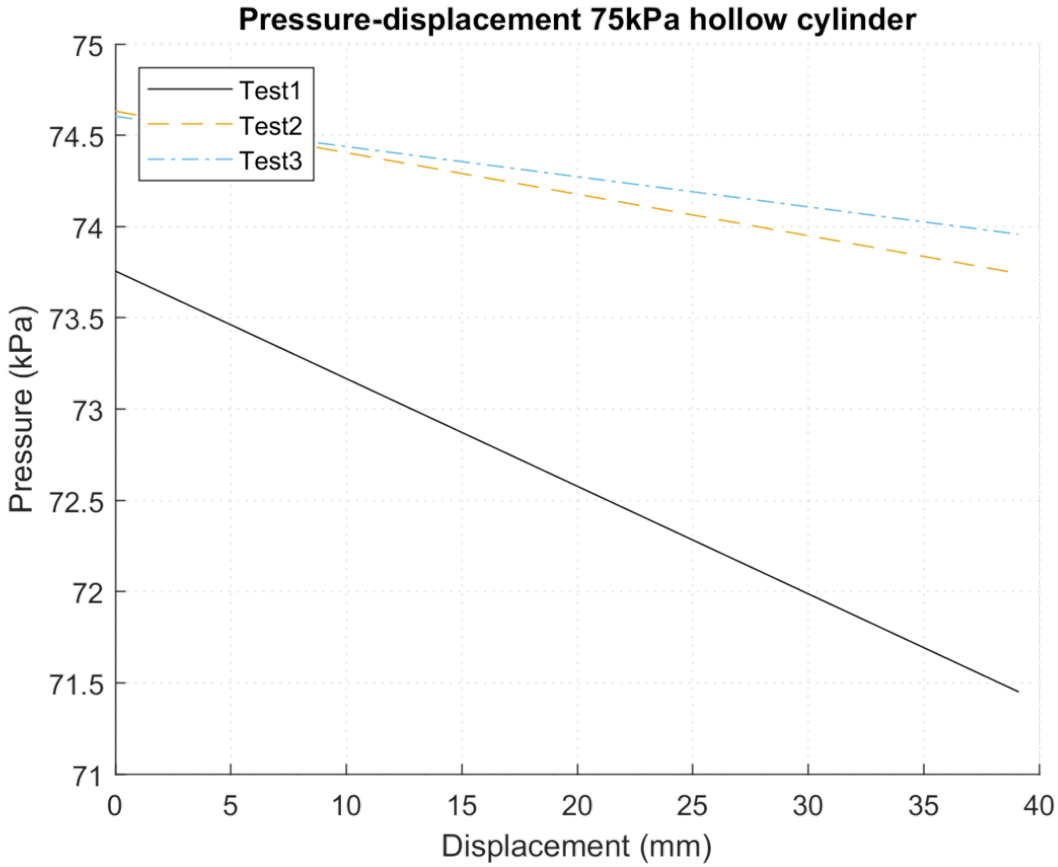

Figure 47: Pressure-displacement curve for the hollow cylinder at 75 kPa

4.4.2 Bending test data

The force required for bending was also recorded during the experiments. In figure 48, example graphs can be found that show the general behaviour of the prototypes during the experiments. For the solid cylinder design, the later tests tend to require slightly more force than the first test. A possible explanation for this behaviour would the a slight extension of the prototype. This extension was observed because the UTM had to be aligned with the free end of the prototype after each experiment. An increase in length would result in a lower force requirement for bending, but this slight extension might have been accompanied by a small radial expansion as well. Furthermore, the slightly larger prototype results in larger strains in the textile, which in turn could increase the Young's and shear modulus of the material. This behaviour was not observed in the results of the hollow cylinder design. The hollow cylinder design was also less prone to the elongating behaviour due to the higher stiffness of the design. All of the pressure-displacement and force-displacement curves for the performed tests can be found in appendix C.

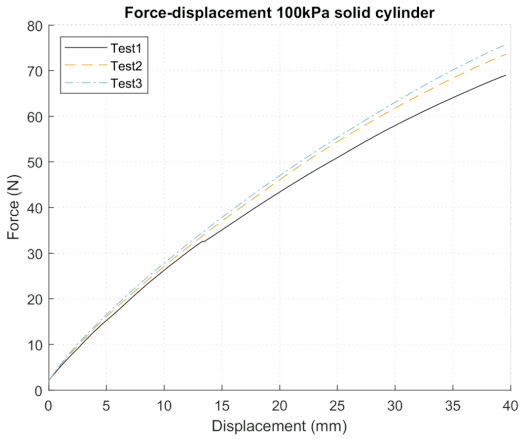

(a) General trend observed in the force-displacement curve for the solid cylinder prototype

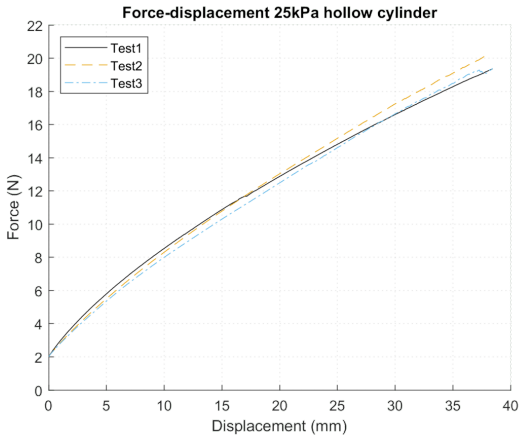

(b) Example of force-displacement curve from the hollow cylinder prototype

Figure 48: Example graphs for the pressure development during the bending tests

In figure 49 the averages of both prototypes are plotted, for both the force-displacement curves as well as the pressure-displacement curves. By observing these graphs, it becomes clear that when the applied pressure increases, so does the difference between the maximum force of both design. It can also be observed that as the prototype reaches larger deformations, the force required to achieve further displacement decreases. In the theoretical ideal case it is expected that the force-displacement curve shows a near linear behaviour, according to equation 28. It does however have to be noted that this function makes a couple of assumptions which might not be true for the produced prototypes. The bending of the prototypes might differ from the expected deformation behaviour for which this formula applies. The prototypes produce a sharp bend close to the clamped end, while remaining straight over the length of the prototype, whereas the theoretical model describes bending over the entire length of the prototype. An example of the described behaviour can be seen in figure 50, where figure 50a shows the prototype shortly after the experiment has started and figure 50b shows the prototype at the end of the test, once it has reached the prescribed displacement of 40 mm.

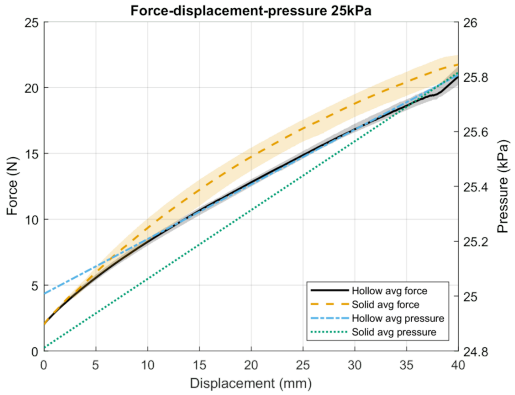

(a) Force-displacement-pressure graph of both designs at 25 kPa

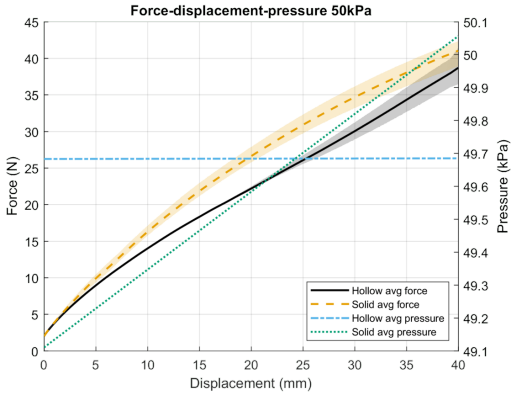

(b) Force-displacement-pressure graph of both designs at 50 kPa

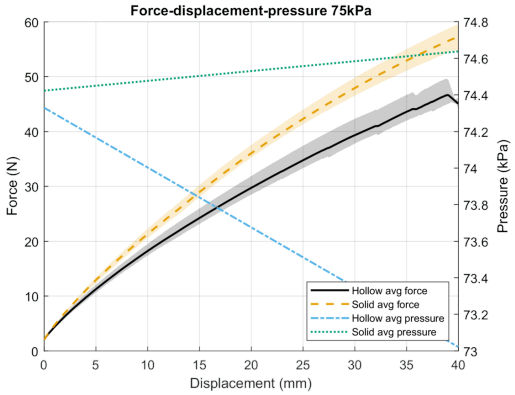

(c) Force-displacement-pressure graph of both designs at 75 kPa

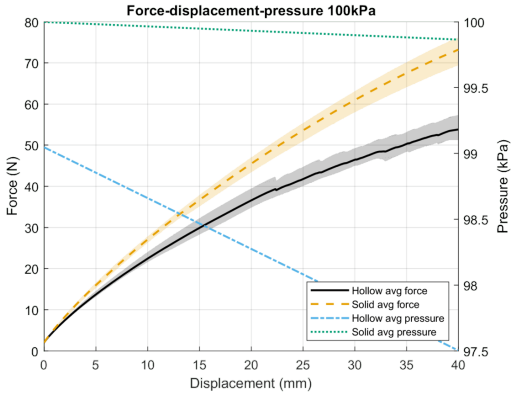

(d) Force-displacement-pressure graph of both designs at 100 kPa

Figure 49: Averaged results from the bending tests

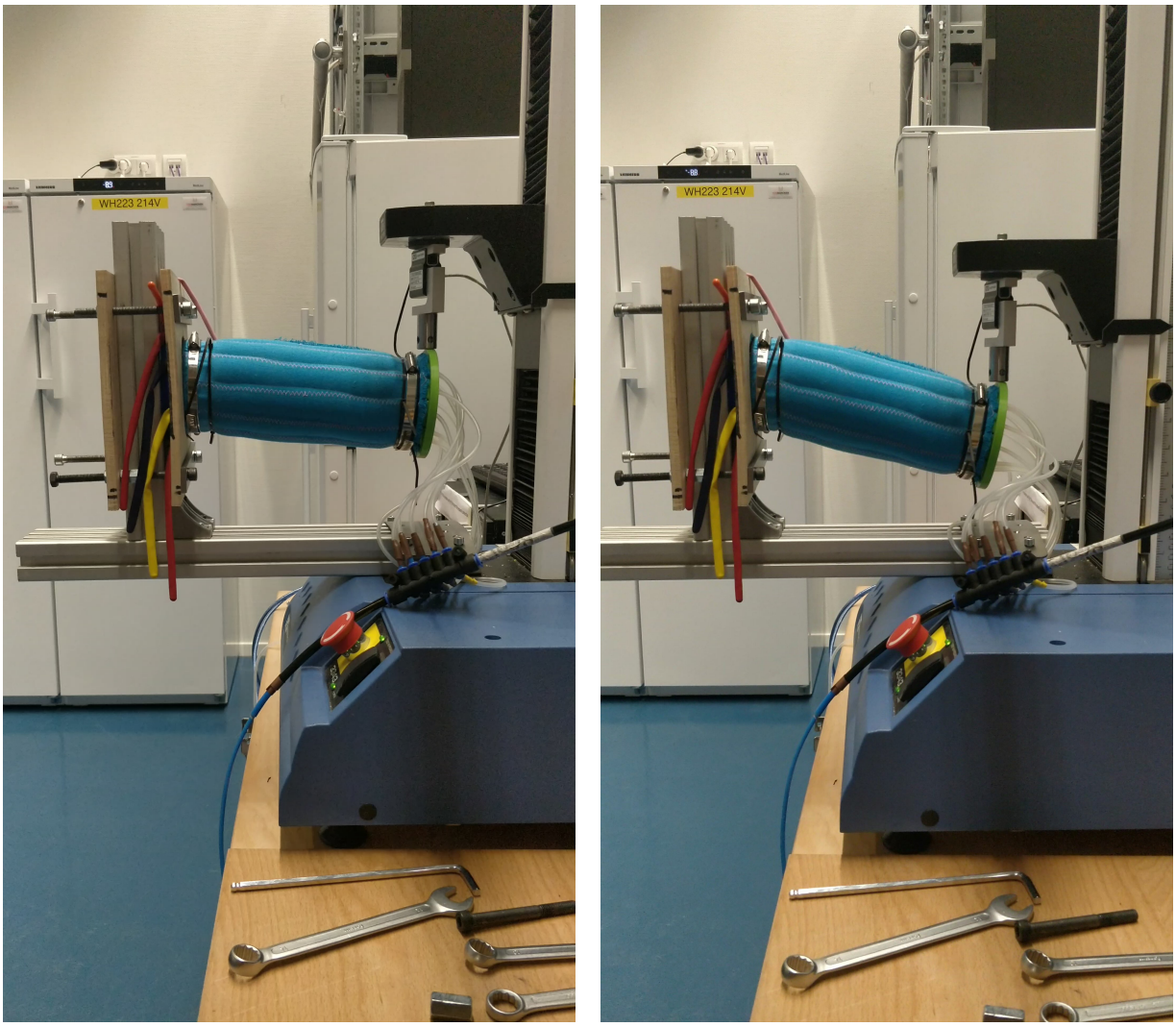

(a) Hollow prototype shortly after the start of the experiment

(b) Hollow prototype at the end of the experiment

Figure 50: Example of the shape change during the bending experiment

Similar to the results from the compression tests, the data has been extrapolated over the entire displacement range for the averaged curves. The data collection during this experiment was started when the threshold of 2 N was reached, which is why the collected data does not span all the way to 40 mm. Due to the extrapolation some uncharacteristic behaviour can be observed in the last few millimeters of displacement. For the curve of the hollow cylinder at 25 kPa in figure 37 a sudden change in slope can be observed at about 37 mm of displacement. This is caused by the extrapolation, which extrapolates the data linearly based on the slope of the last two measurement points. In the curve of the hollow cylinder at 75 kPa shown in figure 40b a sharp downwards slope can be seen in the data. This is caused by a drop in force of Test3 in the last few measurement points, which in then extrapolated over the remaining displacement range. It can be assumed that the curves would continue with the same slope over the entire displacement range if not for these few bad measurement points.
The curves depicted in figure 49 can lead to a wrong conclusion, since these graphs have not been normalized for the volume of air consumed. However, in figure 51, the volume-normalized curves can be observed, which show that the hollow cylinder outperforms the solid cylinder at all test pressures. The hollow cylinder outperforms the solid cylinder by a larger amount at the lower pressures, which could potentially be explained by the required re-installment procedure. Some of the balloons of the hollow cylinder failed at 75 kPa, which required it to be taken out of the test setup and disassembled. After the reassembling of the prototype it might have had a slightly different length, which is caused by the installment procedure of the textile sleeve onto the disks. Furthermore, the orientation of the prototype was most likely different after it was re-installed into the test setup. As was shown previously during the compressive tests, the prototypes are orientation dependent. The combination of these two effects could have had a serious impact on the results of these experiments.

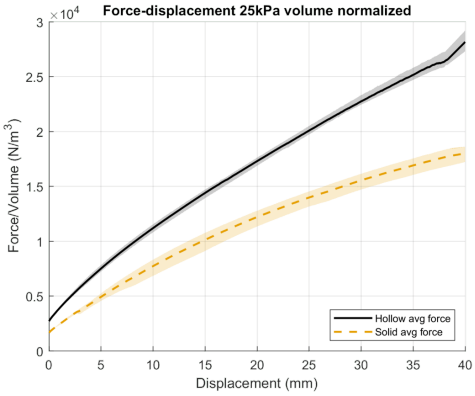

(a) Force-displacement-pressure graph of both designs at 25 kPa

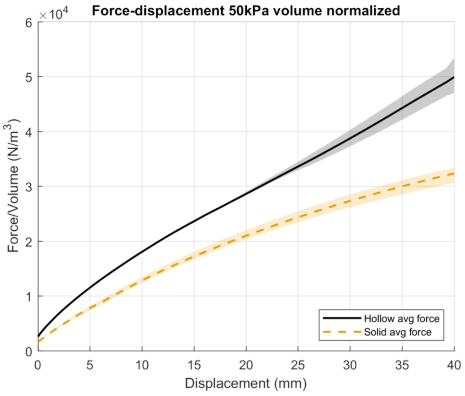

(b) Force-displacement-pressure graph of both designs at 50 kPa

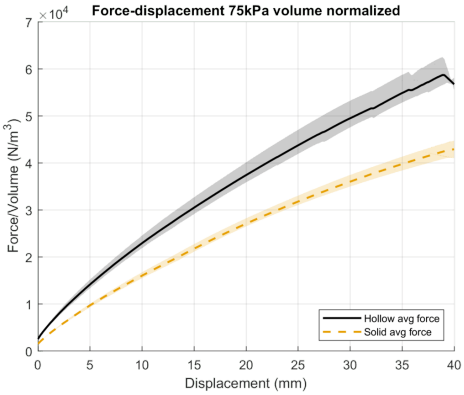

(c) Force-displacement-pressure graph of both designs at 75 kPa

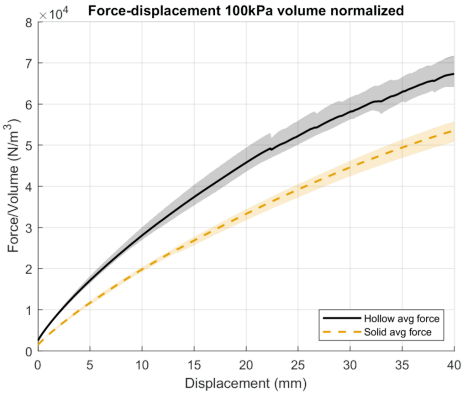

(d) Force-displacement-pressure graph of both designs at 100 kPa

Figure 51: Averaged results from bending tests volume normalized including error margins

4.4.3 Comparison of different designs

The effective strength ratio between both designs is given in table 13, where $F_{\max}$ is the ratio between the maximum force of the hollow cylinder with respect to the solid cylinder. The volume normalized strength ratio using the design ratio of 0.69, is denoted by F_{eff}. The volume normalized strength ratio is given in column F_{eff2}, while the volume ratio is given by V_{ratio}. The measured diameters of the hollow and solid cylinder can be found in columns d_{h} and d_{s}, respectively. The inner radius of the hollow cylinder was assumed to be a constant value of 25 mm, as this value could not be measured.

Table 13: Ratio's from the results of the bending tests and measured radii.

	$F_{\max}$	F_{eff}	F_{eff2}	V_{ratio}	d_{h} (m)	d_{s} (m)
25kPa	0.958	1.386	1.565	0.6124	0.0895	0.0935
50kPa	0.943	1.364	1.543	0.6111	0.0905	0.0950
75kPa	0.817	1.182	1.368	0.5969	0.0910	0.0965
100kPa	0.735	1.063	1.257	0.5849	0.0910	0.0975

Across all measured pressures for the tested prototypes, a notable improvement was observed when transitioning from a solid cylinder to a hollow cylinder design. This improvement is larger at the lower pressures compared to the higher pressures. From the theoretical model it was expected that the performance increase would be smaller as the pressure increases, but not as significantly as was observed during the experiments.
To be able to compare the results from the prototypes with the theoretical model is is important to determine

the values of all the variables. The diameter and length of the prototypes at the different pressures have been measured. An estimation for the value of ν is made, where this value is set to 0.3. In order to be able to determine the value for the Young's modulus, a tensile test was performed.
A rectangular piece of the fabric was placed in the tensile tester, which measures both the displacement and the applied force as it elongates the test sample. This test was performed on five different samples with the same dimensions. The samples had a length of 75 mm, while the width was 25 mm and the thickness 0.5 mm. A visualization of the measurement data can be found in figure 52. In this graph it can be seen that 4 out of the 5 measurements have a very similar curve, while the first performed experiment deviates quite a bit. The Young's modulus can be calculated according to

$$E = \frac{FL}{A\Delta L}, \tag{53}$$

where F is the applied force, L the initial length of the sample, A the surface area and ΔL the elongation during the experiment. To determine the Young's modulus it is important to know what forces are applied on the prototypes as the behaviour measured in the tensile test is non linear. The Young's modulus measured at low forces/elongation will be significantly different from the Young's modulus that would be measured in the middle, linear part of the graphs. It is hard to determine at what point in the graph the prototypes are situated, thus the Young's modulus is measured both at low strains in the non-linear part of the graph as well as in the higher strains up to the point of failure. The Young's modulus after the first initial non-linear behaviour will be constant, since the slope of the graph is constant in that range. When determining the Young's modulus in the low strain portion, the averaged result will exclude Test1 as this initial test has a significantly different slope from the other tests. The most likely explanation for the deviation of Test1 is that this sample was already pre-strained, since the slope is almost identical to that of the other sample in the linear region.
Applying equation 53 in the strain region from 1 mm to 2 mm results in a Young's modulus of 2.2 MPa. Calculating the Young's modulus in the linear region, results in a Young's modulus of 7.3 MPa. Both values will be considered in upcoming calculations since it is hard to determine in which region the correct Young's modulus will be located for each pressure considered. The most likely scenario is that the value of Young's modulus will be pressure dependent. An overview of the measured values can be found in the table 14 below.

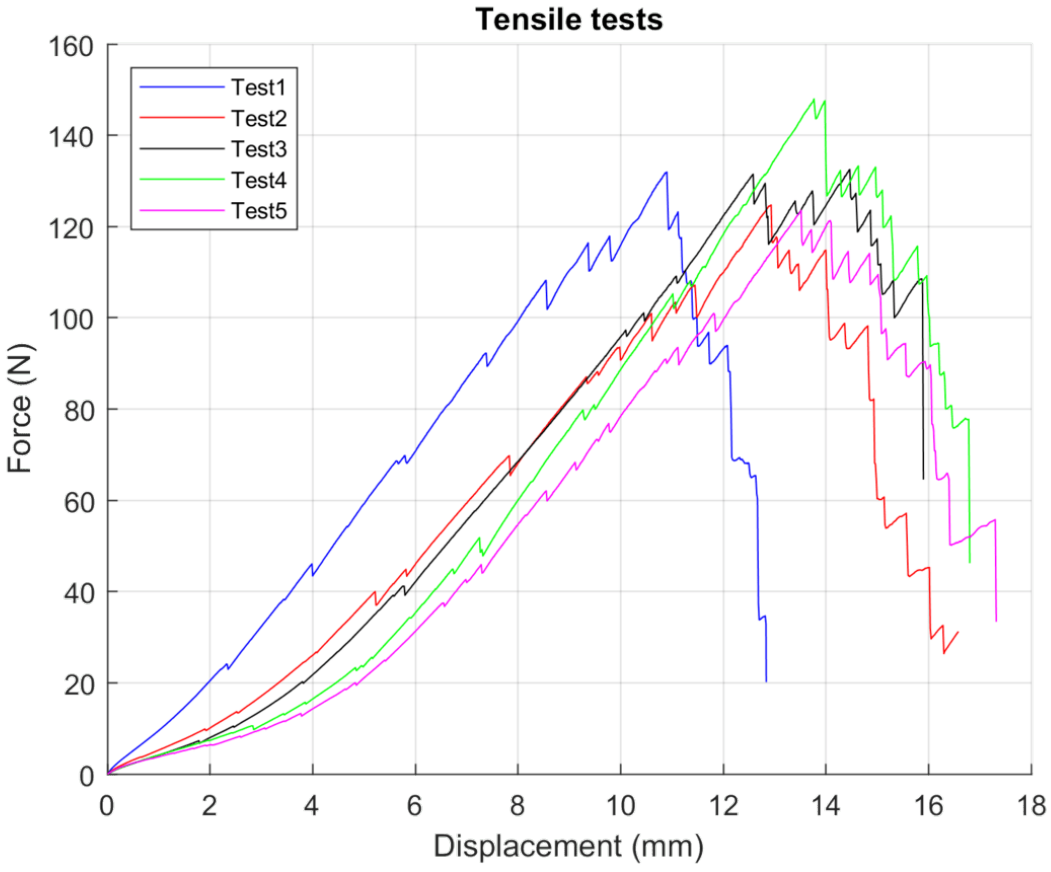

Figure 52: Force-displacement curves of tensile tests

Table 14: Geometrical properties measured

	$L_s(m)$	$L_h(m)$	$d_s(m)$	$d_h(m)$
25kPa	0.1760	0.1710	0.0935	0.0895
50kPa	0.1790	0.1735	0.0950	0.0905
75kPa	0.1820	0.1750	0.0965	0.0910
100kPa	0.1830	0.1760	0.0975	0.0910

When substituting the values above into the equations, table 15 is obtained. In this table F_{max} denotes the theoretical ratio between the maximum forces of both designs and F_{max2} the same ratio, but using a Young's modulus of 7.3 MPa instead of 2.2 MPa. Similarly, F_{eff} denotes the volume normalized ratio between the hollow and solid cylinder designs using a Young's modulus of 2.2 MPa and F_{eff2} using a Young's modulus of 7.3 MPa. At low pressures, the influence of the different Young's moduli is relatively minor, but as the pressure increases, so does the effect of the Young's modulus. When the Young's modulus is relatively large compared to the pressure, the influence of the pressure on the maximum force is limited, but when they start approaching each other in size, the effect of the pressure becomes more and more important for the maximum force. Even if the ratio between the maximum forces is not impacted much by the significantly different Young's modulus, this does not imply that the maximum force itself does not change significantly.
The effective strength ratio decreases as the pressure increases, which is in line with the results from the tested prototypes, albeit that the decrease is smaller compared to the tested prototypes. These results were obtained using the measured dimensions, Young's modulus and references values for the other variables. These values have a uncertainty to them, which results in an error margin. To create this error margin it was assumed that the measured dimensions can be off by as much as 2 mm, which is considerable, but not unrealistic, especially considering the non uniform radius of the prototypes. This effect of the non uniform radius was already diminished by measuring the radius at two different orientations and averaging it. The value for the shear modulus was assumed to be exactly correct for an isotropic material, while the value for ν was assumed to be possible in the entire range of 0 to 0.5, but this only has a very small impact on the error values. The thickness of the material was assumed to possibly be off by as much as 10 %, which only has a small impact due to the large Young's modulus with respect to the pressure. The resulting errors margins are about ±20 %, which is quite significant. However, the majority of these error margins can be attributed to uncertainties in the measurements of the radius and length. The radius, in particular, accounts for approximately half of the overall error margin.

Table 15: Theoretical ratio's between the hollow and solid cylinder design.

	F_{max}		F_{max2}		F_{eff}		F_{eff2}	
25kPa	1.059	+0.210 -0.184	1.083	+0.211 -0.186	1.730	+0.246 -0.223	1.768	+0.245 -0.231
50kPa	1.019	+0.205 -0.178	1.062	+0.206 -0.181	1.667	+0.241 -0.224	1.737	+0.240 -0.226
75kPa	0.984	+0.200 -0.173	1.043	+0.202 -0.178	1.648	+0.243 -0.224	1.748	+0.242 -0.227
100kPa	0.932	+0.193 -0.166	1.005	+0.195 -0.172	1.594	+0.241 -0.220	1.718	+0.240 -0.225

The chosen error margins result in the measurements of the prototypes to be within the margin of error at the lower pressures, but not at the higher pressures. This could be attributed to the measurement results from the hollow cylinder at 75 kPa and 100 kPa, due to aforementioned reasons. However, the results at lower pressures are also not very good, which might point to a mismatch between the theoretical model and the measurement results. One

of the possible variables that could be wrong is the inner radius, which was not measured. It is possible that the inner radius decreases as a function of the pressure as well, but this only has a very minimal impact on the results. Furthermore, a good match between the force ratios does not mean that the model fits with the measurement results. To evaluate the theoretical model in more detail, the maximum force of each design will be compared to the experimental results individually. The results of this can be found in table 16, where $_s$ denotes the results from the solid cylinder while $_h$ denotes the hollow cylinder. Number 1 represents the results with a Young's modulus of 2.2 MPa, while 2 denotes the results with a Young's modulus of 7.3 MPa. From this table it can be observed that the influence of the pressure on the required force for the displacement of 40 mm is only very minor. The effect of the pressure is relatively larger for a low Young's modulus, which is in agreement with the results of the previously performed analysis on the theoretical model. The results from the theoretical model differ significantly from the results of the performed experiments. A few explanations are possible for the observed differences.
For the hollow cylinder the inner radius could also be pressure dependent, which would result in a stronger pressure dependency of the maximum force. This would however only be applicable to the hollow cylinder, as the solid cylinder does not have an inner radius. Furthermore, this effect is only very limited and would not be able to account for the large differences observed.
A second possible explanation would be the pressure dependency of the Young's modulus. From the strain testing it was observed that the Young's modulus shows a non-linear behaviour for small strains. As can be seen from the results in table 16, the relationship between the Young's modulus and required force is quite strong. If it would be assumed that the Young's modulus would change as a function of the pressure from 2.2 MPa at 25 kPa to 7.3 MPa at 100 kPa this would change the results significantly and show a much stronger relationship between the required force and the pressure.
A third reason for the discrepancy between the theoretical and experimental results could be the fact that applied forces are too high for the model to be applicable. According to [Le van and Wielgosz, 2005] and [Nguyen et al., 2015], the results from the model are only valid if,

$$F \leq \frac{\pi R^3 p}{2L} \tag{54}$$

where R is the radius, p the internal pressure, L the length and F the transverse applied force on the beam at the tip. If this relationship is not true, the model is no longer valid since wrinkling will occur in the membrane. The critical forces for the produced prototypes are slightly lower than the force applied during the experiments at the maximum deflection of 40 mm. This could explain the slight deviation from the linear behaviour as the deflection and applied force continue to increase. It does however not account for the large difference observed between the theoretical and experimental results. Furthermore, if the maximum force was calculated slightly below this threshold value, the difference between the theoretical model and experimental results would still be significant.
One further remark that has to be made here is that the model assumes a constantly increasing deflection over the entire length, while the experiments showed a sharp bend at the clamping point of the cylinders with a constant angle over the remaining length of the cylinder. This difference could account for some of the observed differences to the point where the model might no longer be valid, but it is impossible to know the exact effects of the observed behaviour during the experiments.
Finally, in addition to the Young's modulus not being constant, the shear modulus might also not be consistent with the isotropic material approach that was used here. This could have significant effects on the force-displacement relation. Reducing the value for the shear modulus would result in a larger displacement and thus lower forces.

Table 16: Theoretical required force to reach a displacement of 40 mm for different Young's moduli

	$F_{\max_{s1}}$		$F_{\max_{h1}}$		$F_{\max_{s2}}$		$F_{\max_{h2}}$	
25kPa	63.462	+14.646 -11.588	67.216	+15.766 -12.721	200.508	+48.029 -37.664	217.127	+52.051 -41.790
50kPa	67.669	+14.797 -11.861	68.934	+15.617 -12.705	204.548	+47.807 -37.689	217.159	+51.224 -41.273
75kPa	71.884	+14.985 -12.152	70.711	+15.570 -12.757	208.668	+47.612 -37.733	217.698	+50.683 -40.963
100kPa	77.202	+15.489 -12.674	71.955	+15.489 -12.769	215.948	+48.345 -38.457	217.038	+50.006 -40.530

The results obtained from the theoretical model, using the given values, indicate a significant deviation from the experimental results. However, if it is assumed that the Young's modulus varies linearly as a function of the

pressure, with a range of 2.2 MPa at 25 kPa to 7.3 MPa at 100 kPa, it would result in a significantly improved fit between the theoretical model and the experimental data. It is assumed that the isotropic nature of the material still holds true. The results from this change can be found in table 17. The found force's are still significantly higher than the results from the experiments, however, if the Young's modulus is scaled by a constant factor a much improved fit can be achieved. Dividing the Young's modulus by a factor of 3.25, results in a linear scaled Young's modulus from 0.677 MPa at 25 kPa to 2.246 MPa at 100 kPa. The results from this can be found in columns 4, while the experimental results can be found in the columns with a 5 of table 17.

Table 17: Theoretical ratio's between the hollow and solid cylinder design with varying inner radius and improved fit

	$F_{\max_{s3}}$	$F_{\max_{h3}}$	$F_{\max_{s4}}$	$F_{\max_{h4}}$	$F_{\max_{s5}}$	$F_{\max_{h5}}$
25kPa	$63.462^{+14.646}_{-11.588}$	$67.216^{+15.766}_{-12.721}$	20.674	21.614	21.75	20.84
50kPa	$113.347^{+25.779}_{-20.458}$	$118.383^{+24.333}_{-11.466}$	37.782	38.505	41.05	38.71
75kPa	$163.145^{+36.708}_{-29.191}$	$168.760^{+34.576}_{-11.623}$	54.950	55.144	57.07	47.48
100kPa	$215.948^{+48.345}_{-38.457}$	$217.038^{+50.006}_{-40.530}$	73.142	71.066	73.23	53.82

A very good fit between the theoretical model and the experimental data is achieved for the solid cylinder. The hollow cylinder only achieves a good fit at 25 kPa and 50 kPa. At higher pressures the difference between the theoretical and experimental data increases significantly. This difference might again be attributed to the failure at 75 kPa and the subsequent re-install moment procedure.
From the theoretical model it was observed that at the given pressures and used Young's moduli, the behaviour is heavily dominated by the Young's modulus. Which results in a near linear increase of the bending stiffness if the Young's modulus is scaled linearly. This was observed for the solid cylinder design and also at the two lower pressures of the hollow cylinder design in the experimental results.
Comparing the Timoshenko beam model found in equation 26 with the model for the inflatable beam and the experimental results gives some quick insights in the accuracy of this model. If the found values for the variables are substituted into this equation, while the area is defined as the entire region that is filled with air, it overestimates the bending stiffness by a very large factor. However, if the same definitions are used as in the inflatable beam model, it approximates it quite well. This is due to the relatively low impact of the pressure in comparison to the Young's modulus. As the pressure increase and is closer to the value of the Young's modulus, the deviation between the Timoshenko beam model and the inflatable beam model becomes a lot bigger. This could be observed directly from equation 28, where the pressure terms can be interpreted as an addition to the material properties. As the pressure increases, so do the equivalent material properties, which means that for low pressures the Timoshenko beam model results in a good approximation, while at higher pressures this is no longer the case.

5 Conclusion

In this research, a novel geometric design was proposed with the objective of achieving a higher force-to-volume ratio for a soft pneumatic actuator. Existing soft pneumatic actuators utilize an inflatable pouch made of an airtight material in combination with a strain limiting layer. In the newly proposed design, the solid cylinder is replaced by a hollow cylinder. It is hypothesized that the soft actuator will be able to achieve similar levels of output force as the original soft pneumatic actuator, while consuming a significantly reduced amount of air to reach inflation. The reduced air consumption should lead to faster inflation times or for a less powerful and bulky air supply to be used, which could lead to a fully untethered soft pneumatic actuator.

The volume reduction of the inflatable actuator results in an improved inflation time equal to the volume reduction, which was about 68 % the time of the solid cylinder design. As the pressure increases the achieved improvement in inflation time decreases in both absolute and relative terms, but still significant improvements are observed. To reach a pressure of 75 kPa, 90.3 % of the time is used.

The results obtained from the compression tests conducted on the prototypes were consistent with the theoretical calculations. A near perfect ratio of 1 was achieved after the theoretical model was slightly adapted to better fit the results. Both designs have a similar amount of force generated per unit air consumed. Due to the low slenderness ratio of the produced prototypes, the dominant behaviour observed during the axial compression tests was compressive failure.

The different iterations of the prototype exhibited significant variations in the results, whereas the tests conducted on the same prototype demonstrated lower variations but revealed an orientation dependency. When the prototype was moved and rotated between subsequent tests performed at the same pressure, the results showed larger variation compared to test where this was not done. The observed difference in the experimental results was as much as 10 %.

Furthermore, the first test performed on the solid cylinder at each pressure, generally achieved a higher displacement before failing. A possible explanation for this behaviour is the relaxation of the fabric, which increases the volume of the cylinder. A larger starting volume would have a slightly less steep pressure increase, which means it needs a larger displacement to achieve the same force output. The relatively high variation between the different produced prototypes shows that small fabrication differences can have a large influence on the behaviour of the soft pneumatic actuator.

The low variance observed between the results of the tests performed on the same prototype shows the consistency between different inflation cycles. The strong agreement between the theoretical and measured values indicates the logical nature of the test results. By making small adjustments to the theoretical model, it was possible to achieve a highly accurate fit between the measurement data and the theoretical predictions. The difference between the theoretical and measured maximum force is within 3 % for both iterations of the prototype at all measured pressures. A few tests resulted in larger errors, which can be attributed to measurement variations.

The results from the compressive tests are not as good as was initially hypothesized when the research was started. The produced prototypes showed no improvement compared to the original solid cylinder design, while having additional downsides. The hollow cylinder requires more material, a higher effort to be produced, has a higher stiffness in the deflated state and has a larger footprint to be able to output the same force. It is hypothesized that if the produced prototype design is long and slender an improvement can be found compared to the solid cylinder design, because buckling behaviour will become dominant, rather than compressive strength.

The prototypes are also evaluated for their bending behaviour. It is hypothesized that the hollow cylinder has a significantly higher bending stiffness compared to the solid cylinder design per unit air consumed. This hypothesis is supported by theoretical calculations performed using both the Timoshenko beam model and the inflatable beam model. The Timoshenko beam model is not applicable for membrane structures and the inflatable beam model should be used instead. Both the theoretical and experimental results show an increased bending stiffness per unit volume air consumed for the newly proposed design at all tested pressures. The observed increase was as much as 1.565 at 25 kPa for the experimental results and $1.768\ ^{+0.245}_{-0.231}$ at 25 kPa with a Young's modulus of 7.3 MPa and the same dimensions as the prototype for the theoretical model. Both the model and experimental results show a decrease in the effective bending stiffness of the hollow cylinder with respect to the solid cylinder as the pressure increases. From the experimental results this observed behaviour was much more significant at 75 kPa and 100 kPa, where the improvement went from 1.565 at 25 kPa to 1.257 at 100 kPa. This much more significant drop in effectiveness can most likely be attributed to the performed tests rather than the underlying physics, but this will require further research.

As was already observed in previous research by [Le van and Wielgosz, 2005] and [Nguyen et al., 2015], the fit between the used theoretical model and the results is quite good. In the previous research the theoretical model was compared to a finite element analysis of the same inflatable cylinder, while in this paper the model was compared to experimental results. The experimental results showed a near linear increase of the bending stiffness as

a function of the pressure. This same behaviour was not observed from the theoretical model. The difference can most likely be attributed to the pressure dependency of the Young's and shear modulus of the strain limiting material. If this pressure dependency is included in the theoretical model, a relatively good fit can be achieved with the experimental results. The measured Young's modulus has to be divided by a factor of 3.25 to achieve a very good fit with the experimental results. There is no direct explanation for this difference and further investigation of the Young's and shear modulus should be performed.
A good fit with the experimental data is only achieved for the solid cylinder. The hollow cylinder only achieves a good fit with the experimental results at 25 kPa and 50 kPa. The most likely explanation for the mismatch between the model and the experimental results is the failure of the prototype during the experiments at 75 kPa. As a result of the prototype's failure, the test setup had to be taken apart and the prototype had to be repaired. During the repairs and re-installation onto the solid disks, small changes might have been introduced. Additionally, the prototype showed orientation dependent behaviour which most likely has been introduced into the results as well when the prototype was installed into the test setup again.
The main drawbacks of the proposed design are the higher stiffness in deflated state, more complicated design and the lower output force, especially at higher pressures. The newly proposed design requires a larger amount of space to be able to output the same force, which can be limiting in certain applications. The higher initial stiffness can lead to larger interference with the user in the deflated state, which is not desired. Furthermore, the more complex design of the soft actuator requires larger amounts of material and longer production times. The downsides are only minor in comparison to the potential upsides and are highly dependent on exact application.
Across the entire range of tested pressures, both the experimental and theoretical results demonstrated an improved performance per unit volume air consumed for the newly proposed design. Combining the new and improved design with other state of the art design improvements, as suggested in [Sridar et al., 2020], can increase the efficiency of the soft pneumatic actuator even further, which could potentially lead to a fully untethered soft pneumatic actuator that can be used in day to day applications.

6 Recommendations

The main goal of this thesis was to try and improve the design of current soft inflatable actuators to achieve a higher force to air consumption ratio. The proposed design change shows promising results, but does require further research and optimization to be applied in a working solution. To help achieve this goal a number of recommendations will be made that should be considered in future work.

- The currently developed prototypes utilize a textile layer in combination with balloons to establish an airtight seal. This design could easily be improved upon by using a different fabrication technique. One potential improvement involves impregnating the interior of the textile sleeve with an airtight material, eliminating the need for balloons. This modification would not only result in more consistent behavior, which is crucial for dynamic applications, but it would also result in a more robust design which is likely to function at higher pressures without failure. While the operational pressures must adhere to relevant standards and regulations, the risk of failure would shift from the balloon bursting to failure of the textile sleeve material. In a prototyping process using a method like this might prove difficult, but when moving to large scale production it should be relatively straight forward to implement.

- The chosen textile material was selected for its strength and thickness, which facilitates easier fabrication while ensuring that any failure occurs in the air bladders rather than the textile sleeve. When implementing the proposed design change in a specific application, it is important to carefully select a suitable material. In general, it is advisable to choose a textile material that possesses sufficient strength to avoid failure while maintaining a low stiffness in the deflated state. This way the impact on the user is minimal in the deflated state.

- The created prototypes both have solid disks on their tops and bottoms, which might not be ideal in an application. A few different solutions are possible to replace the solid disks with a soft solution. A possible solution for this would be to sew them closed. This can be done in two different ways, where the first option would be to sew the top and bottom closed, but leaving small holes to have room for the air supply tubes. The other option would be to fully close it using sewing and making a hole for the air supply on the faces of the chambers. Both these solutions are basically the same, with the difference being the location of the air supply tubes.

- In the newly proposed hollow cylinder design, each chamber is equipped with its own air supply tube and air bladder. Assuming a solution similar to the first recommendation is used, where the textile is impregnated with an airtight material, a single air supply tube can be used instead. In the currently proposed design each of the chambers is fully closed, but with the impregnated fabric it would be possible to have holes in the inner walls of the cylinder. This would allow for each of the chambers to be interconnected and be inflated from a single inflation point. If very fast inflation time are required having a single inflation point might not be ideal, however, multiple inflation points can be implemented using the same solution as well. A solution like this would reduce the complexity of the design, but would require further research to determine possible flow rate bottlenecks.

- The produced hollow prototypes all had 10 chambers, which was chosen for ease of production. For future designs and research it might be interesting to investigate the influence of the number of chambers and the size of the chambers. The produced prototypes showed non axi-symmetric behaviour which was most likely caused by small production errors. Decreasing the number of chambers might create a more symmetric behaviour, which is beneficial for a number of reasons. A symmetric design should perform better and the control algorithm would also have to be less sophisticated.

- The mismatch between the theoretical model and the experimental results for the bending tests should be investigated further. In this research the data for the bending tests was only collected on a single iteration of each prototype. As was noticed during the experiments for the hollow cylinder design a small change can significantly impact the results. In contrast to previously performed research, the difference between the results from these experiments with the theoretical model is quite large, both for the hollow and solid cylinder design. To investigate if the model can accurately predict the results from design changes, further experiments will be required, preferably on multiple prototypes to limit the error.

- To achieve a good fit between the theoretical model and the experimental results it was required to linearly scale the Young's modulus as a function of the pressure and also apply a multiplication factor to the measured Young's modulus. To investigate if the model can describe the bending behaviour of the inflatable prototypes more research will have to be performed on the Young's modulus of the textile strain limiting material used.

The Young's modulus is the most likely cause of the mismatch between the results of the model and the experimental tests, considering previous research did show a good match between the theoretical model and a finite element model.

- The experiments performed on the prototypes had a different bending shape compared to the theoretical model. In the theoretical model the bending happens over the entire length of the beam, whereas in the experiments a sharp bend occurred right at the start. After the initial sharp bend, the prototype remained straight over the entire length, which could also be a possible explanation for the differences between the theoretical model and the experimental results. Further prototypes should be created and investigated for their bending shape using different strain limiting materials to confirm the validity of the theoretical model.

References

[Acome et al., 2018] Acome, E., Mitchell, S. K., Morrissey, T. G., Emmett, M. B., Benjamin, C., King, M., Radakovitz, M., and Keplinger, C. (2018). Hydraulically amplified self-healing electrostatic actuators with muscle-like performance. *Science*, 359(6371):61–65.

[Alici, 2018] Alici, G. (2018). Softer is harder: What differentiates soft robotics from hard robotics? *MRS Advances*, 3:1–12.

[Barnett et al., 1993] Barnett, S. L., Bagley, A. M., and Skinner, H. B. (1993). Ankle weight effect on gait: Orthotic implications. *Orthopedics*, 16(10):1127–1131.

[Bartlett et al., 2015] Bartlett, N. W., Tolley, M. T., Overvelde, J. T. B., Weaver, J. C., Mosadegh, B., Bertoldi, K., Whitesides, G. M., and Wood, R. J. (2015). A 3d-printed, functionally graded soft robot powered by combustion. *Science*, 349(6244):161–165.

[Bechet and Ohnishi, 2014] Bechet, F. and Ohnishi, K. (2014). Electro-hydraulic force transmission for rehabilitation exoskeleton robot. In *2014 IEEE 13th International Workshop on Advanced Motion Control (AMC)*, pages 260–265.

[Caldwell et al., 1994] Caldwell, D. G., Medrano-Cerda, G. A., and Goodwin, M. (1994). Characteristics and adaptive control of pneumatic muscle actuators for a robotic elbow. In *Proceedings of the 1994 IEEE International Conference on Robotics and Automation*, volume 4, pages 3558–3563.

[Daerden, 1999] Daerden, F. (1999). Conception and realization of pleated pneumatic artificial muscles and their use as compliant actuation elements. *Vrije Universiteit Brussel*, page 176.

[Decker, 2015] Decker, M. (2015). Soft robotics and emergent materials in architecture. *Proceedings of the 33rd eCAADe Conference*, 2:409–416.

[El-Atab et al., 2020] El-Atab, N., Mishra, R. B., Al-Modaf, F., Joharji, L., Alsharif, A. A., Alamoudi, H., Diaz, M., Qaiser, N., and Hussain, M. M. (2020). Soft actuators for soft robotic applications: A review. *Advanced Intelligent Systems*, 2(10):2000128.

[Farris et al., 2014] Farris, R. J., Quintero, H. A., Murray, S. A., Ha, K. H., Hartigan, C., and Goldfarb, M. (2014). A preliminary assessment of legged mobility provided by a lower limb exoskeleton for persons with paraplegia. *IEEE Transactions on Neural Systems and Rehabilitation Engineering*, 22(3):482–490.

[Gao et al., 2023] Gao, W., Di Lallo, A., and Su, H. (2023). A portable powered soft exoskeleton for shoulder assistance during functional movements: Design and evaluation. unpublished.

[Hibbeler, 2014] Hibbeler, R. C. (2014). *Chapter 13, Buckling of Columns*, page 667–671. Pearson Education.

[Hutchinson, 2000] Hutchinson, J. R. (2000). Shear Coefficients for Timoshenko Beam Theory. *Journal of Applied Mechanics*, 68(1):87–92.

[Kellaris et al., 2018] Kellaris, N., Venkata, V. G., Smith, G. M., Mitchell, S. K., and Keplinger, C. (2018). Peano-hasel actuators: Muscle-mimetic, electrohydraulic transducers that linearly contract on activation. *Science Robotics*, 3(14):eaar3276.

[Le van and Wielgosz, 2005] Le van, A. and Wielgosz, C. (2005). Bending and buckling of inflatable beams: Some new theoretical results. *Thin-Walled Structures*, 43(8):1166–1187.

[Le van and Wielgosz, 2006] Le van, A. and Wielgosz, C. (2006). Erratum to: "bending and buckling of inflatable beams: Some new theoretical results": [thin-wall. struct. 43 (2005) 1166–1187]. *Thin-Walled Structures*, 44(7):822–823.

[Loepfe et al., 2015] Loepfe, M., Schumacher, C. M., Lustenberger, U. B., and Stark, W. J. (2015). An untethered, jumping roly-poly soft robot driven by combustion. *Soft Robotics*, 2(1):33–41.

[Malcolm et al., 2013] Malcolm, P., Derave, W., Galle, S., and De Clercq, D. (2013). A simple exoskeleton that assists plantarflexion can reduce the metabolic cost of human walking. *PLOS ONE*, 8(2):1–7.

[Mooney et al., 2014] Mooney, L. M., Rouse, E. J., and Herr, H. M. (2014). Autonomous exoskeleton reduces metabolic cost of human walking during load carriage. *Journal of NeuroEngineering and Rehabilitatio*, 11(80).

[Natividad et al., 2017] Natividad, R. F., Rosario, M. R. D., Chen, P. C. Y., and Yeow, C.-H. (2017). A hybrid plastic-fabric soft bending actuator with reconfigurable bending profiles. *2017 IEEE International Conference on Robotics and Automation (ICRA)*, pages 6700–6705.

[Nguyen et al., 2015] Nguyen, Q.-T., Thomas, J.-C., and Le van, A. (2015). Inflation and bending of an orthotropic inflatable beam. *Thin-Walled Structures*, 88:129–144.

[Pehlivan et al., 2013] Pehlivan, A. U., Rose, C., and O'Malley, M. K. (2013). System characterization of ricewrist-s: A forearm-wrist exoskeleton for upper extremity rehabilitation. In *2013 IEEE 13th International Conference on Rehabilitation Robotics (ICORR)*, pages 1–6.

[Pons, 2008] Pons, J. L. (2008). *Wearable Robots: Biomechatronic Exoskeletons*. Wiley.

[Rich et al., 2018] Rich, S. I., Wood, R. J., and Majidi, C. (2018). Untethered soft robotics. *Nature Electronics*, 1(2):102–112.

[Sanjuan et al., 2020] Sanjuan, J. D., Castillo, A. D., Padilla, M. A., Quintero, M. C., Gutierrez, E. E., Sampayo, I. P., Hernandez, J. R., and Rahman, M. H. (2020). Cable driven exoskeleton for upper-limb rehabilitation: A design review. *Robotics and Autonomous Systems*, 126:103445.

[Shepherd et al., 2013] Shepherd, R. F., Stokes, A. A., Freake, J., Barber, J., Snyder, P. W., Mazzeo, A. D., Cademartiri, L., Morin, S. A., and Whitesides, G. M. (2013). Using explosions to power a soft robot. *Angewandte Chemie International Edition*, 52(10):2892–2896.

[Skorina et al., 2018] Skorina, E. H., Luo, M., Oo, W. Y., Tao, W., Chen, F., Youssefian, S., Rahbar, N., and Onal, C. D. (2018). Reverse pneumatic artificial muscles (rpams): Modeling, integration, and control. *PLOS ONE*, 13(10):1–24.

[Sovero et al., 2017] Sovero, S. E., Talele, N., Smith, C. S., Cox, N., Swift, T., and Byl, K. (2017). Initial data and theory for a high specific-power ankle exoskeleton device. In *2016 International Symposium on Experimental Robotics*, pages 355–364, Cham. Springer International Publishing.

[Sridar et al., 2017] Sridar, S., Nguyen, P. H., Zhu, M., Lam, Q. P., and Polygerinos, P. (2017). Development of a soft-inflatable exosuit for knee rehabilitation. In *2017 IEEE/RSJ International Conference on Intelligent Robots and Systems (IROS)*, pages 3722–3727.

[Sridar et al., 2020] Sridar, S., Poddar, S., Tong, Y., Polygerinos, P., and Zhang, W. (2020). Towards untethered soft pneumatic exosuits using low-volume inflatable actuator composites and a portable pneumatic source. *IEEE Robotics and Automation Letters*, 5(3):4062–4069.

[Stephen, 1980] Stephen, N. (1980). Timoshenko's shear coefficient from a beam subjected to gravity loading. *Journal of Applied Mechanics-transactions of The Asme - J APPL MECH*, 47.

[Sup et al., 2009] Sup, F., Atakan Varol, H., Mitchell, J., Withrow, T. J., and Goldfarb, M. (2009). Preliminary evaluations of a self-contained anthropomorphic transfemoral prosthesis. *IEEE/ASME Transactions on Mechatronics*, 14(6):667–676.

[Sárosi and György, 2015] Sárosi, J. and György, L. (2015). Comparison of static force exerted by fluidic muscle and shadow air muscle. *Analecta Technica Szegedinensia*, 9(2):15–19.

[Talaty et al., 2013] Talaty, M., Esquenazi, A., and Briceño, J. E. (2013). Differentiating ability in users of the rewalk¡sup¿tm¡/sup¿ powered exoskeleton: An analysis of walking kinematics. In *2013 IEEE 13th International Conference on Rehabilitation Robotics (ICORR)*, pages 1–5.

[Thalman et al., 2020] Thalman, C. M., Hertzell, T., and Lee, H. (2020). Toward a soft robotic ankle-foot orthosis (sr-afo) exosuit for human locomotion: Preliminary results in late stance plantarflexion assistance. In *2020 3rd IEEE International Conference on Soft Robotics (RoboSoft)*, pages 801–807.

[Thalman et al., 2019] Thalman, C. M., Hsu, J., Snyder, L., and Polygerinos, P. (2019). Design of a soft ankle-foot orthosis exosuit for foot drop assistance. In *2019 International Conference on Robotics and Automation (ICRA)*, pages 8436–8442.

[Xavier et al., 2022] Xavier, M. S., Tawk, C. D., Zolfagharian, A., Pinskier, J., Howard, D., Young, T., Lai, J., Harrison, S. M., Yong, Y. K., Bodaghi, M., and Fleming, A. J. (2022). Soft pneumatic actuators: A review of design, fabrication, modeling, sensing, control and applications. *IEEE Access*, 10:59442–59485.

A Solidworks files

A.1 Closing disks hollow cylinder

The file for the Solidworks model of the hollow cylinder disk without the holes can be downloaded here or by going to this link: `https://drive.google.com/uc?export=download&id=1YfIhmyZGToq3lOqg-JtlBHo6b97AWy51`. The Solidworks file of the hollow cylinder disk with the air supply holes can be downloaded here or by going to this link: `https://drive.google.com/uc?export=download&id=1n-Wa3b0ki8MCJcN1q2LowQXX_eucB77p`.

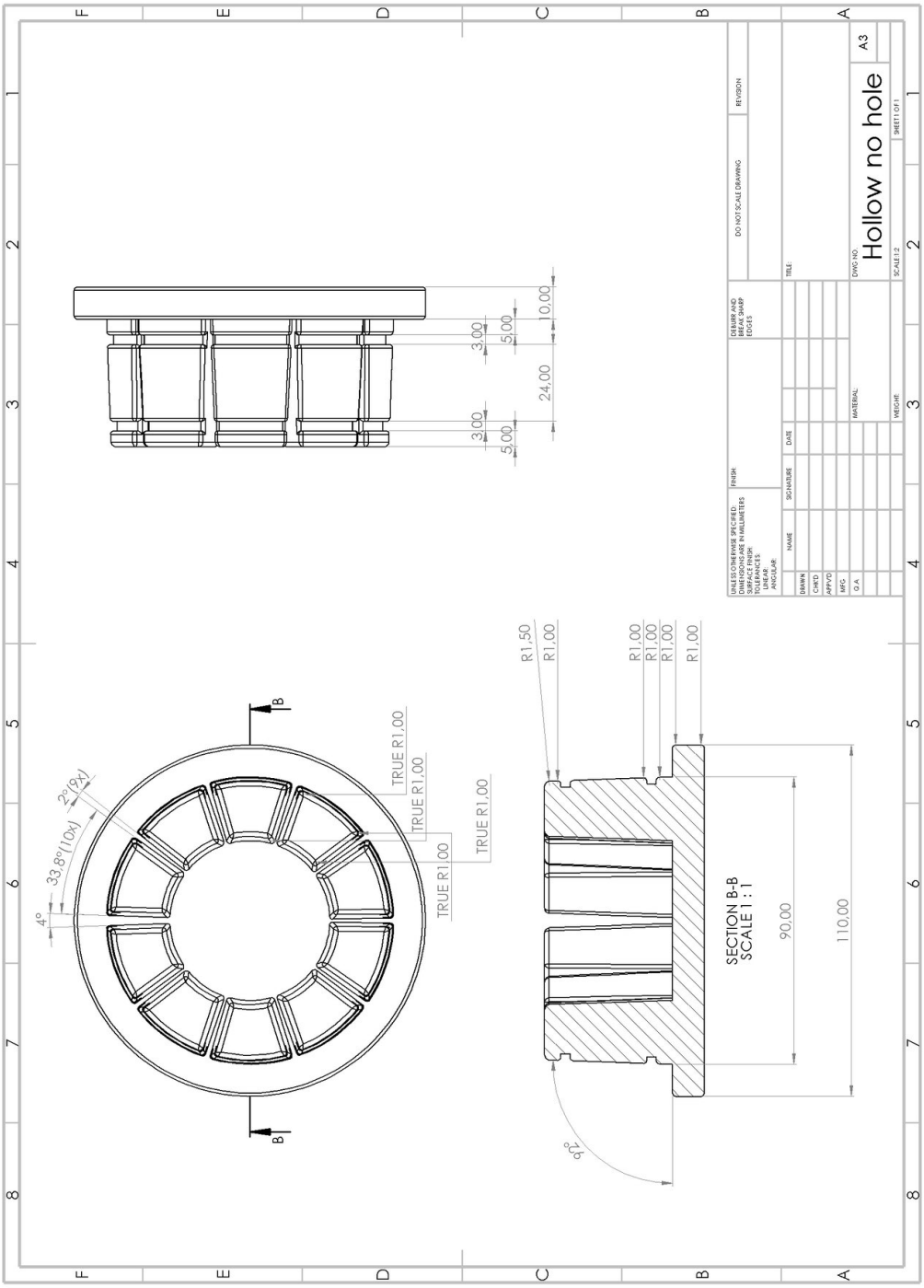

Figure A.1: Solidworks drawing of the closing disk for the hollow cylinder, with no air supply hole

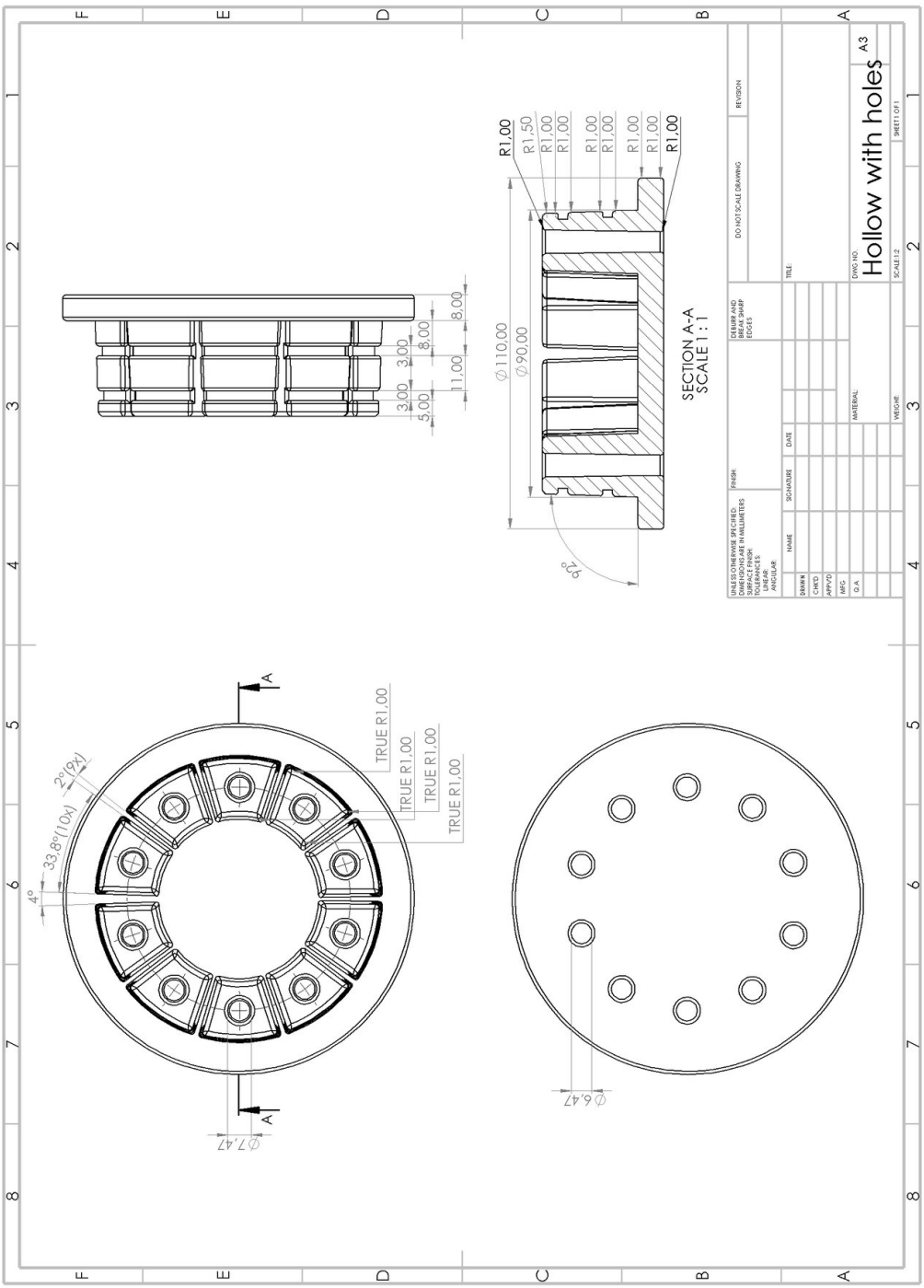

Figure A.2: Solidworks drawing of the closing disk for the hollow cylinder, with air supply holes

A.2 Closing disks solid cylinder

The file for the Solidworks model of the solid cylinder disk without the hole can be downloaded here or by going to this link: `https://drive.google.com/uc?export=download&id=1gx1CroJ5O2oe2-vMAiDw-etIhSy5kzZm`. The Solidworks file of the solid cylinder disk with the air supply hole can be downloaded here or by going to this link: `https://drive.google.com/uc?export=download&id=1fDYanFbcvXa6HEb6W-0O0mWM97igG3Lr`.

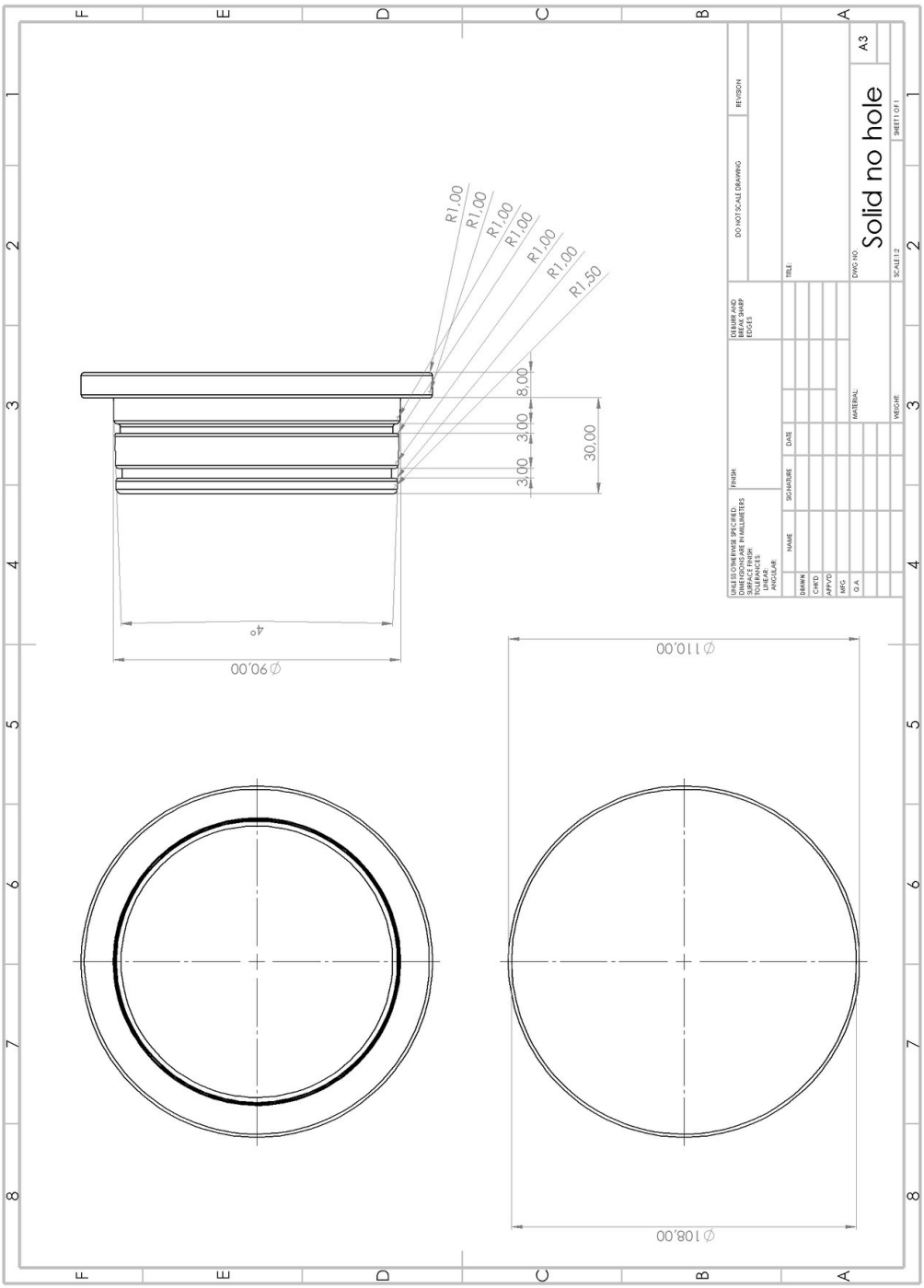

Figure A.3: Solidworks drawing of the closing disk for the solid cylinder, with no air supply hole

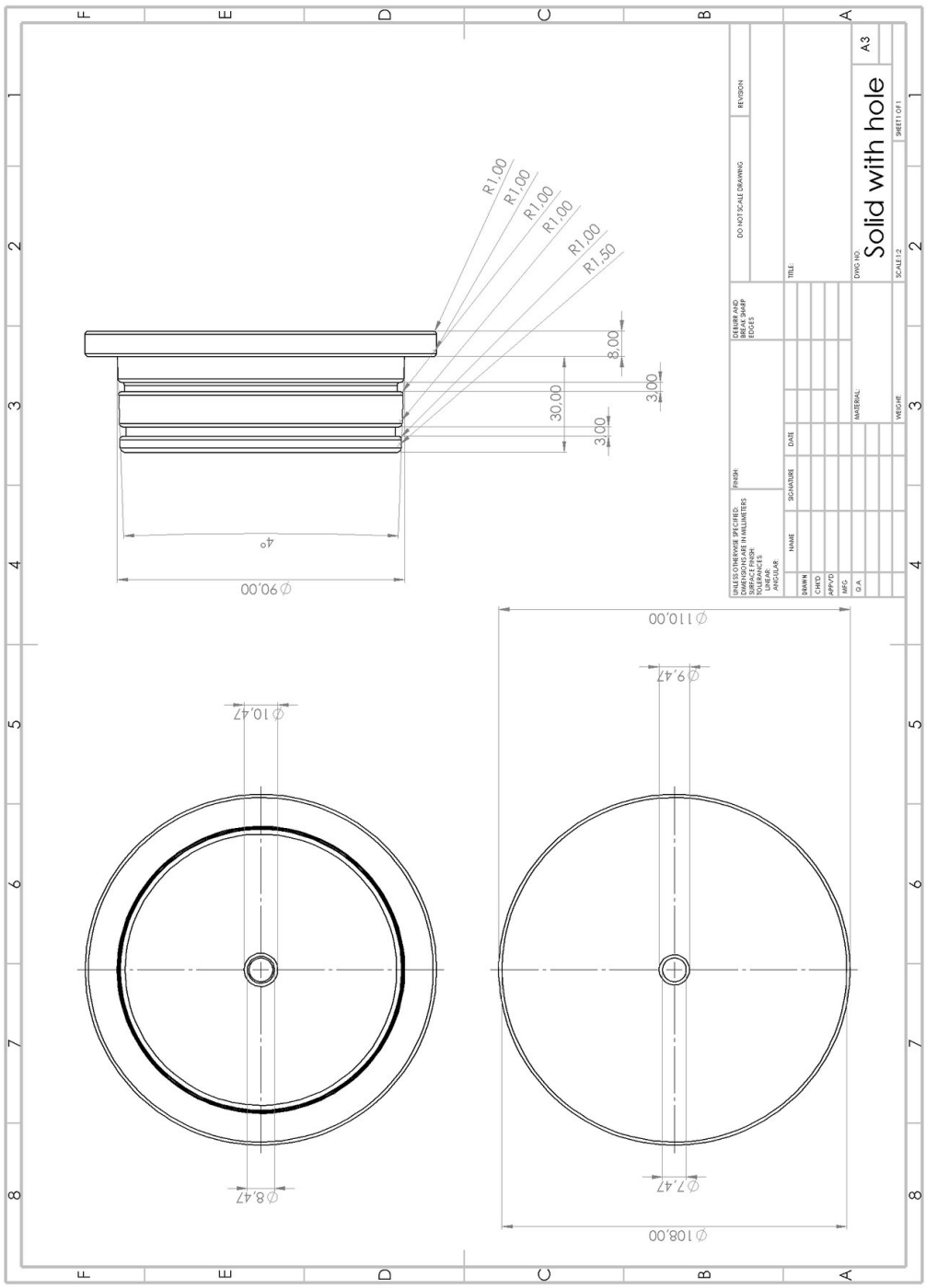

Figure A.4: Solidworks drawing of the closing disk for the solid cylinder, with the air supply hole

A.3 Custom clamps solid cylinder

The file for the Solidworks model of the solid cylinder clamp with the nut side can be downloaded here or by going to this link: `https://drive.google.com/uc?export=download&id=1cjNoSV0fK9tNZXKC4zmFRsYSR3Iroox3`. The file of the head side can be downloaded here or using this link: `https://drive.google.com/uc?export=download&id=1LJ3WNZ0AvMp3pbYCu3GtM_pTjTvcj9E2`

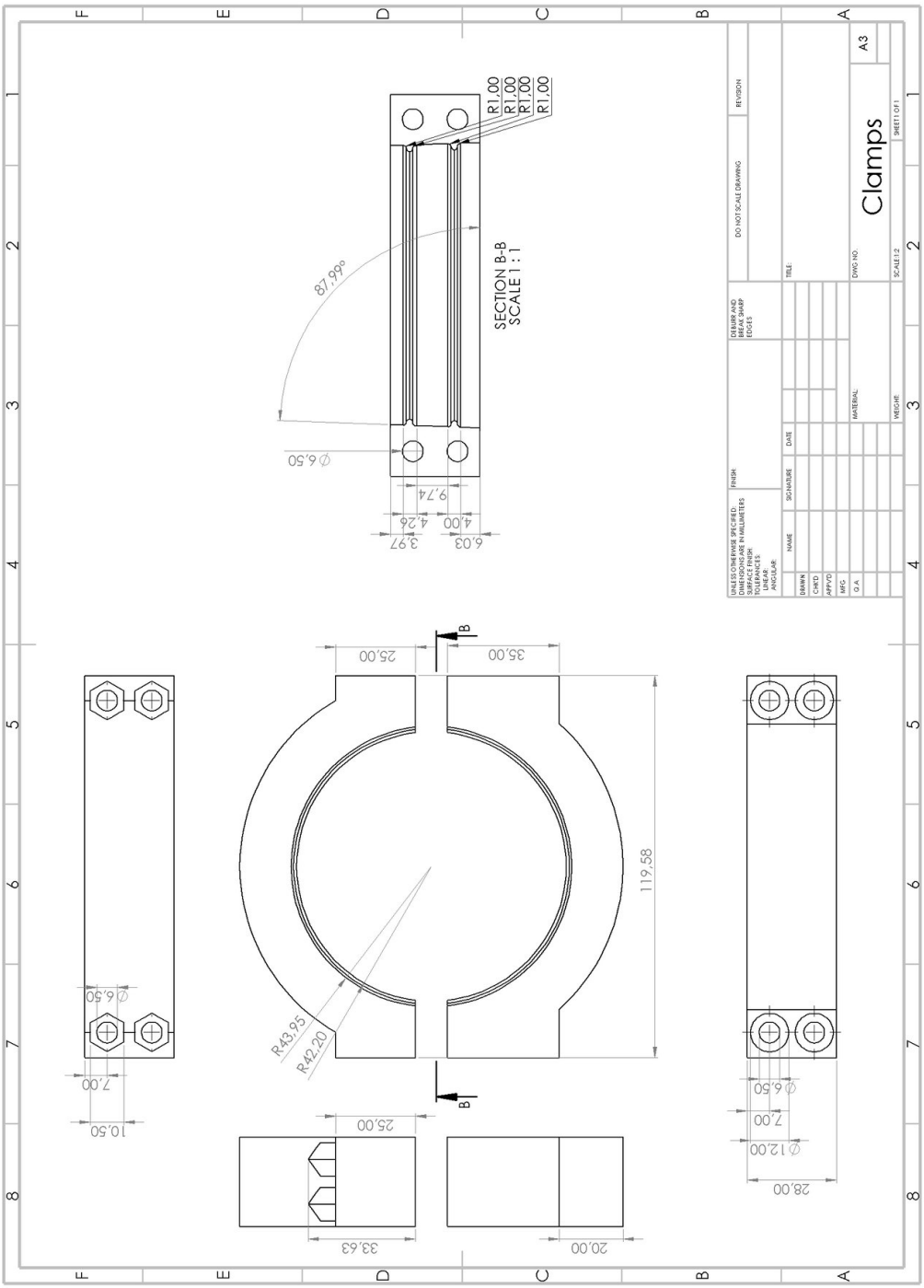

Figure A.5: Solidworks drawing of the custom clamps for the solid cylinder

B Compression tests all results

In all of the following figures, Test1, Test2 and Test3 belong to the first iteration prototype and Test4, Test5 and Test6 belong to the second iteration of the same prototype. The exceptions to this are the results from the solid cylinder at 100 kPa, where the Test4, Test5 and Test6 belong to the third iteration solid cylinder prototype instead of the second iteration, due to failure.

B.1 Force-displacement results

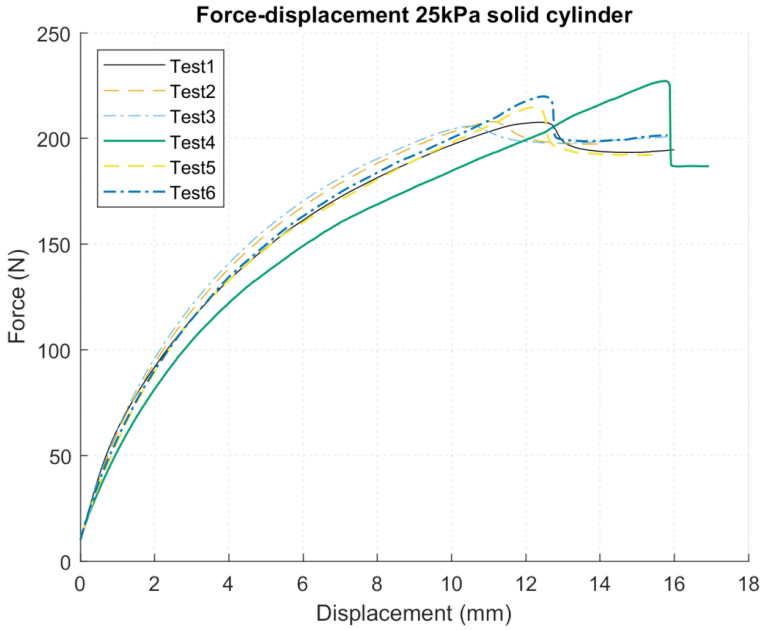

Figure B.1: Force-displacement curve for the solid cylinder at 25 kPa

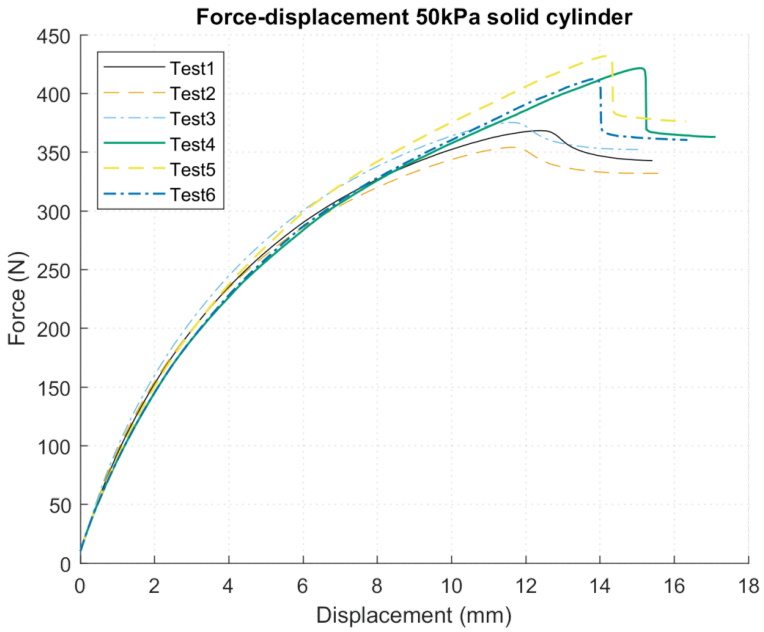

Figure B.2: Force-displacement curve for the solid cylinder at 50 kPa

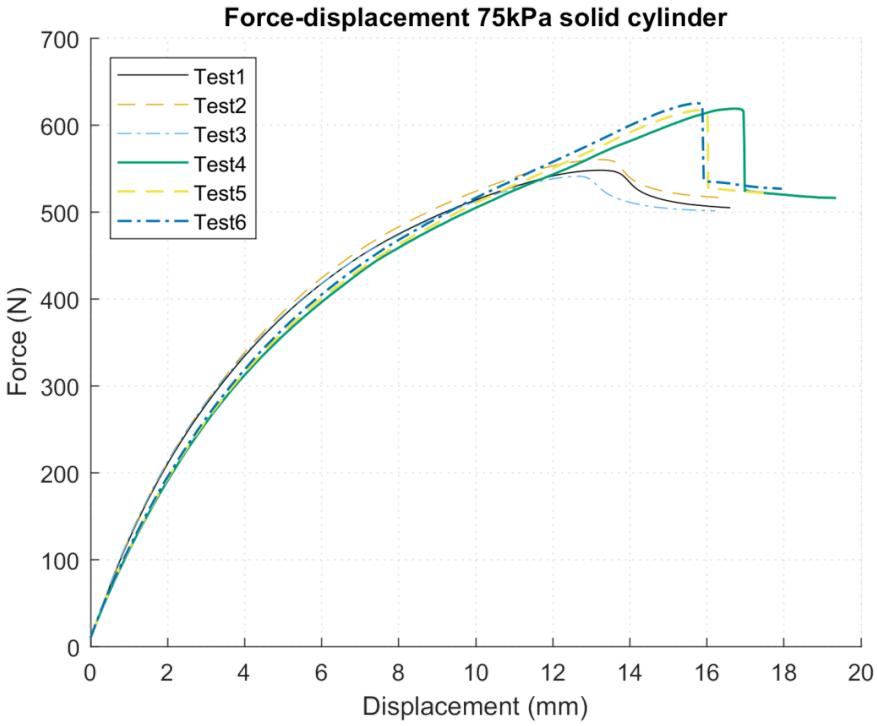

Figure B.3: Force-displacement curve for the solid cylinder at 75 kPa

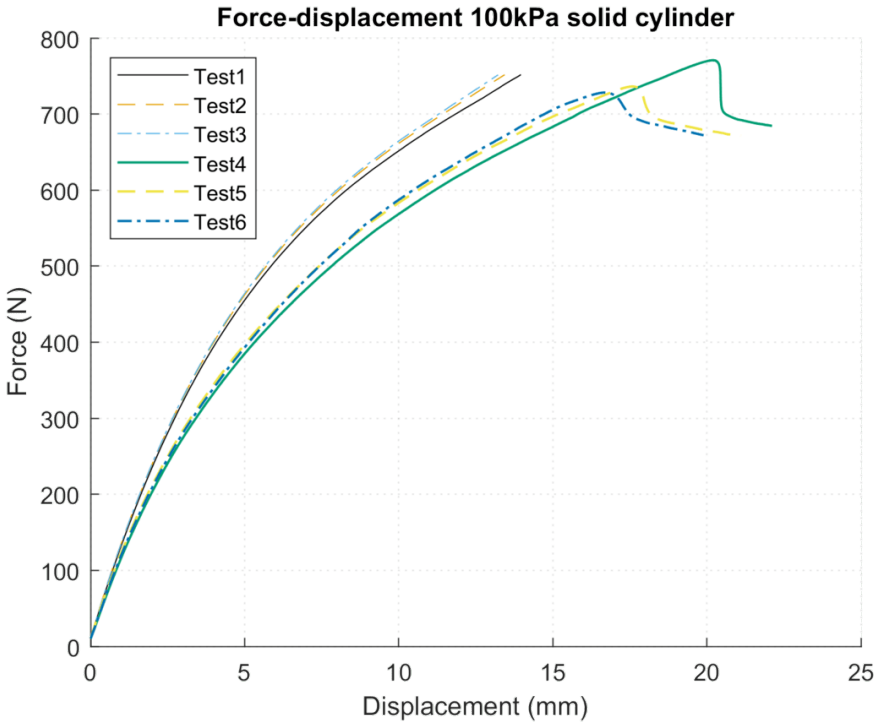

Figure B.4: Force-displacement curve for the solid cylinder at 100 kPa

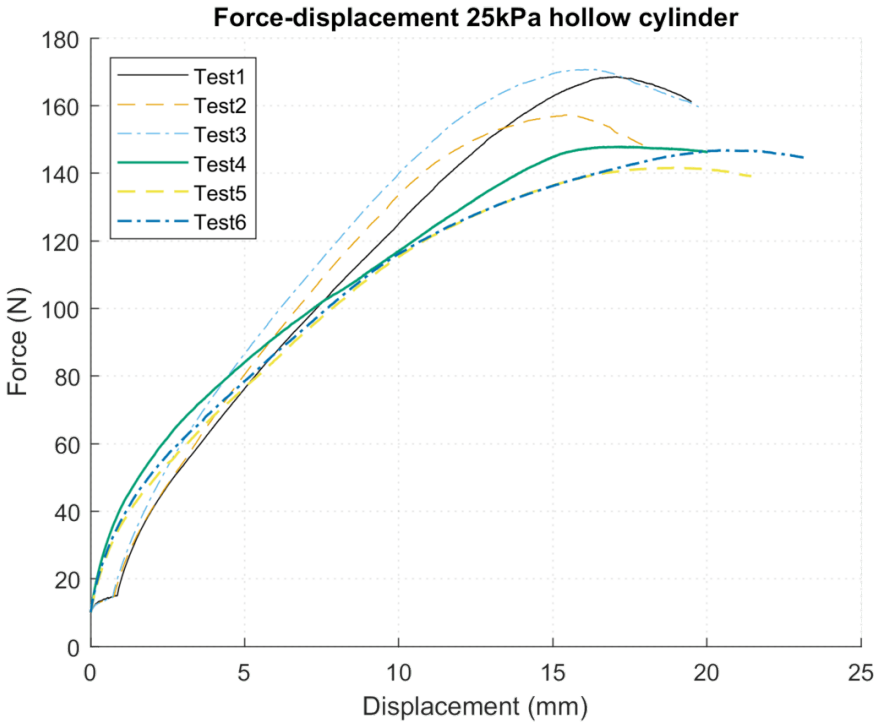

Figure B.5: Force-displacement curve for the hollow cylinder at 25 kPa

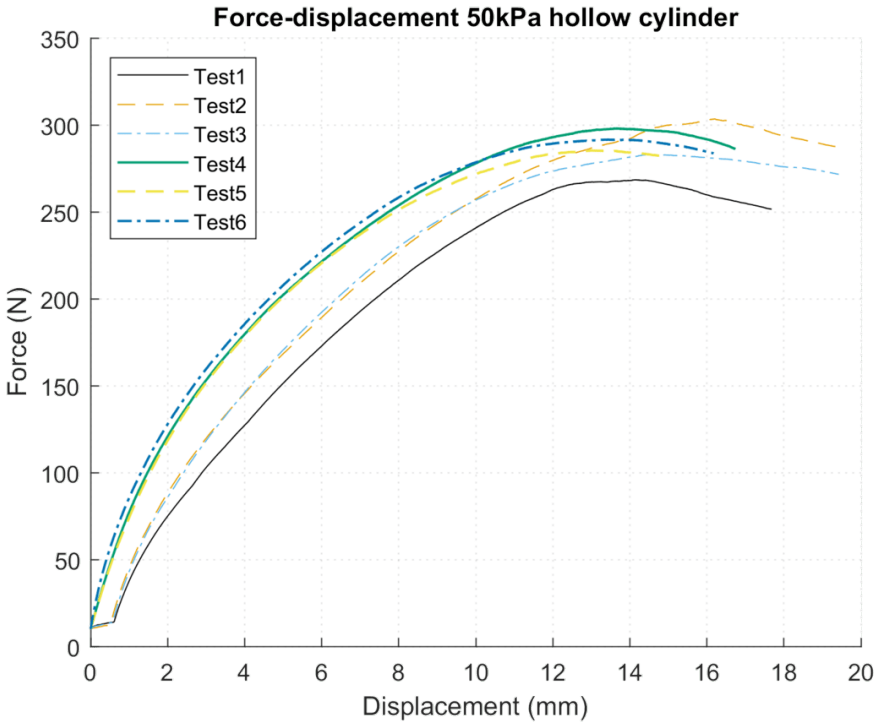

Figure B.6: Force-displacement curve for the hollow cylinder at 50 kPa

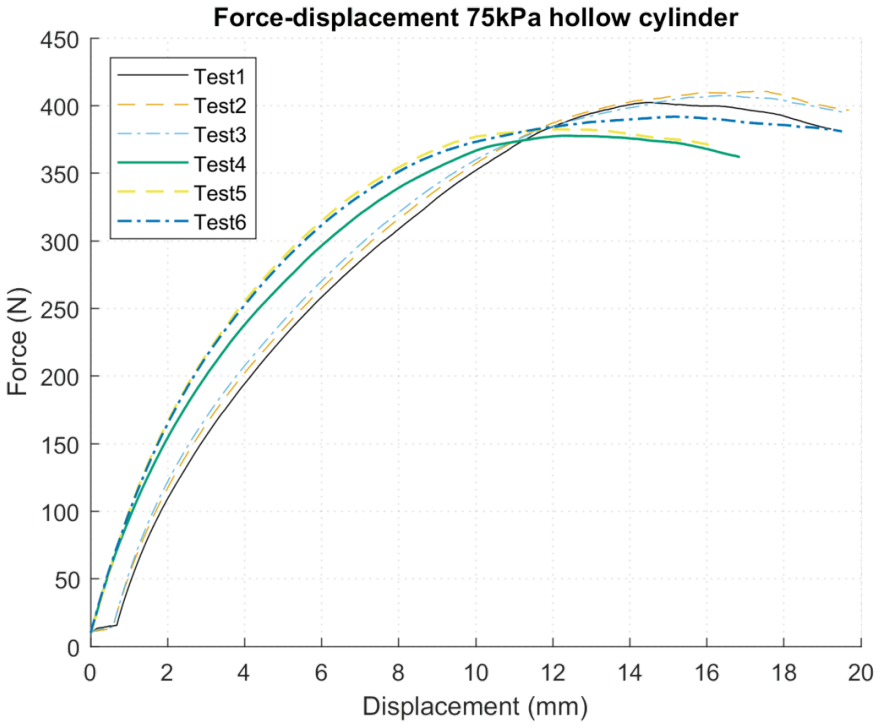

Figure B.7: Force-displacement curve for the hollow cylinder at 75 kPa

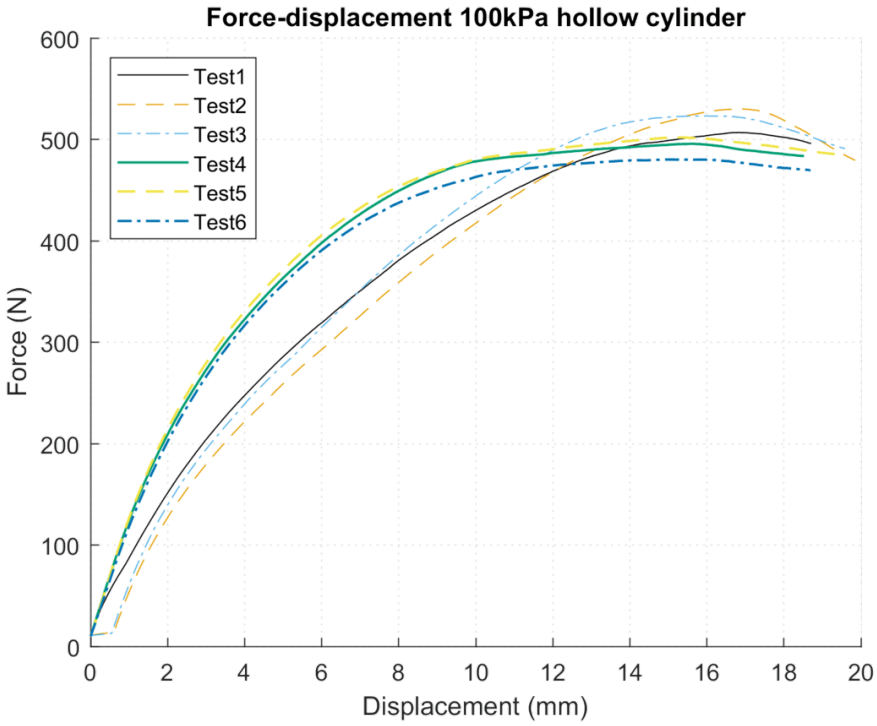

Figure B.8: Force-displacement curve for the hollow cylinder at 100 kPa

B.2 Pressure-displacement results

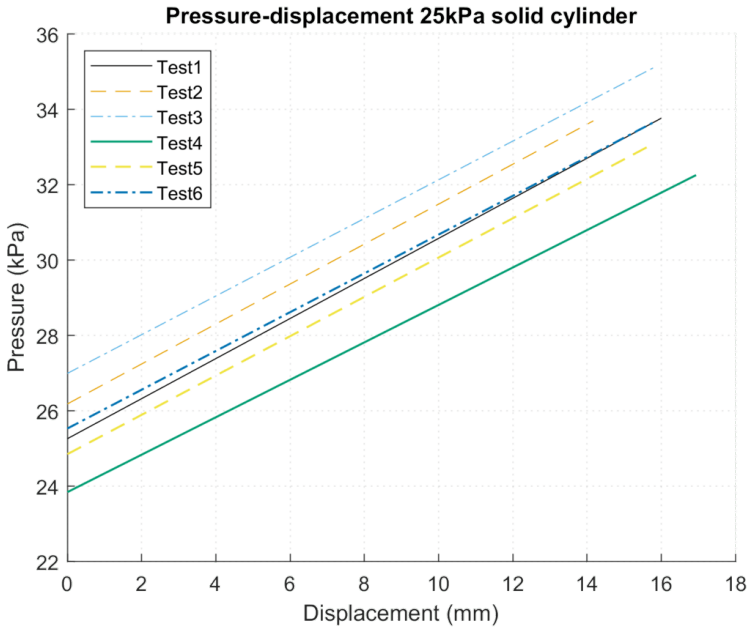

Figure B.9: Pressure-displacement curve for the solid cylinder at 25 kPa

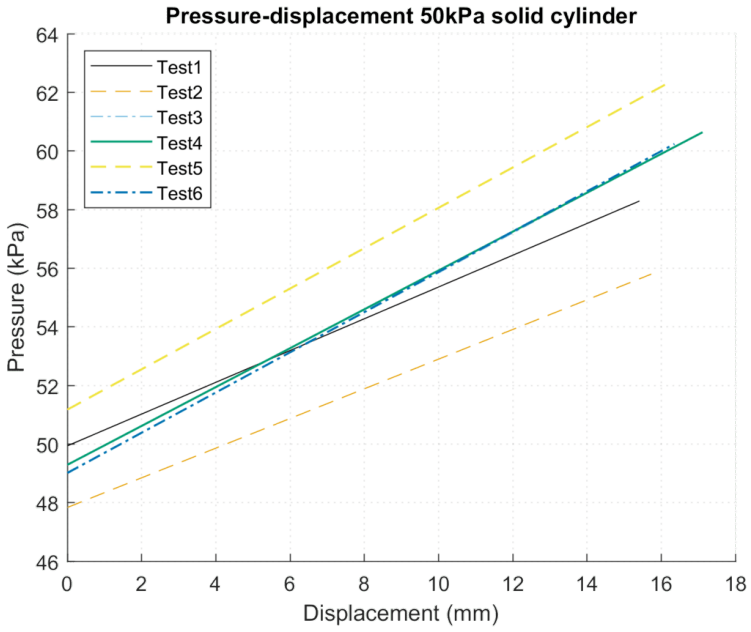

Figure B.10: Pressure-displacement curve for the solid cylinder at 50 kPa

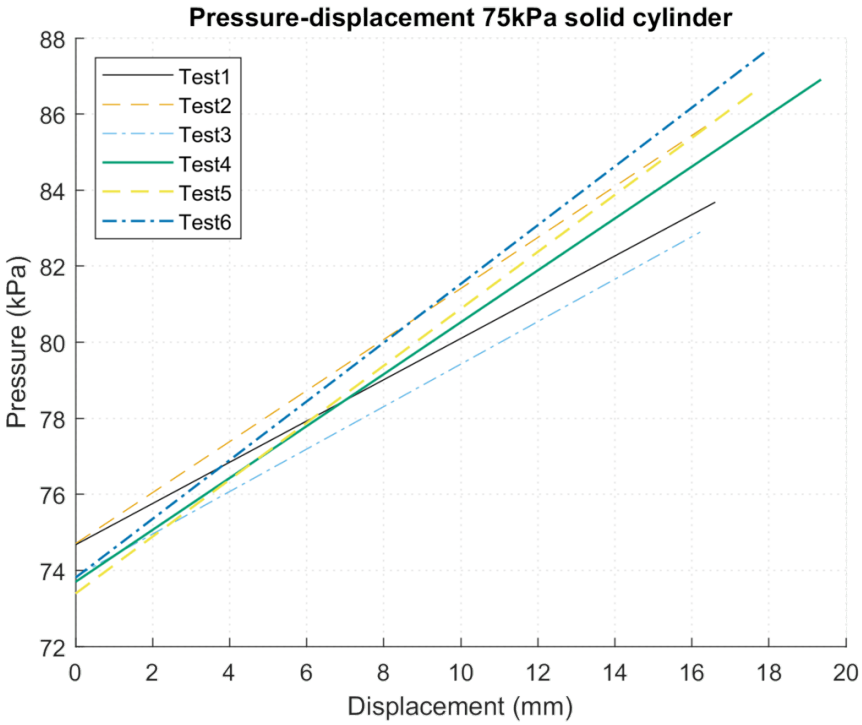

Figure B.11: Pressure-displacement curve for the solid cylinder at 75 kPa

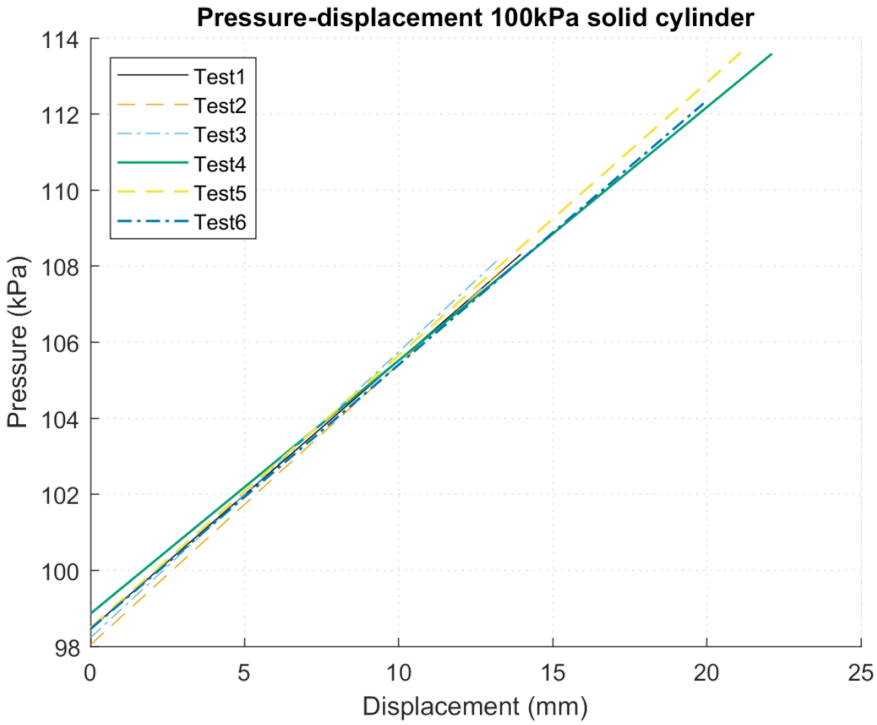

Figure B.12: Pressure-displacement curve for the solid cylinder at 100 kPa

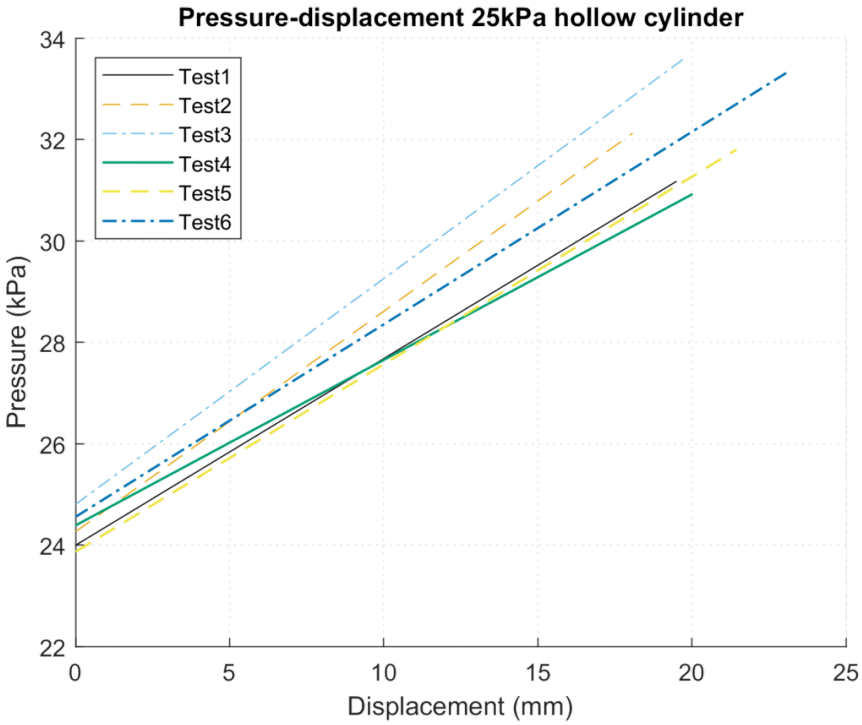

Figure B.13: Pressure-displacement curve for the hollow cylinder at 25 kPa

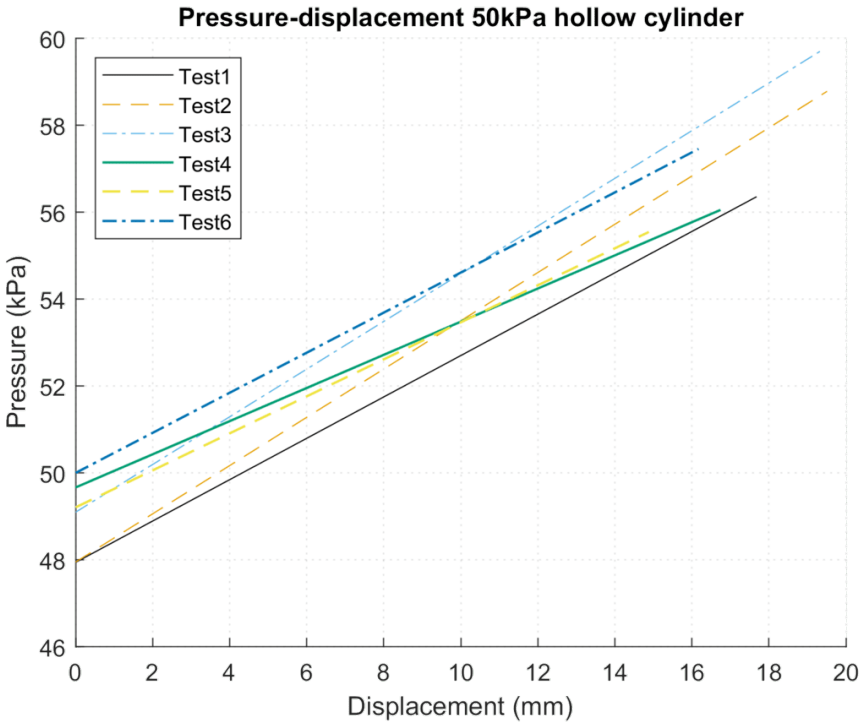

Figure B.14: Pressure-displacement curve for the hollow cylinder at 50 kPa

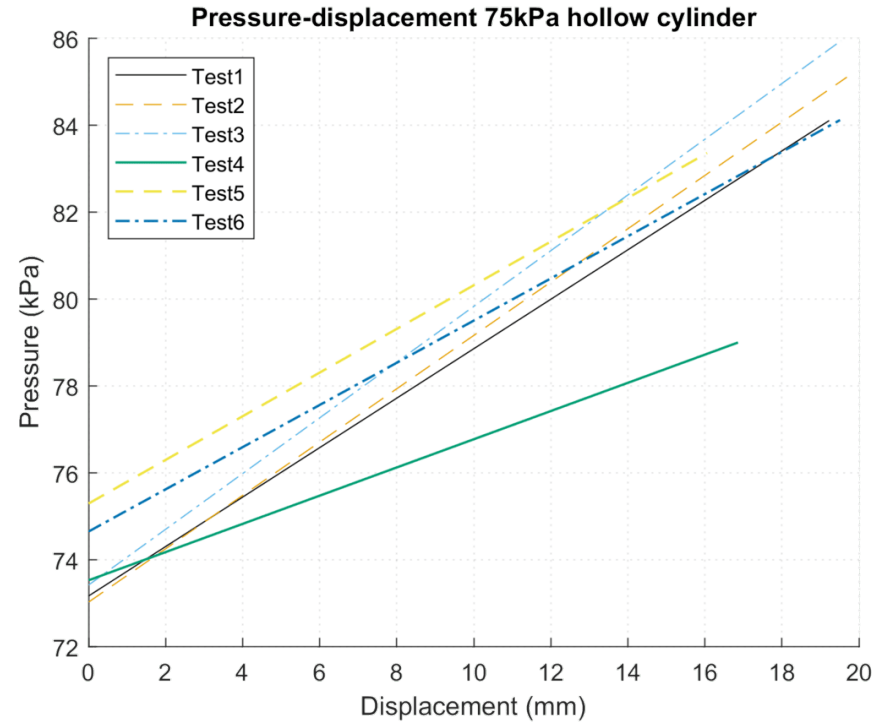

Figure B.15: Pressure-displacement curve for the hollow cylinder at 75 kPa

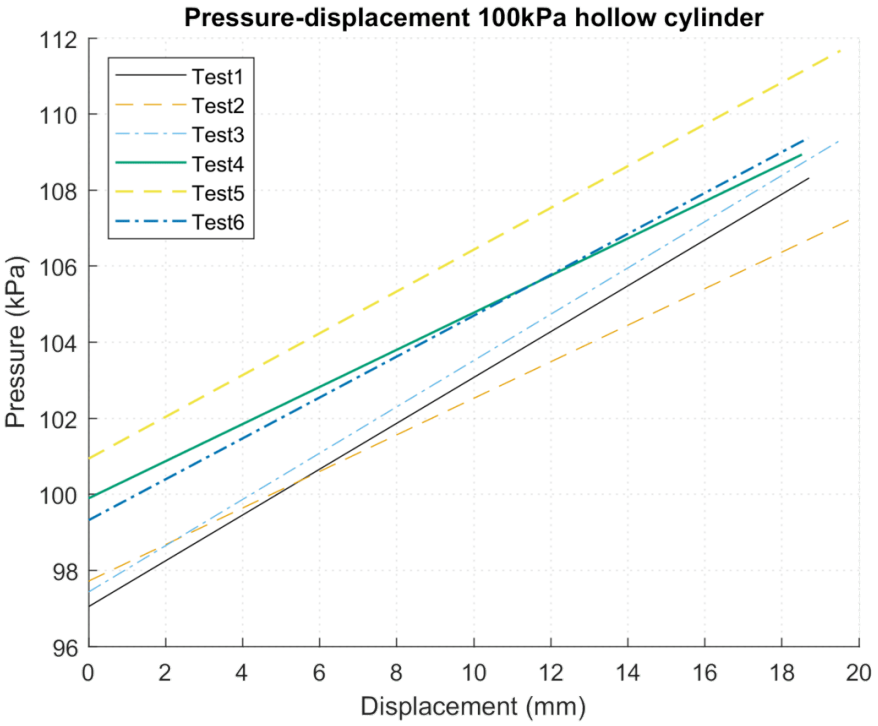

Figure B.16: Pressure-displacement curve for the hollow cylinder at 100 kPa

C Bending tests all results

C.1 Force-displacement results

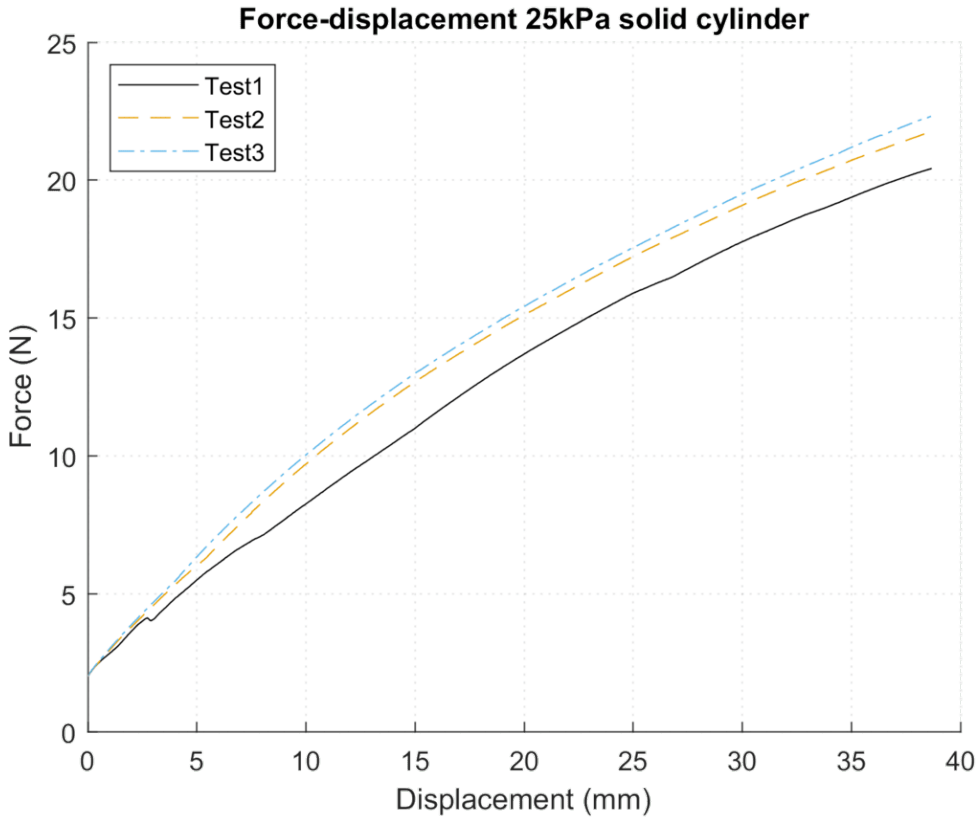

Figure C.1: Force-displacement curve for the solid cylinder at 25 kPa

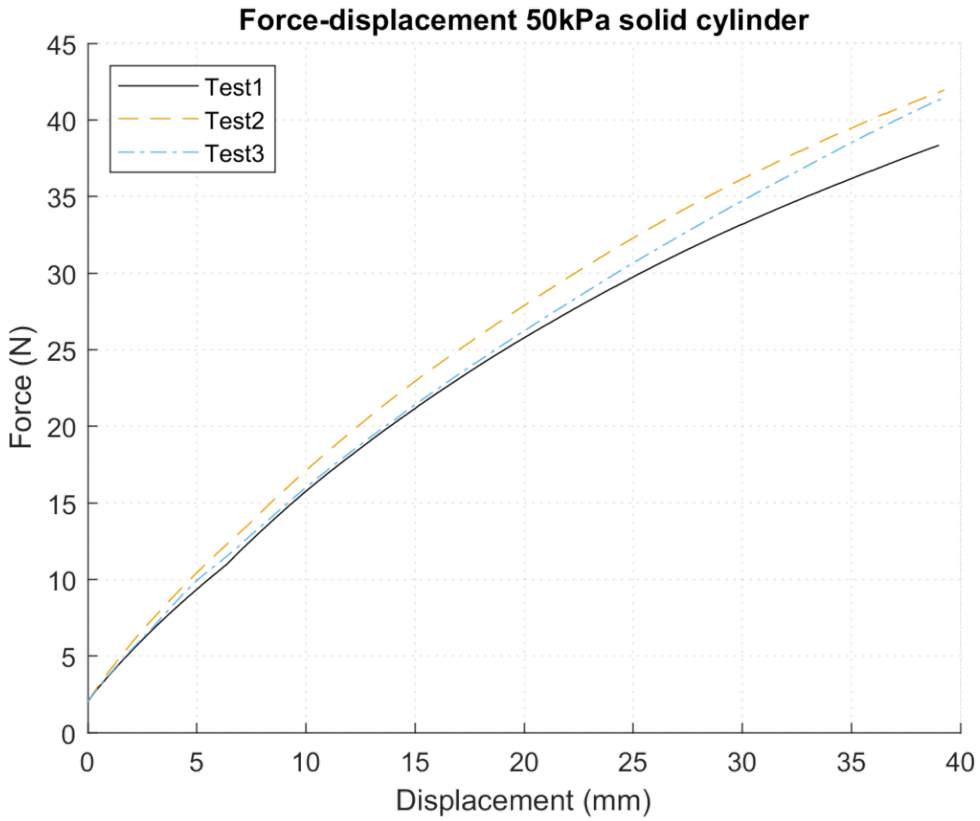

Figure C.2: Force-displacement curve for the solid cylinder at 50 kPa

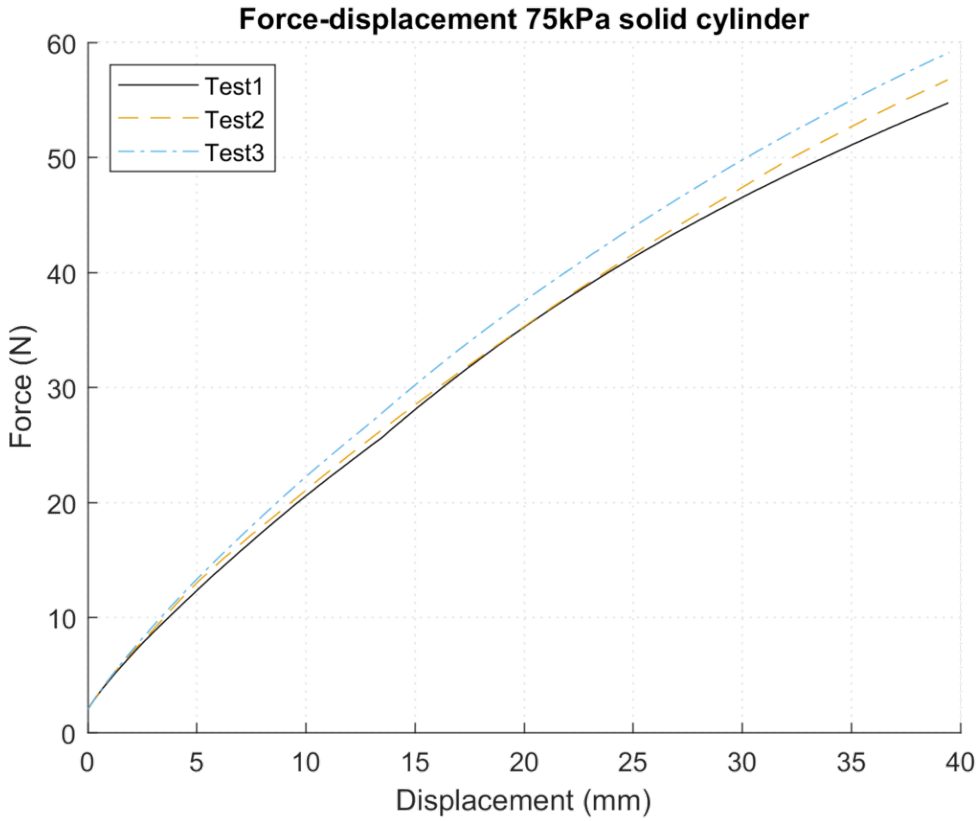

Figure C.3: Force-displacement curve for the solid cylinder at 75 kPa

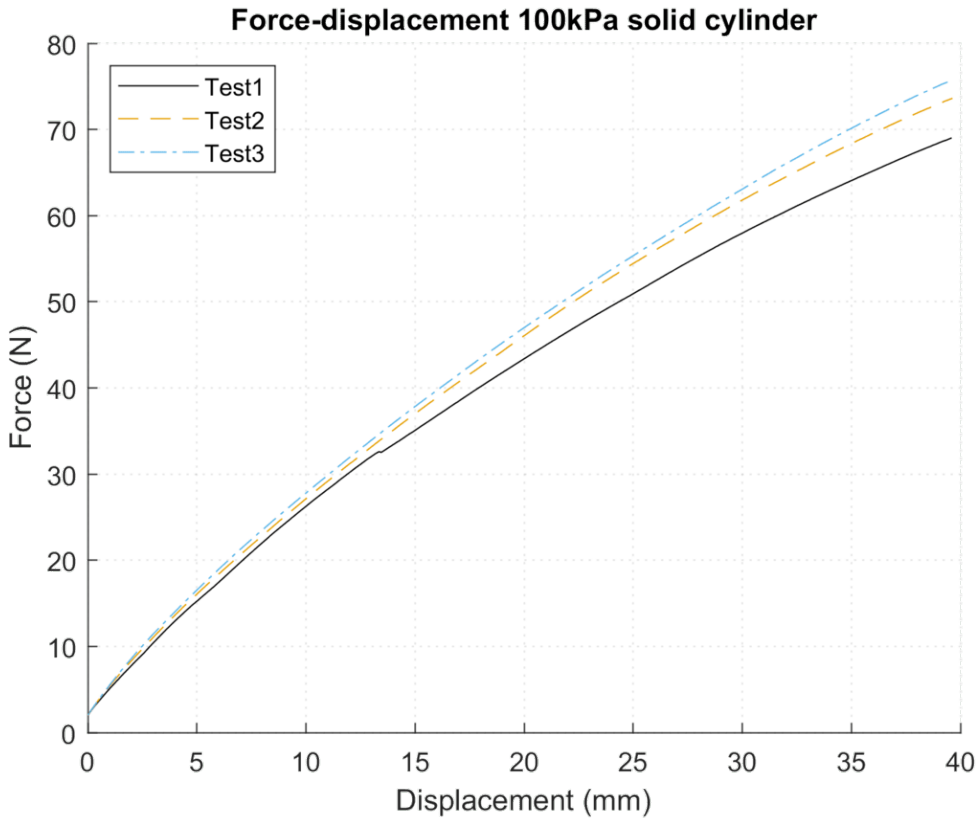

Figure C.4: Force-displacement curve for the solid cylinder at 100 kPa

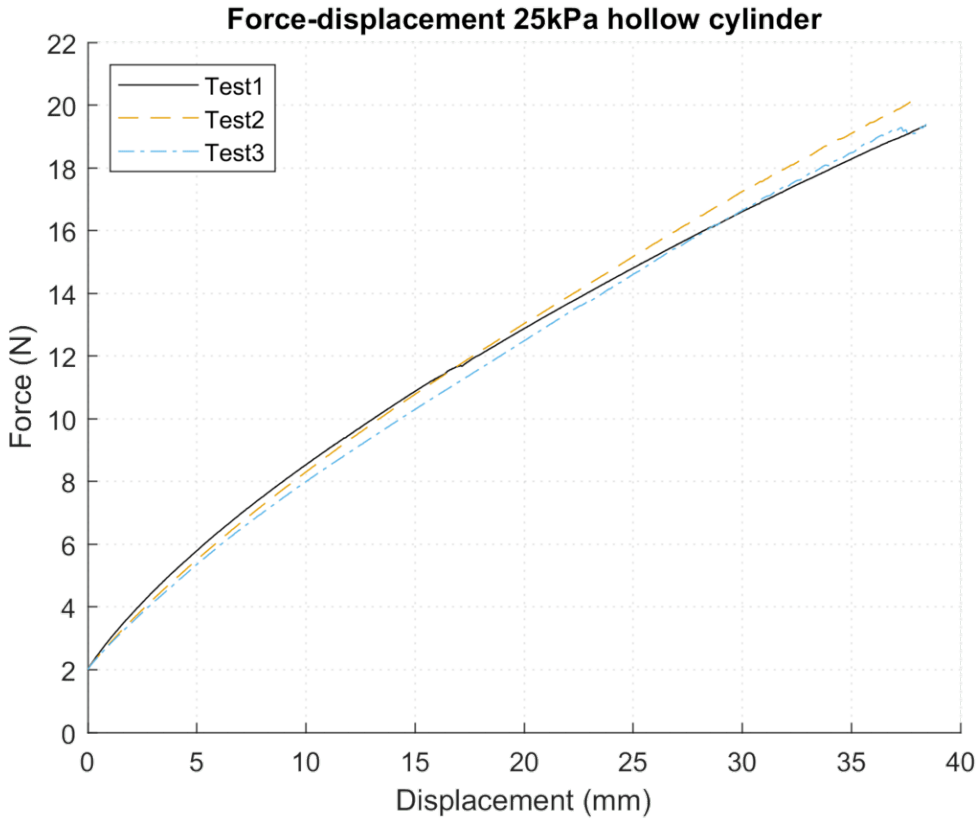

Figure C.5: Force-displacement curve for the hollow cylinder at 25 kPa

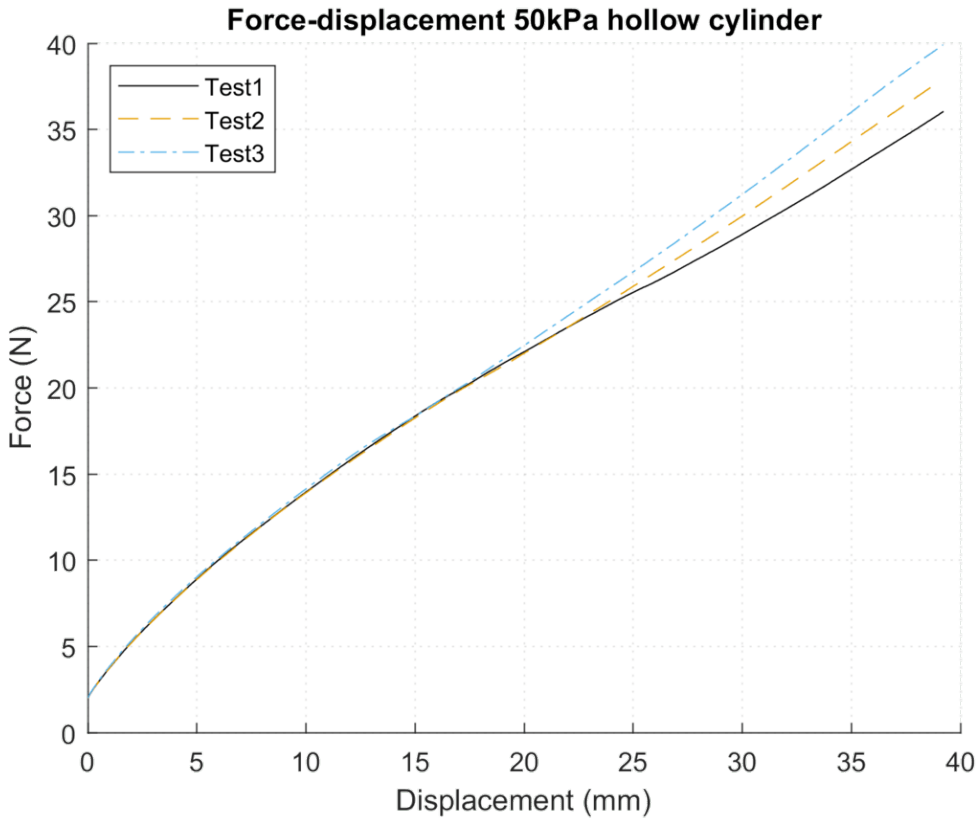

Figure C.6: Force-displacement curve for the hollow cylinder at 50 kPa

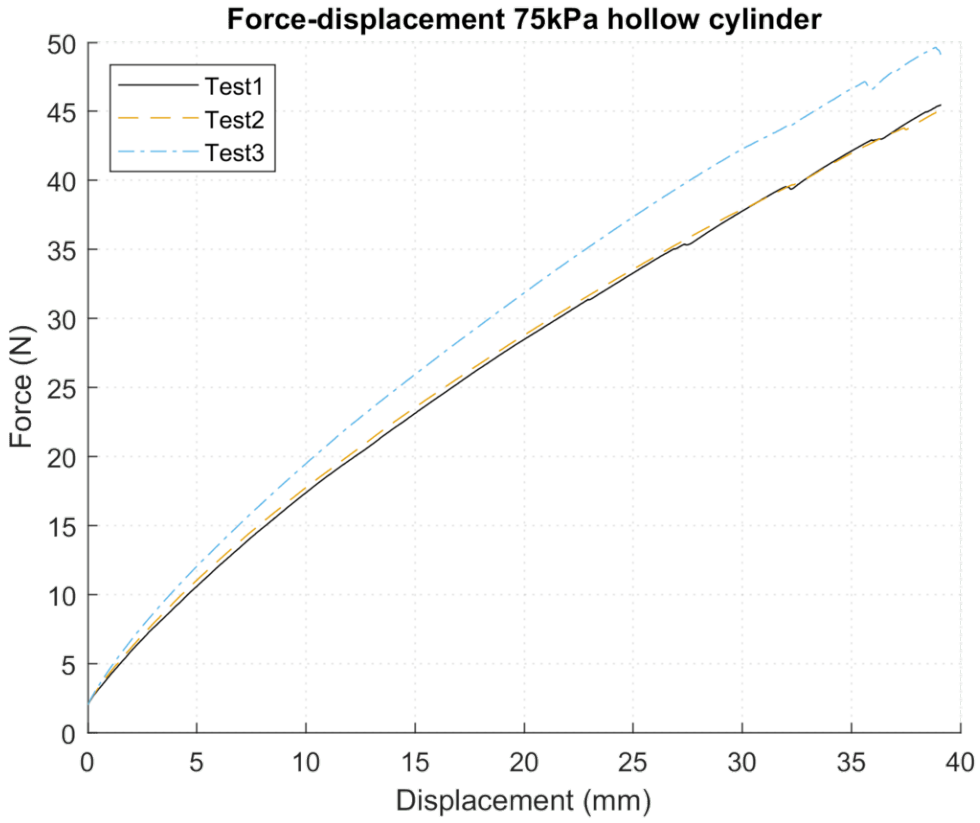

Figure C.7: Force-displacement curve for the hollow cylinder at 75 kPa

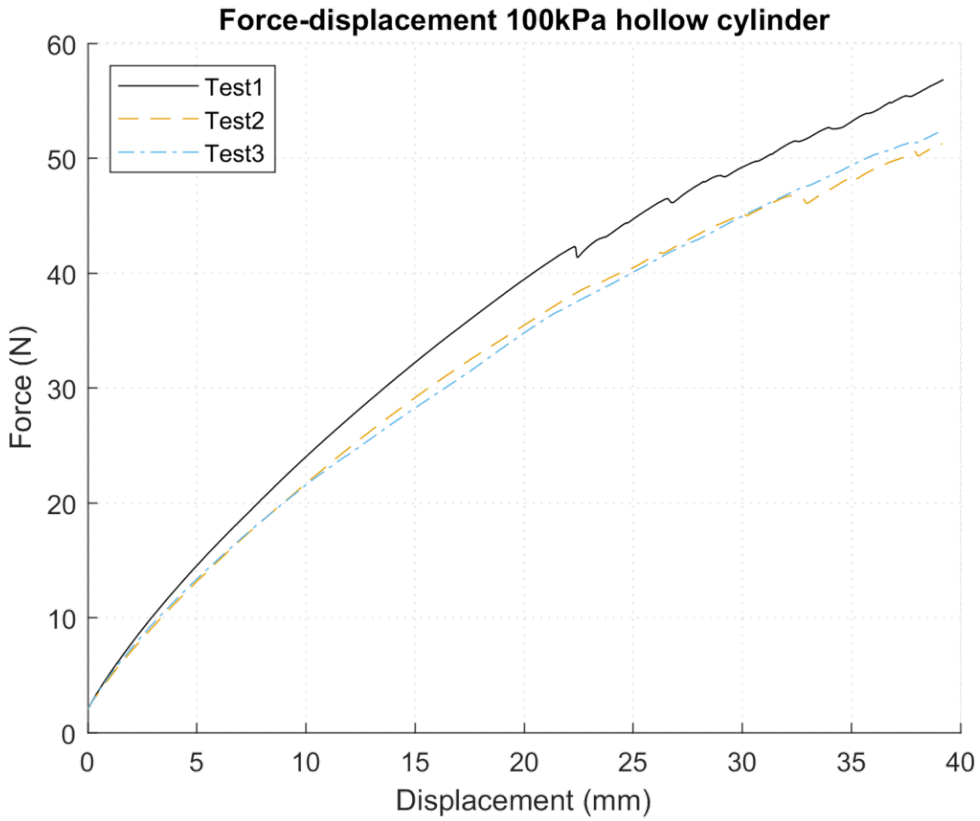

Figure C.8: Force-displacement curve for the hollow cylinder at 100 kPa

C.2 Pressure-displacement results

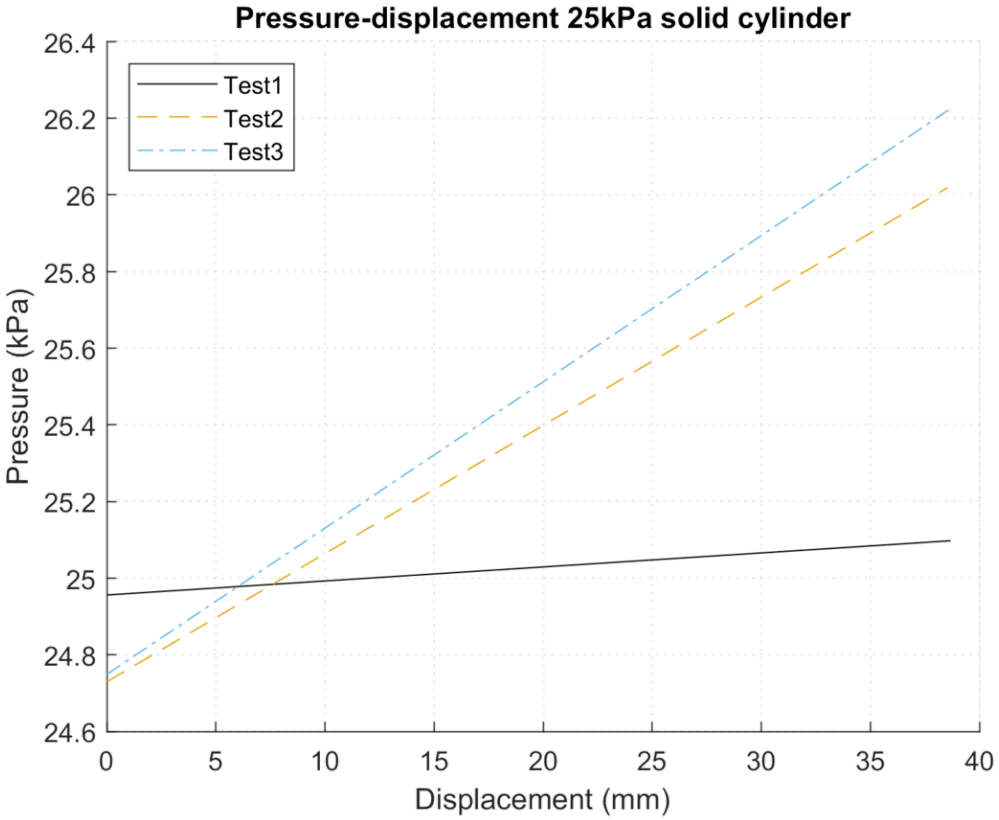

Figure C.9: Pressure-displacement curve for the solid cylinder at 25 kPa

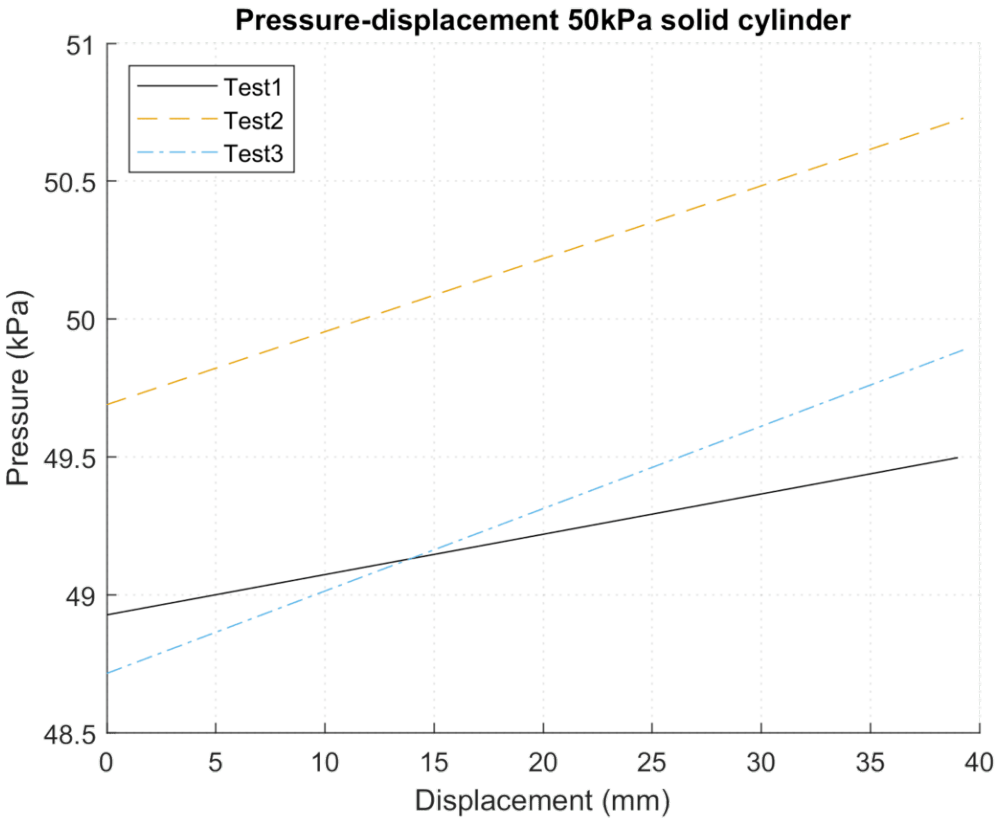

Figure C.10: Pressure-displacement curve for the solid cylinder at 50 kPa

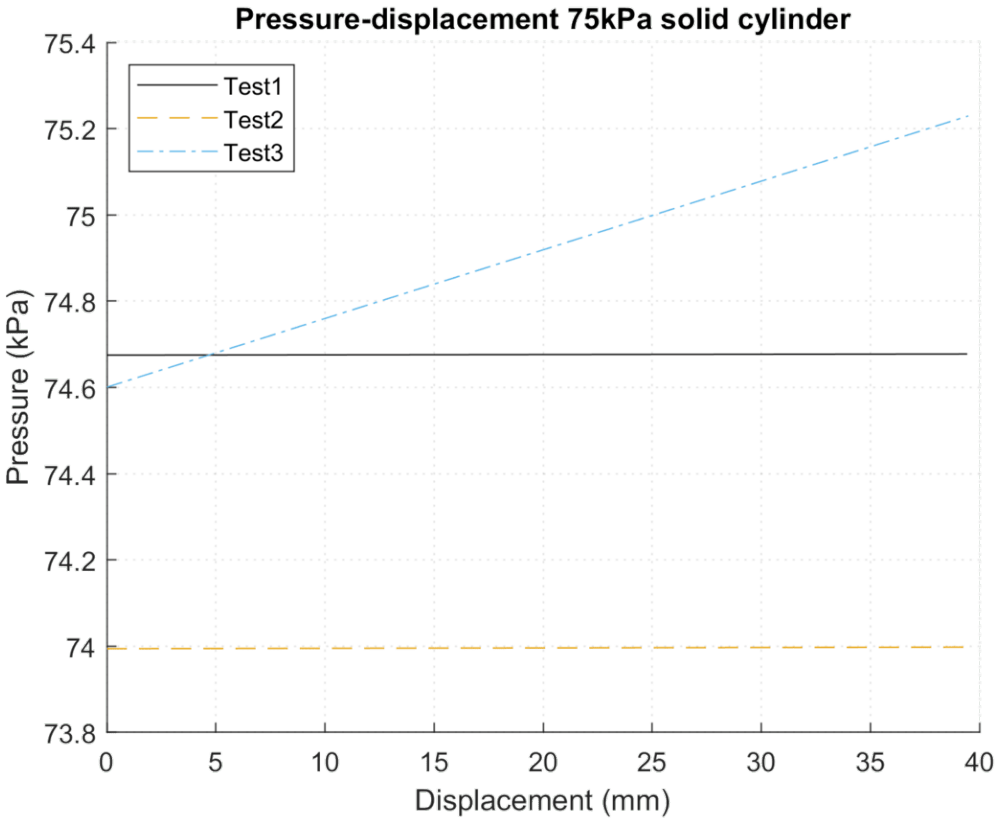

Figure C.11: Pressure-displacement curve for the solid cylinder at 75 kPa

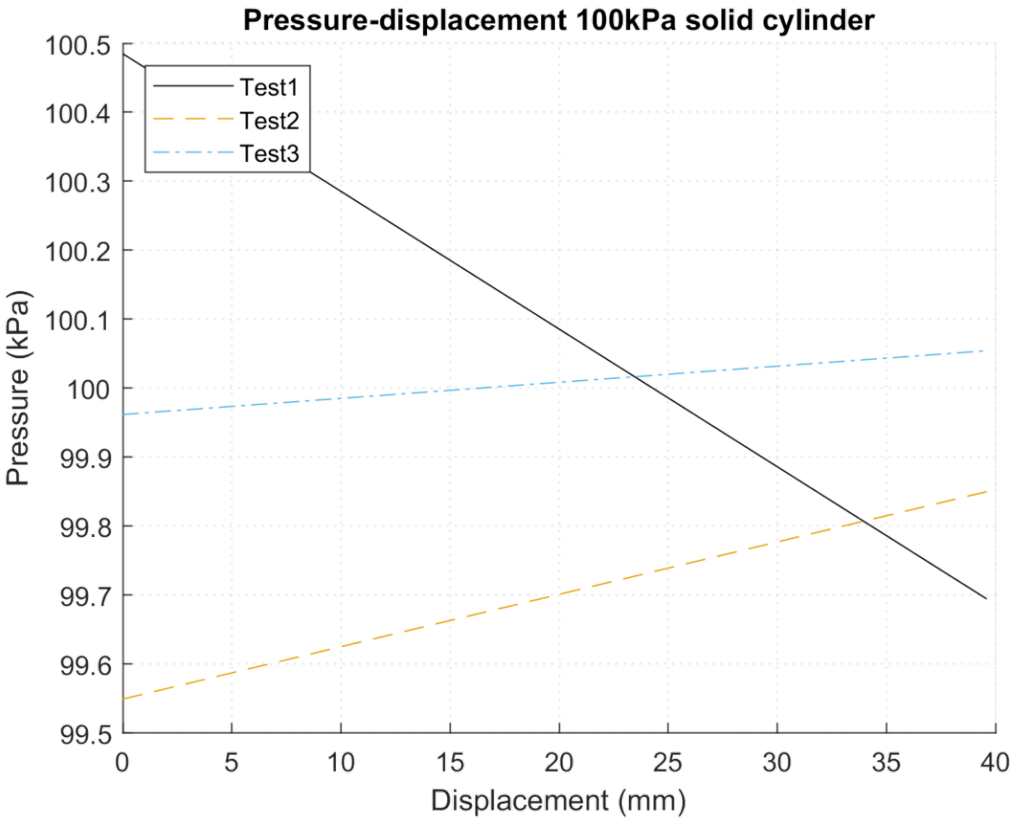

Figure C.12: Pressure-displacement curve for the solid cylinder at 100 kPa

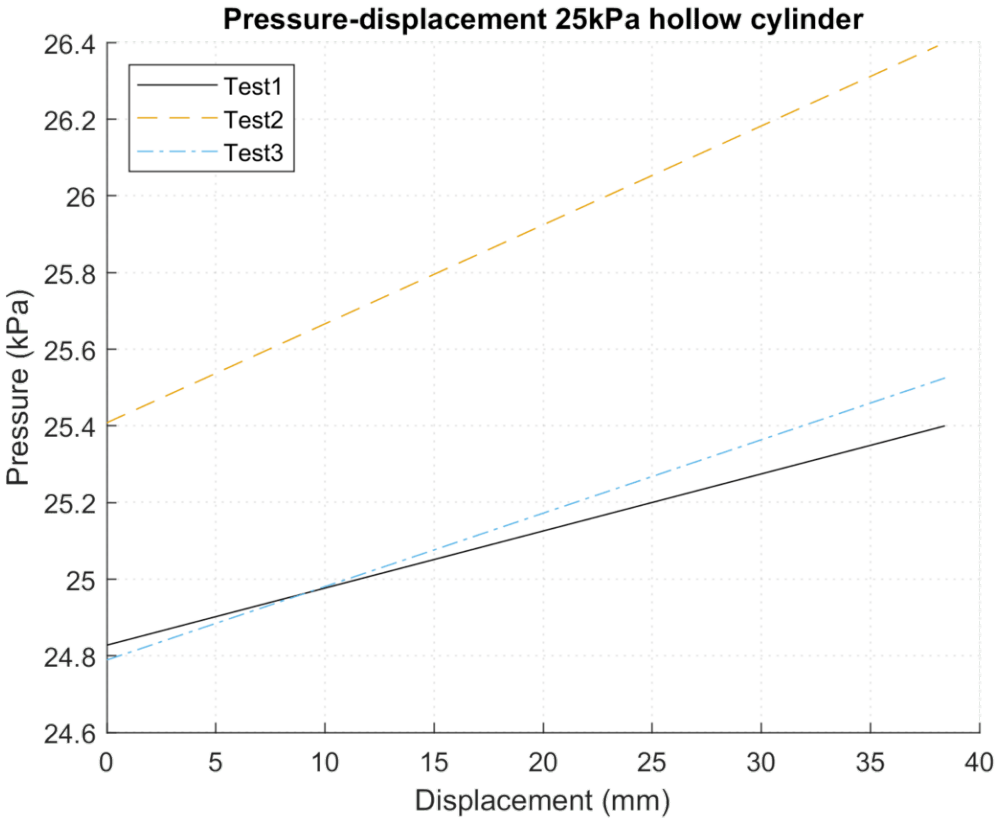

Figure C.13: Pressure-displacement curve for the hollow cylinder at 25 kPa

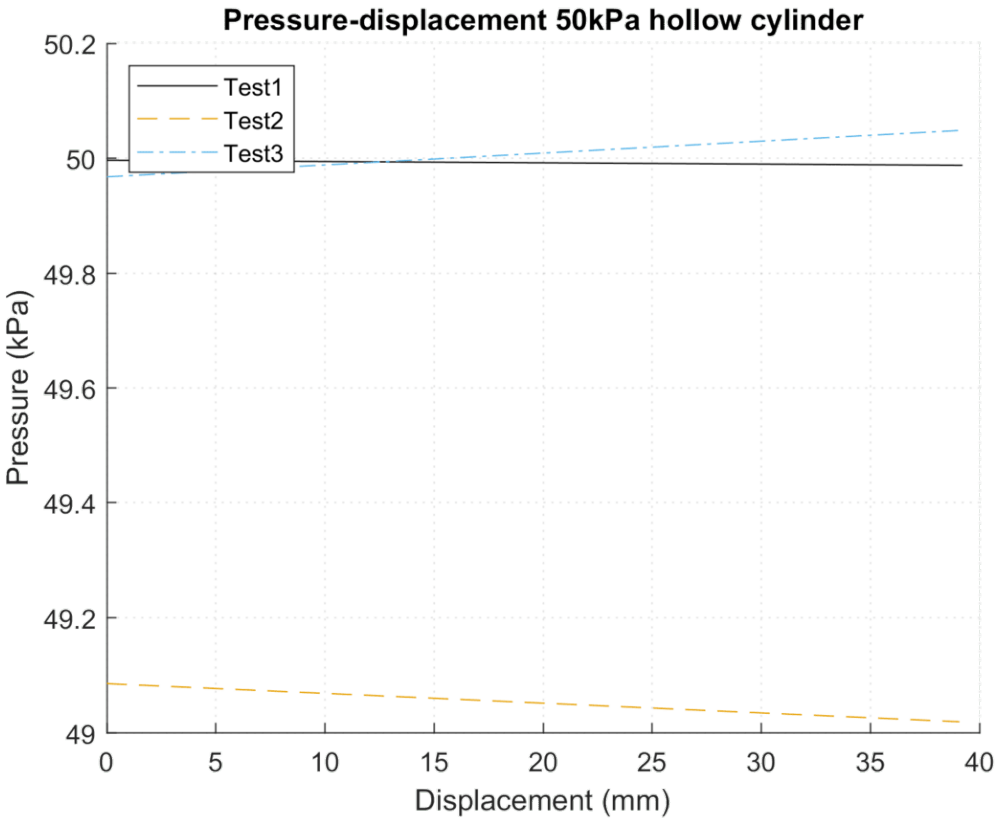

Figure C.14: Pressure-displacement curve for the hollow cylinder at 50 kPa

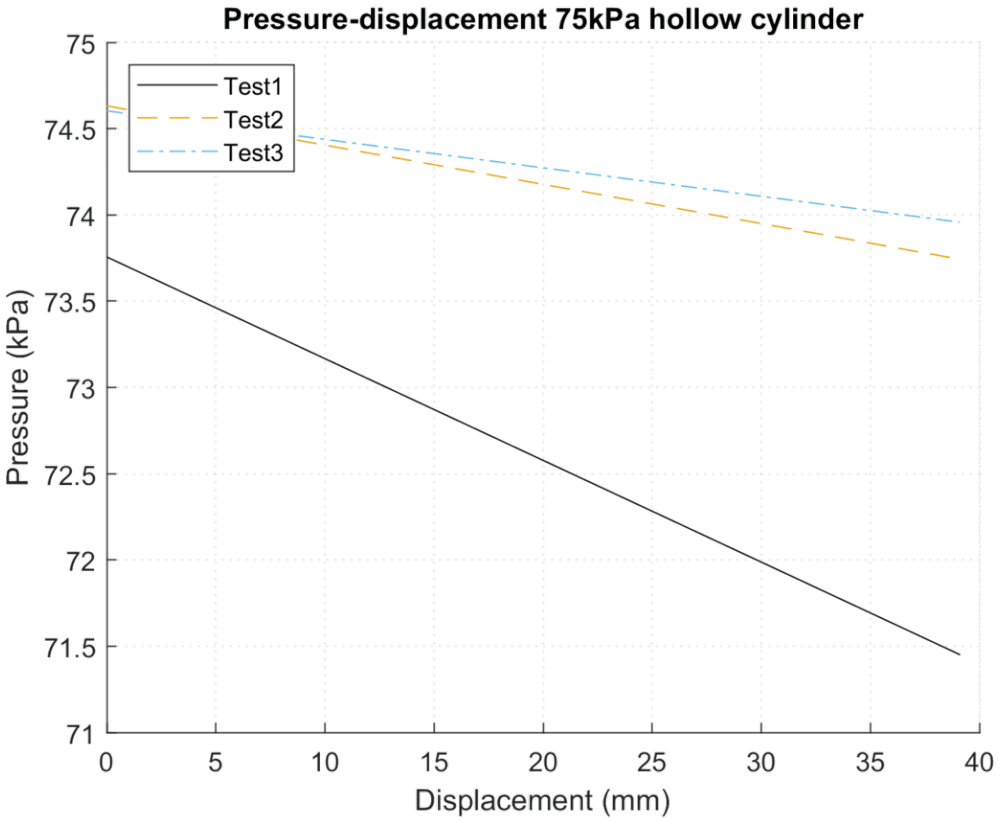

Figure C.15: Pressure-displacement curve for the hollow cylinder at 75 kPa

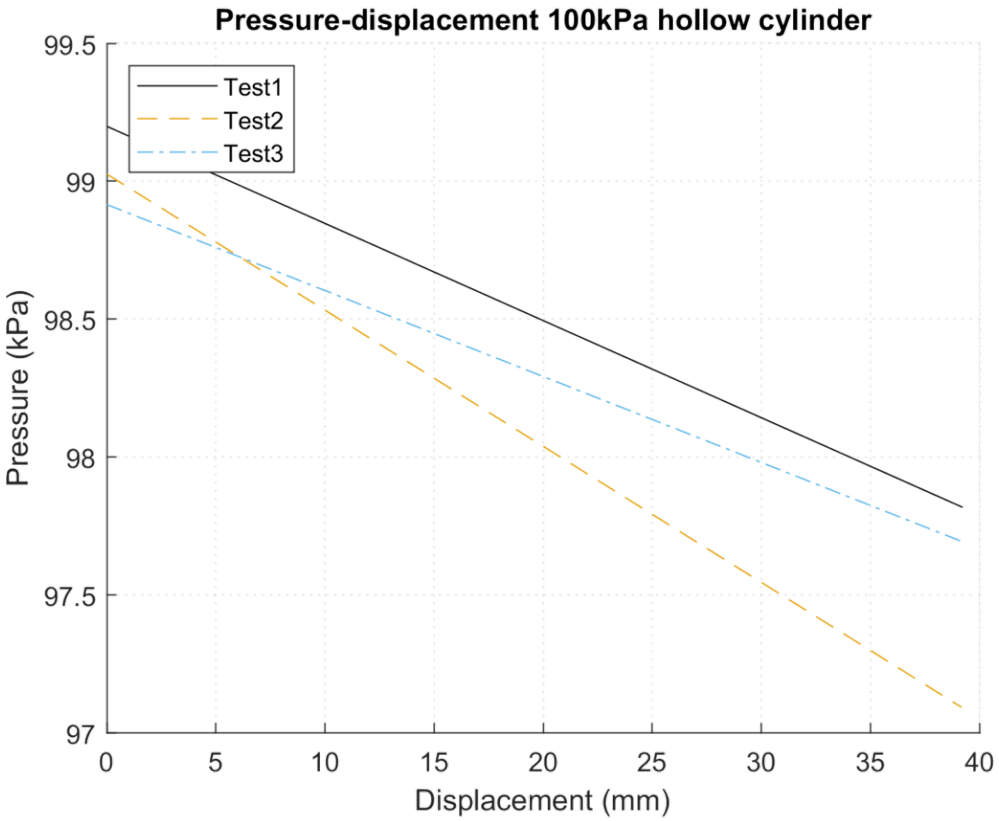

Figure C.16: Pressure-displacement curve for the hollow cylinder at 100 kPa